THE DEVELOPMENT OF NOVEL YTTERBIUM FIBER LASERS AND THEIR APPLICATIONS

By

Bai Nie

A DISSERTATION

Submitted to
Michigan State University
in partial fulfillment of the requirements
for the degree of

Physics—Doctor of Philosophy

2014

ABSTRACT

THE DEVELOPMENT OF NOVEL YTTERBIUM FIBER LASERS AND THEIR APPLICATIONS

By

Bai Nie

The aim of my Ph.D. research is to push the fundamental limits holding back the development of novel Yb fiber lasers with high pulse energy and short pulse duration. The purpose of developing these lasers is to use them for important applications such as multiphoton microscopy and laser-induced breakdown spectroscopy.

My first project was to develop a short-pulse high-energy ultrafast fiber laser for multiphoton microscopy. To achieve high multiphoton efficiency and depth resolved tissue imaging, ultrashort pulse duration and high pulse energy are required. In order to achieve this, an all-normal dispersion cavity design was adopted. Output performances of the built lasers were investigated by varying several cavity parameters, such as pump laser power, fiber length and intra-cavity spectral filter bandwidth. It was found that the length of the fiber preceding the gain fiber is critical to the laser performance. Generally, the shorter the fiber is, the broader the output spectrum is. The more interesting parameter is the intra-cavity spectral filter bandwidth. Counter intuitively, laser cavities using narrower bandwidth spectral filters generated much broader spectra. It was also found that fiber lasers with very narrow spectral filters produced laser pulses with parabolic profile, which are referred to as self-similar pulses or similaritons. This type of pulse can avoid wave-breaking and is an optimal approach to generate pulses with high pulse energy and ultrashort pulse duration. With a 3nm intra-cavity spectral filter, output pulses with about 20 nJ pulse energy were produced and compressed to about 41 fs full-width-at-half-maximum (FWHM) pulse duration. Due to the loss in the compression device, the peak power of

the compressed pulses is about 250 kW. It was the highest peak power generated from a fiber oscillator when this work was published. This laser was used for multiphoton microscopy on living tissues like Drosophila larva and fruit fly wings. Several imaging methods, such as two-photon-excited fluorescence, second harmonic generation, and third harmonic generation, were performed. Not only were single layers of thin tissue imaged, but also depth resolved imaging of thick samples was tested, and three-dimensional image reconstruction was demonstrated.

The other project was to develop a simple fiber oscillator for laser-induced breakdown spectroscopy (LIBS). Laser pulses with high energy, high ablation efficiency and low ablation threshold are desirable for this application. We built a fiber laser using up to 200 m long fiber and scaled the output pulse energy up to 450 nJ. This laser was operated in an unusual mode-locking regime and produced noise-like pulses, which have a picosecond long pulse envelope containing multiple irregular femtosecond sub-pulses. This type of pulse was mostly ignored by many earlier researchers. Intra-cavity spectral filters did not affect the laser performance as much as in the similariton lasers and were removed from the laser cavity. Characteristics of our noise-like laser, such as MHz repetition rate, broad spectrum, and picosecond-long pulse envelope containing multiple femtosecond sub-pulses, were found to meet the requirement of an ideal laser source for LIBS. A simple LIBS setup using our laser was demonstrated and atomic emission spectra with very good signal-to-noise ratio were obtained. Composition detection, qualitative concentration determination, and trace detection were also tested. These tests show that our noise-like fiber laser is an ideal laser source for a low-cost and portable LIBS system.

ACKNOWLEDGMENTS

My time here at Michigan State University has been a great learning experience scientifically and personally. Thinking about the decision to come to US for my Ph.D. study, I do not have any regrets. Professor Chong-Yu Ruan and other committee members recruiting for Physics and Astronomy Department at MSU thank you for giving me the chance of this great adventure.

My advisor, Professor Marcos Dantus, allowed me to learn a great deal of science in his lab. I am so lucky to have joined your group. The variety of research projects in your group gave me chance to learn and try many different things; and you always supported me for exploring new things. You also sent me to various conferences and encouraged me to discuss my research with people in the same field. I was very impressed by your determination and enthusiasm to approach new concepts. I feel this attitude is crucial for successful in any field. I hope that I can replicate this attitude in my following career. I really appreciate all your support during my research and job hunting.

I also would like to thank current and former members of Dantus group: Dr. Vadim Lozovoy, Dr. Marshall Bremer, Dr. Paul Wrzesinski, Dr. Sergey Arkhipov, Dr. Alexander van Rhijn, Arkaprabha Konar, Anton Ryabtsev, Ilyas Saytashev, Gennady Rasskazov, Gregory Parker, Jay Shah and Orin Yue. Thank you for sharing your toys and helping me carry out my experiments. It was a lot of fun working with you together. I would like to thank Dr. Vadim Lozovoy for the many great discussions we have had. I was always impressed by your insightful thoughts. I want to thank Ilyas Saytashev for teaching me many aspects of optical microscopy. I have bothered you the most in this group. I owe you a great debt of gratitude. Gregory Parker worked together with me on the LIBS project and helped me a lot.

Our collaborators from Cornell University, Professor Frank Wise, Andy Chong, William Renninger, Simon Lefrancois and Hui Liu, are a group of people I must thank. You were so kind to share your experience on fiber laser research and answer all my questions. Without your help, I would not have made my fiber laser work so quickly. I was always amazed by your creative thoughts.

I would like to thank Biophotonics Solutions Inc. Especially, Dr. Dmitry Pestov and Dr. Bingwei Xu, for their help with my questions and concerns regarding pulse shaper alignment and pulse compression technology. I owe a lot of gratitude to Dr. Dmitry Pestov, for purchasing equipment and components for my first fiber laser project before I joined the group. He has helped save a tremendous amount of time.

During the first week of my US adventure, I met a group of Chinese students and we remained friends in the past six years. It was a great journey with all of you together. I appreciate your help and support during my hard time. Thank you to Xianbo Yang, Xingyi Yang, Bite Zhou, Hongmei Li, Zhe Chen, Cheng Sun, Zhensheng Tao, Ding Wang, Xu Lu, Yutian Shu, Mingjie Jin.

I would like to thank my mother and father. You always supported me with patience and love. If I have ever accomplished anything, the real credit should go to you. I cannot say thank you enough.

Finally, I would like to thank my beautiful wife. I really appreciate your support and patience. Without your understanding, I could not reach the end of this adventure. I feel deeply sorry that we were mostly geographically separated in the past two years. And special thank goes to my lovely son, your smile is the strongest motivation for me to finish my Ph.D. study. Sorry, I

missed so many important moments in your life. I hope that we will get together soon and will never be separated again.

TABLE OF CONTENTS

LIST OF FIGURES

KEY TO SYMBOLS AND ABBREVIATIONS

AC	Autocorrelation
ANDi	All-Normal Dispersion
AOM	Acoustic Optical Modulator
ASE	Amplified Spontaneous Emission
BBO	Barium Borate
BW	Bandwidth
CPA	Chirped-Pulse Amplification
CW	Continuous Wave
DCF	Double-Clad Fiber
EOM	Electrical Optical Modulator
Er	Erbium
FWHM	Full Width Half Maximum
GVD	Group Velocity Dispersion
HWP	Half-Wave Plate
LIBS	Laser-Induced Breakdown Spectroscopy
LMA	Large Mode Area
KDP	Potassium Dihydrogen Phosphate
MIIPS	Multiphoton Intrapulse Interference Scan
Nd	Neodymium
NLOM	Nonlinear Loop Optical Mirror
NPE	Nonlinear Polarization Evolution
OPO	Optical Parametric Oscillator

OSA	Optical Spectrum Analyzer
PBS	Polarizing Beam Splitter
PDD	Polarization Dependent Delay
PMT	Photomultiplier Tubes
QWP	Quarter-Wave Plate
RF	Radio Frequency
SA	Saturable Absorber
SESAM	Semiconductor Saturable Absorber Mirror
SF	Spectral Filter
SMF	Single Mode Fiber
SOD	Second Order Dispersion
SWCN	Single-Wall Carbon Nanotube
Tm	Tellurium
TOD	Third Order Dispersion
SBS	Stimulated Brillouin Scattering
SHG	Second Harmonic Generation
SPM	Self-Phase Modulation
SRS	Stimulated Raman Scattering
THG	Third Harmonic Generation
TPEF	Two Photon Excited Fluorescence
UHNA	Ultra-High Numerical Aperture
WDM	Wavelength-Division Multiplexing
XPM	Cross-Phase Modulation

Yb	Ytterbium

Chapter 1 Introduction

In this thesis, two types of fiber lasers – similariton and noise-like – are studied. Both experimental and numerical simulation results are presented and compared. The laser performance is mainly described in terms of the pulse energy, the pulse duration and the peak power. A few cavity parameters, such as fiber length and intra-cavity spectral filter bandwidth, are investigated to see how they affect the laser performance. Meanwhile, our developed fiber lasers are demonstrated for applications, such as multiphoton microscopy and laser-induced breakdown spectroscopy.

The rest of this thesis is organized as follows:

Chapter 1 provides the background knowledge necessary to understand the subjects of this thesis. First, the development and science of ultrafast lasers are introduced. Following that, the properties of optical fibers and pulse propagation in passive fibers are discussed. Then, the principles of ultrafast fiber lasers and several types of ultrafast fiber laser designs are discussed. At the end of chapter 1, an ultrafast pulse shaping and characterization technology is introduced.

In Chapter 2, systematic study of sub-50 fs fiber lasers based on all-normal-dispersion cavities is presented. The dependence of laser performance on several cavity parameters is investigated. Experimentally, it is found that a narrow intra-cavity spectral filter can attract laser pulses into self-similar evolution. This result is also verified by numerical simulations.

Using our developed sub-50 fs fiber lasers, multiphoton microscopy of living tissues is demonstrated in Chapter 3. Results of second harmonic generation (SHG) imaging and third harmonic generation imaging (THG) are compared. Depth resolved imaging on Drosophila larva and fruit fly eyes is also presented.

In Chapter 4, fiber lasers delivering higher energy noise-like pulses are studied. The noise-like fiber lasers behave very differently than the similariton fiber lasers. It is found that the output pulses have the characteristic of a picosecond-long wave packet containing multiple irregular femtosecond sub-pulses. Laser-induced breakdown spectroscopy (LIBS) is tested on a few samples using a noise-like fiber laser. Based on the strong atomic emission signal, good signal-to-noise ratio and low ablation threshold, we believe that the noise-like fiber lasers can be incorporated as ideal light source for a simple LIBS system.

Our work is summarized in Chapter 5 and future directions of our work are discussed.

1.1 Introduction to ultrafast lasers

The concept of laser, Light Amplification by Stimulated Emission of Radiation, was initially proposed in the late 1950s [1] and the first functioning laser was operated by Theodore Maiman in 1960 [2]. In the past several decades, all sorts of lasers were developed, varying in emission wavelength, pulse duration or output power. Numerous scientific discoveries and innovations have been aided by lasers. Besides serving as a powerful tool for fundamental research, lasers are also widely used in industrial fields. From simple laser pointers to high power military-use lasers, from LASIK surgery to three-dimensional printing, lasers are permeating our daily life. Today's laser market is worth billions of dollars and continues to grow at an accelerating pace [3].

Most lasers follow the same principle and depend on a laser cavity. A simple laser cavity can be just two mirrors with a gain medium in between. One of the mirrors is fully reflective and the other one is partially transmitting and acts as an output coupler. The gain medium is pumped by an external optical source (not including electrically pumped lasers such as diode lasers) that provides photons with higher energy than the band-gap of the gain medium, such that electrons

in the upper energy level out-number the electrons in the lower level, a condition called population inversion. Once this state is achieved, stimulated emission happens and the cavity starts lasing. Laser light is emitted through the partially transparent mirror. The emission wavelength is determined by the band-gap of the gain medium.

There are two major modes of laser operation – continuous wave (CW) and pulsed. CW means that the output power is continuous over time. However, pulsed mode is very different; it delivers laser pulses with finite temporal duration. Each laser pulse has the same duration, which can vary from several nanoseconds to several femtoseconds. The pulsed mode can be achieved using either Q-switching or mode-locking methods. Q-switching is usually used to generate high power nanosecond laser pulses, such as from a Nd:YaG laser. To get shorter pulse duration, mode-locking is normally used.

To understand these different operation modes, we can start from a basic resonator cavity. Due to the wave-particle duality, light can be considered a wave. As light bounces back and forth between two resonator mirrors, it will form standing waves due to constructive and destructive interference. The modes of the standing waves are determined by the cavity properties. Generally, the frequency can be presented as

$$\omega = \frac{N\pi c}{nL}, \tag{1}$$

where ω is the mode frequency, N is an integer number representing the mode number, c is the speed of light, n is the refractive index of the cavity medium , and L is the cavity length.

$$\Delta\omega = \frac{\pi c}{nL}, \tag{2}$$

where $\Delta\omega$ is the fundamental mode frequency (free spectral range), corresponding to the gap between two adjacent modes.

In principle, a resonator cavity can support an infinite number of modes. However, due to the limited gain bandwidth, only certain modes can be amplified. Meanwhile, if all these modes have random relative phase, then the summation of all these modes results in a constant output in the temporal domain. If these modes are phase locked to each other, which means that their phase difference is either 0 or multiples of 2π, constructive interference between these modes happens and an intense pulse is generated. In this case, the laser is called mode-locked. Either a passive saturable absorber (or artificial saturable absorber) or active modulation (amplitude, phase, or frequency) can be used to achieve mode-locking.

Pulsed lasers are attractive for many practical applications due to their high peak power.

$$P_0 = \frac{E}{\tau} = \frac{\bar{P}\Delta t}{\tau}, \tag{3}$$

where P_0 is peak power, E is pulse energy that is the product of average power $\bar{P}$ and period time Δt, and τ is pulse duration. If the pulse duration is 1 ps, the peak power can be 10^6 times higher than the average power at 1 MHz repetition rate. With this high peak power, nonlinear effects can be realized which leads to many useful and important applications. On the other hand, regardless of the peak power, short pulse duration is also very useful. It is possible to resolve ultrafast chemical processes. All these interesting characteristics have led to the development of a new research field – ultrafast (~ ps to fs) science. There have been two Nobel Prize awarded to scientist working on ultrafast science. One was for ultrafast chemistry, which enables the observation of the transition state of molecules in chemical reactions [4]. The other one was for frequency combs which are very useful in metrology [5]. Additionally, there are many other important applications, such as multi-photon microscopy [6] and material processing [7].

Driven by the ultrafast science research and practical applications, many types of ultrafast lasers have been developed. Among them, solid-state mode-locked lasers have emerged as the most popular and useful ultrafast light sources. Currently the most popular femtosecond lasers are based on the Ti:sapphire crystal, due to its high gain and very broad gain bandwidth [8]. From a simple oscillator, sub-100 fs pulses can be easily produced. But the pulse energy is usually limited to tens of nJ due to self-focusing caused by high peak power, which can damage the gain medium. Normally, chirped-pulse amplification (CPA) [9] is used to increase the pulse energy. Chirped pulses means that the instantaneous frequency in pulses increases or decreases with time, which broadens the pulses in time domain and lowers the peak power of the pulses. The output pulses from an oscillator can be pre-chirped using pairs of gratings before being amplified in another gain medium. After the pre-chirping, the pulse duration of the input pulses usually becomes three or more orders of magnitude longer, which brings down the peak power by the same magnitude. Thus, the input pulses can be safely amplified to the μJ or mJ level. The amplified pulses are compressed back to short pulse duration afterward. Recently, pulse energy up to 1.85 MJ has been achieved by the National Ignition Facility, corresponding to a peak power of 414 TW [10].

Despite the improved performance and accelerated development of solid-state lasers, there are still problems that are hard to overcome. For example, Ti:Sapphire femtosecond lasers are sensitive to their environment because the gain crystal is exposed to the environment. Changes of temperature or humidity can easily disturb the laser operation. Also they have to be set on tables with excellent vibrational stability, otherwise mode-locking status is hard to sustain. Due to the small volume of the gain crystal, heat dissipation also becomes a problem. Usually the crystal is cooled using water, which adds complexity to the system and limits the output power or pulse

energy. Another drawback is the pump laser, usually a frequency-doubled Nd:YaG CW laser, which has low electric-to-optical efficiency or wall-plug efficiency. The size and cost are also concerns. With the development of new research and technology, robust, compact and high performance lasers are more and more desirable.

1.2 Introduction of optical fibers

In 2010, the Nobel Prize in Physics was awarded to Charles K. Kao for his contributions in the development of optical fibers. Optical fibers have many great characteristics such as low loss over long-distance propagation and flexibility. Optical fibers have made telecommunication and the majority of Internet traffic possible, and this is why they can be considered as one of the most important developments in human history.

Effectively, an optical fiber is an optical waveguide, which can propagate light along confined modes. Typical optical fibers have two layers called core and cladding, respectively (see Figure 1) [11]. The difference in the refractive index between the core and cladding causes total internal reflection of the input light and confines it. In an active single-clad fiber, the pump light and laser radiation co-propagate through the core and have the same beam quality.

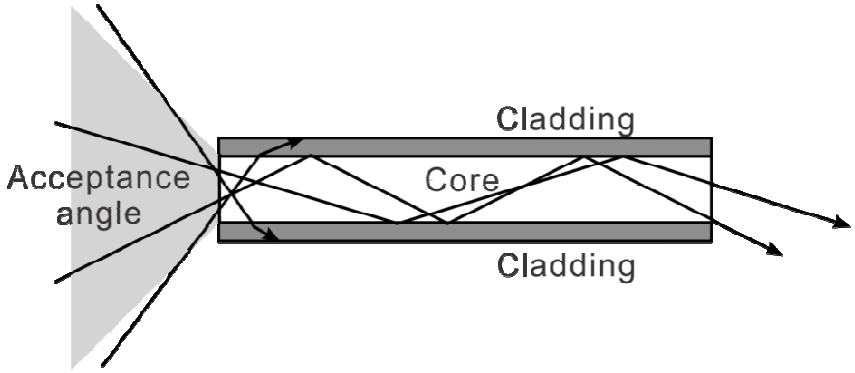

Figure 1: Schematic of a standard single-clad optical fiber [11].

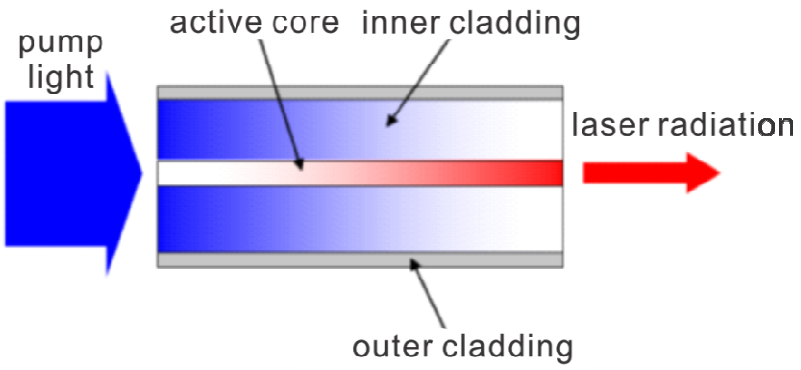

Figure 2: Schematic of a double-clad optical fiber. [12]

Besides the single-clad fibers, there are also double-clad fibers (DCF) [12], which have one core and two cladding layers (Figure 2). The inner cladding has higher refractive index than the outer cladding. Since the refractive index is frequency dependent, it can confine certain frequencies in the core while allowing some other frequencies to leak into the inner cladding, within which they are still confined by the outer cladding. As shown in Figure 2, this design allows clad pumping, where laser radiation and pump light propagate separately in the fiber core and the inner cladding, which can be as large as 100 μm, enabling the coupling of high-power pump light. These high power pump lasers are usually delivered by multimode fiber (~100 μm) and have poor beam quality. However, laser radiation still propagates in the small core and remains single mode. This new design greatly improves the pump efficiency and average power levels available form fiber lasers. Other than these, there are many more novel fibers developed, such as photonic crystal fibers [13], chirally-coupled-core fibers [14], and highly nonlinear fibers [15].

Fibers are also categorized as single-mode or multi-mode fibers and as passive or active fibers. Usually multi-mode fibers have larger diameter than single mode fibers and can support light with many spatial modes other than HE_{11} mode. The most common fiber is made of fused silica. Normally, germanium dioxide or aluminum oxide is used as dopant to raise the refractive

index. Fluorine or boron trioxide doping is used for decreasing the refractive index. For active fiber or gain fiber, the core is usually doped with rare earth ions.

There are several important parameters of optical fibers. Among them, the two most important for ultrashort laser pulses are chromatic dispersion and third order susceptibility $\chi^{(3)}$, which dominate the linear and nonlinear effects on the laser pulses, respectively. Chromatic dispersion means that different frequencies travel with different group velocities due to the frequency-dependent refractive index. Thus, a transform-limited pulse can be chirped to a longer pulse after going through a fiber. The chromatic dispersion can be either positive, negative or zero; the material used for fiber fabrication and the waveguide structure determine it. Waveguide dispersion arises from the frequency-dependent effective mode index of a waveguide [16], defined by

$$\begin{aligned}
&\frac{1}{v_g} = \frac{d\beta}{d\omega} = \frac{n_2}{c} + \frac{n_1 - n_2}{c}\left(\frac{d}{dV}(bV)\right), \\
&\beta = \frac{\omega}{c}\left(n_2 + (n_1 - n_2)b(V)\right), \\
&V = k_0 a\left(n_1^2 - n_2^2\right)^{1/2}, \\
&b \approx \frac{\beta - k_0 n_2}{k_0 (n_1 - n_2)}, \\
&k_0 = 2\pi/\lambda,
\end{aligned} \tag{4}$$

where v_g is the group delay due to waveguide, n_1 and n_2 are the refractive index of core and clad, c is speed of light, a is core radius, and λ is the wavelength of light.

Normally waveguide dispersion is small compared to the material dispersion and can be ignored. Figure 3 shows the variation of material, waveguide, and total dispersion for a standard silica fiber [17]. But for a fiber with zero material dispersion, waveguide dispersion has to be considered.

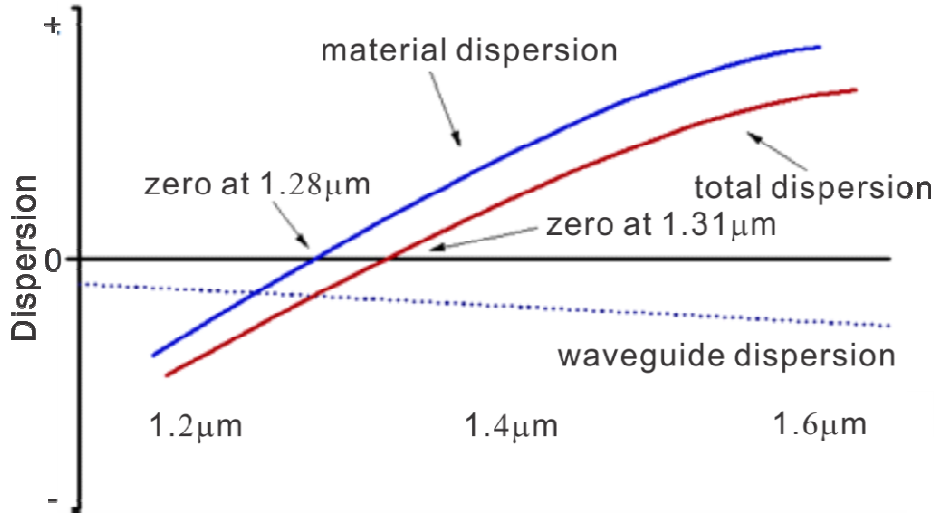

Figure 3: Variation of material (blue), waveguide (dot) and total (red) dispersion for a silica fiber. [17]

Chromatic dispersion is a linear optical effect and can be easily dealt with. On the other hand, due to the small core size of a fiber, the high peak power of an ultrafast laser pulse can result in very high peak intensity and cause significant nonlinear effects. The major effects include self-phase modulation (SPM), cross-phase modulation (XPM), stimulated Raman scattering (SRS) and stimulated Brillouin scattering (SBS). All these effects originate from the third order susceptibility $\chi^{(3)}$. SPM and XPM are due to the nonlinear refractive index change. SRS and SBS are related to excitation of acoustic phonons and optical photons, respectively, of silica. All these linear and nonlinear effects in an optical fiber can be described by [18]

$$\begin{aligned} &\frac{\partial A}{\partial z}+\frac{\alpha}{2}A+\beta_1\frac{\partial A}{\partial t}+\frac{i}{2}\beta_2\frac{\partial^2 A}{\partial t^2}-\frac{1}{6}\beta_3\frac{\partial^3 A}{\partial t^3} \\ &=i\gamma\left(1+\frac{i}{\omega_0}\frac{\partial}{t}\right)\left(\left(A(z,t)\right)\int_0^{\infty}R(t')\left|A(z,t-t')\right|^2 dt'\right), \end{aligned} \tag{5}$$

where A is the pulse amplitude, which is a function of propagation distance z and time t, α is the fiber loss, β_1 is the group delay, β_2 is the group-velocity dispersion (GVD), β_3 is the third order

dispersion, ω_0 is the carrier frequency of the pulse, and *R(t)* is the nonlinear response function, which is related to higher order nonlinear effects such as SRS and self-steepening. γ is the nonlinear coefficient, defined by

$$\gamma = \frac{n_2 \omega_0}{c A_{eff}}, \tag{6}$$

where n_2 is the nonlinear refractive index and is related to $\chi^{(3)}$, and A_{eff} is the effective fiber core area.

In most cases, the higher order nonlinear effects such as SRS and SBS can be ignored and the Equation (5) can be simplified as

$$\frac{\partial A}{\partial z} + \frac{i}{2}\beta_2 \frac{\partial^2 A}{\partial t^2} - \frac{1}{6}\beta_3 \frac{\partial^3 A}{\partial t^3} = i\gamma |A|^2 A. \tag{7}$$

Only chromatic dispersion (left terms in Equation (7)) and nonlinear refraction (right term in Equation (7)) terms need to be considered. Without the third order dispersion term, Equation (7) becomes

$$\frac{\partial A}{\partial z} + \frac{i}{2}\beta_2 \frac{\partial^2 A}{\partial t^2} - i\gamma |A|^2 A = 0. \tag{8}$$

Equation (8) is sometimes referred to as a nonlinear Schrödinger equation (NLSE) [18, 19], since it has the same form as a basic NLSE defined by [20, 21]

$$i\frac{\partial \psi}{\partial t} + \frac{1}{2}\frac{\partial^2 \psi}{\partial x^2} + \kappa |\psi|^2 \psi = 0, \tag{9}$$

where ψ is a complex function, the variables *t* and *x* are frequently but not limited to time and space coordinates, and κ is a nonlinear coefficient. Unlike the linear Schrödinger equation, the NLSE does not describe the time evolution of a quantum state. Instead, it is generally used to

describe the evolution of slowly varying wave packets in nonlinear media with dispersion [21]. Nonlinear effects, such as self-focusing [22] and pulse propagation in optical fibers [23], have been successfully described using this equation.

With only chromatic dispersion terms ($\gamma = 0$), Equation (7) is linear and can be solved analytically. Pure dispersion affects the pulse in the temporal domain while keeping its spectrum unchanged. Some numerical simulation results are illustrated in Figure 4 (the simulation code is presented in Appendix). Significant changes of temporal profile are observed. However, the spectra remain the same.

The parameter used to characterize the effect of dispersion is the dispersion-length, which is defined as

$$L_D = \frac{\tau^2}{|\beta_2|}, L_D' = \frac{\tau^3}{|\beta_3|}, \tag{10}$$

where L_D and L_D' represent the dispersion length corresponding to second order and third order dispersion, respectively. τ is the full-width half-maximum (FWHM) pulse duration.

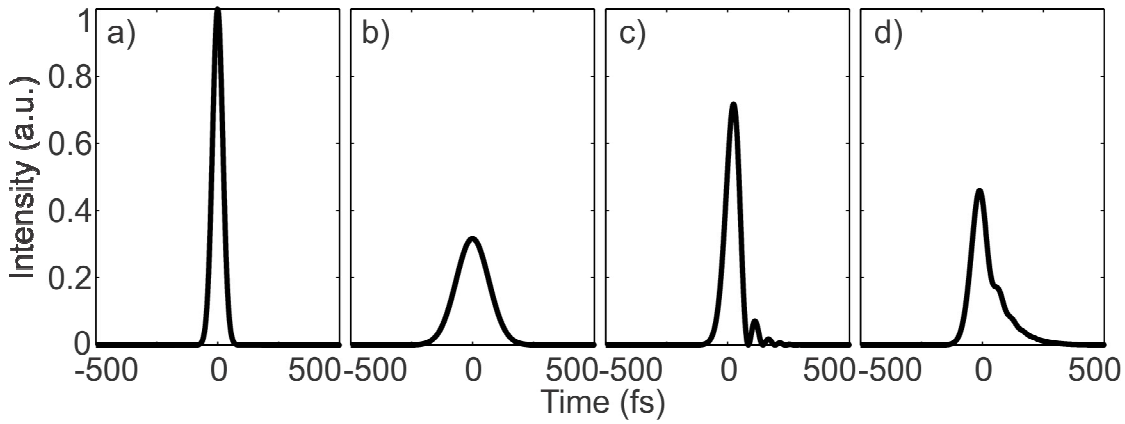

Figure 4: Simulation results. Pulse profiles of a) input pulse; b) pulse after propagating through 3*L_D-long fiber with β_3=0; c) pulse after propagating through 3*L_D'-long fiber with β_2=0; d) combined effects of (b) and (c).

The introduction of the nonlinear refraction term makes the problem more complicated. With a non-zero γ, Equation (7) can no longer be solved analytically. The way to figure out the effects of pulse propagation is to use numerical simulation with the split-step method [24, 25]. By using small steps for the pulse propagation, the linear (dispersion) and nonlinear parts in NLSE can be treated separately. Figure 5 shows simulation results of the effects caused by nonlinear refraction without dispersion introduced (the simulation code is presented in Appendix). A pulse propagates through a length L_{NL} of fiber, and a spectral broadening is observed while the pulse profile is preserved. L_{NL} is the nonlinear length, defined as

$$L_{NL} = \frac{1}{\gamma P_0}. \tag{11}$$

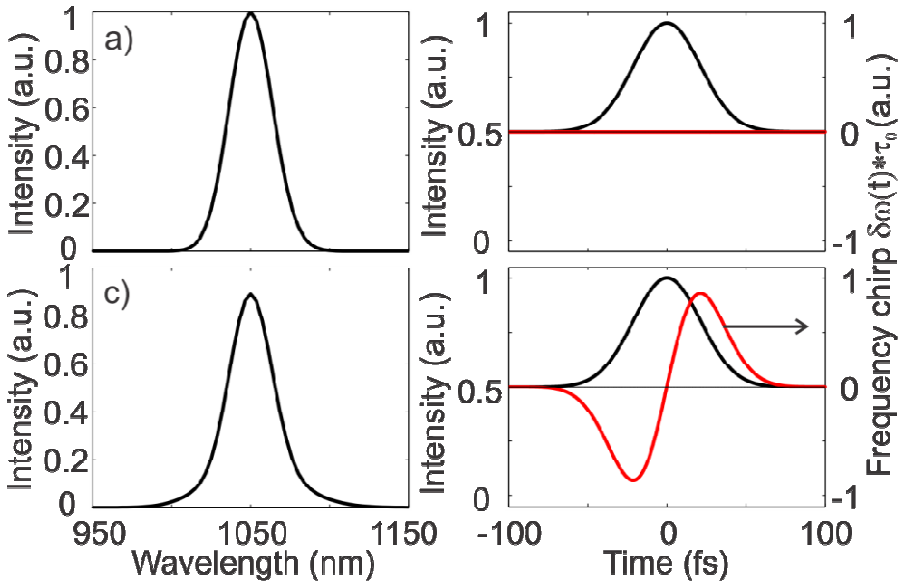

Figure 5: Simulation results. Top: (a) input pulse spectrum and (b) temporal profile; Bottom: (c) spectrum and (d) temporal profile of pulse after propagating a distance L_{NL} in fiber. Red line: frequency chirp induced by SPM.

This phenomenon is called self-phase modulation (SPM). The spectral broadening is due to the time dependence of the self-induced nonlinear phase shift (ϕ_{NL}) experienced by an optical

pulse during its propagation through the fiber. The SPM induced chirp, or the difference between instantaneous optical frequency and central frequency, is plotted in Figure 5(d). Though the pulse has the same profile, it is not transform-limited any more.

The nonlinear phase shift is a very important parameter for pulse evolution in the fiber, and is defined by

$$\begin{aligned} \phi_{NL} &= \frac{2\pi}{\lambda} n_2 L \left|E\right|^2, \\ \phi_{NL}^{\max} &= L/L_{NL} = \gamma P_0 L, \end{aligned} \tag{12}$$

where L is the fiber length, λ is the carrier wavelength of optical pulse, E is the electric field in the temporal domain, and P_0 is the peak power of pulse. The pulse experiences a maximum nonlinear phase shift ($\phi_{NL}^{\max}$) of 1 radian after propagating through L_{NL} long fiber. Simulation results of the spectral broadening corresponding to different maximum nonlinear phase shifts are shown in Figure 6. The larger $\phi_{NL}^{\max}$ is, the broader the output spectrum is.

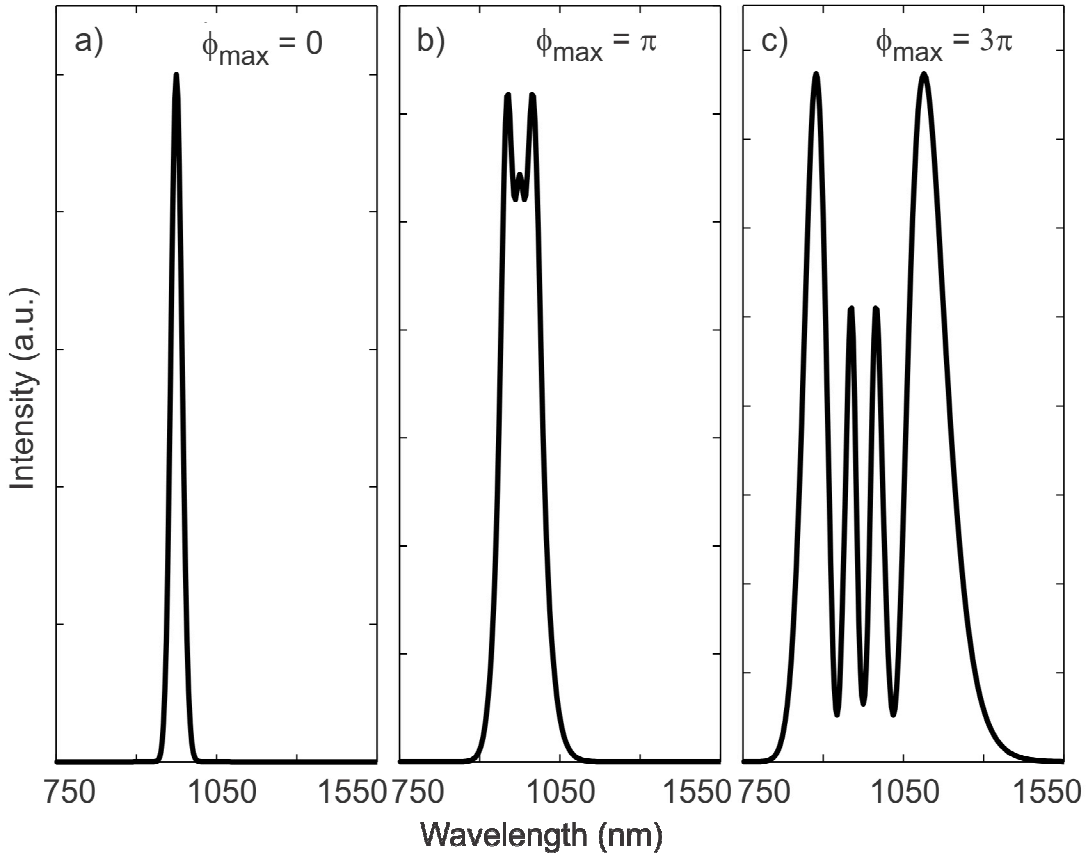

Figure 6: Simulated SPM induced spectral broadening of the pulse experiencing a maximum nonlinear phase shift of a) 0; b) π; c) 3.5π. ϕ_{max} is the maximum nonlinear phase shift.

Previously, we only considered the effects of chromatic dispersion and nonlinear refraction independently. In reality, they always exist together and affect each other, and this causes more complicated and interesting effects. As shown in Figure 7, the optical pulse experiences changes in both the spectral and temporal domains, unlike the effects demonstrated previously (simulation code seen in Appendix). Here, we choose the case for which SPM effects are much larger than those of dispersion, which means L_{NL} is much greater than L_D. For a fiber with a length of only $0.04L_D$, there are significant changes of the pulse profile and spectrum (see Figure 7(c) and (d)).

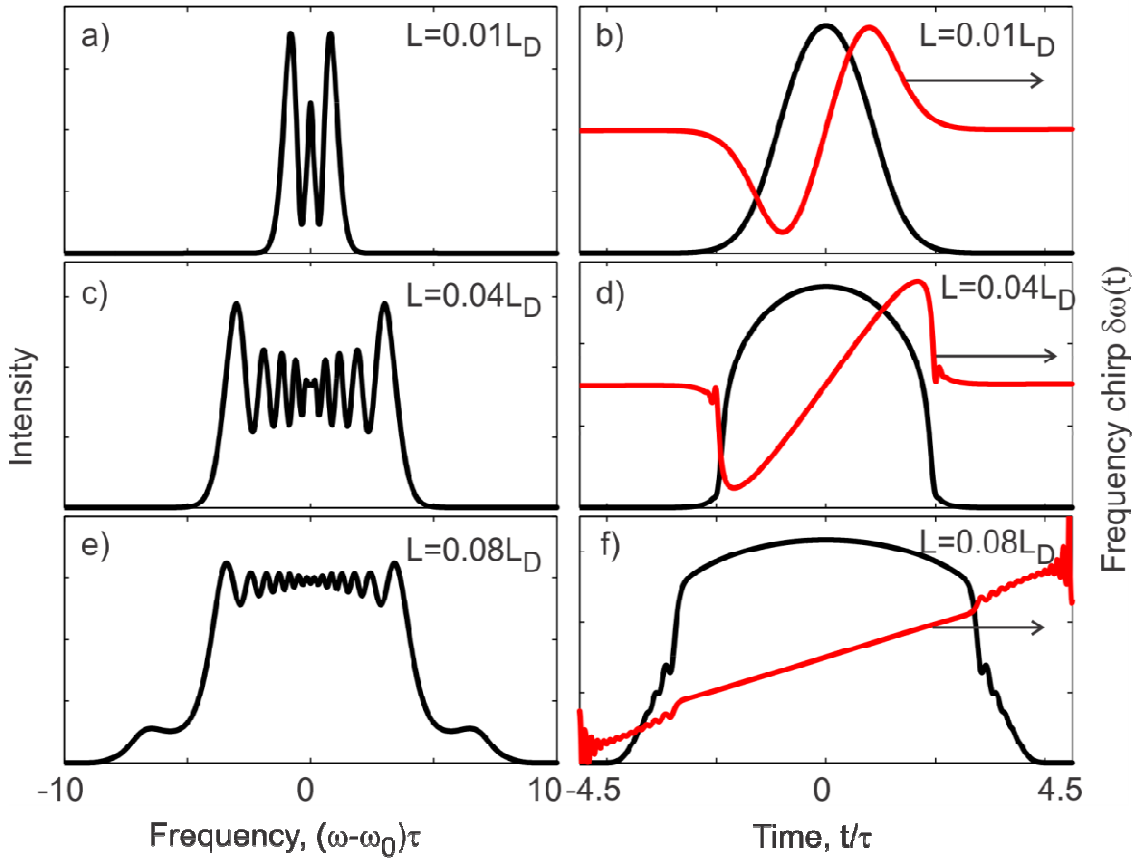

Figure 7: Simulation showing pulse intensity and spectrum after propagating through a fiber with both dispersion and nonlinear refraction. Top: fiber length of $0.01L_D$; middle: fiber length of $0.04L_D$; bottom: fiber length of $0.08L_D$.

As shown in Figure 7(e) and (f), there are oscillations near the edges of the temporal profile and side lobes in the spectrum. This phenomenon is called temporal wave-breaking [26]. This only happens in a normal dispersion fiber where longer wavelengths travel faster. As shown in Figure 5(d), SPM induces frequency chirp. The SPM-induced red-shifted light (negative change of frequency) travels faster, which makes the frequency chirp function steeper while the pulse propagates, see Figure 7(d). Eventually, the red-shifted light can overtake the un-shifted light in the leading edge of the pulse. Then, the lead edge of the pulse contains two frequencies at the same time, which causes interference. Also, blue-shifted light travels slower and is caught by the un-shifted light on the trailing edge. The oscillations near the leading and trailing edges of the

pulse are due to these interferences [26]. It is very important to avoid wave-breaking in fiber laser development, since it breaks one pulse into pieces.

1.3 Introduction to fiber lasers

Not only for optical communication, optical fibers are also used to make lasers [27]. Compared to conventional solid-state lasers, fiber lasers have many advantages. First of all, all light can be confined within the fibers. Thus it is environmentally more stable and insensitive to changes in humidity or temperature. Also no optical alignment is needed, unlike the complicated optical setups of normal solid-state lasers. Meanwhile, the output beam profile can be a pure single mode, without being affected by different powers. This is very important for microscopic imaging or precise micro-machining. Second, due to the large surface-to-volume ratio, the heat dissipation of fiber is much better than that of bulk gain crystals, which enables high power or energy laser delivery without any cooling. Third, because of the large telecom industry, the fabrication of fibers is very well developed and the cost is considerably low. Fourth, fiber lasers can be directly diode pumped. Laser diodes are widely available, inexpensive and compact. The electrical-to-optical efficiency of fiber lasers can be more than 30%. Based on all the advantages mentioned above, fiber lasers have attracted considerable attention in the past two decades. [27-32]

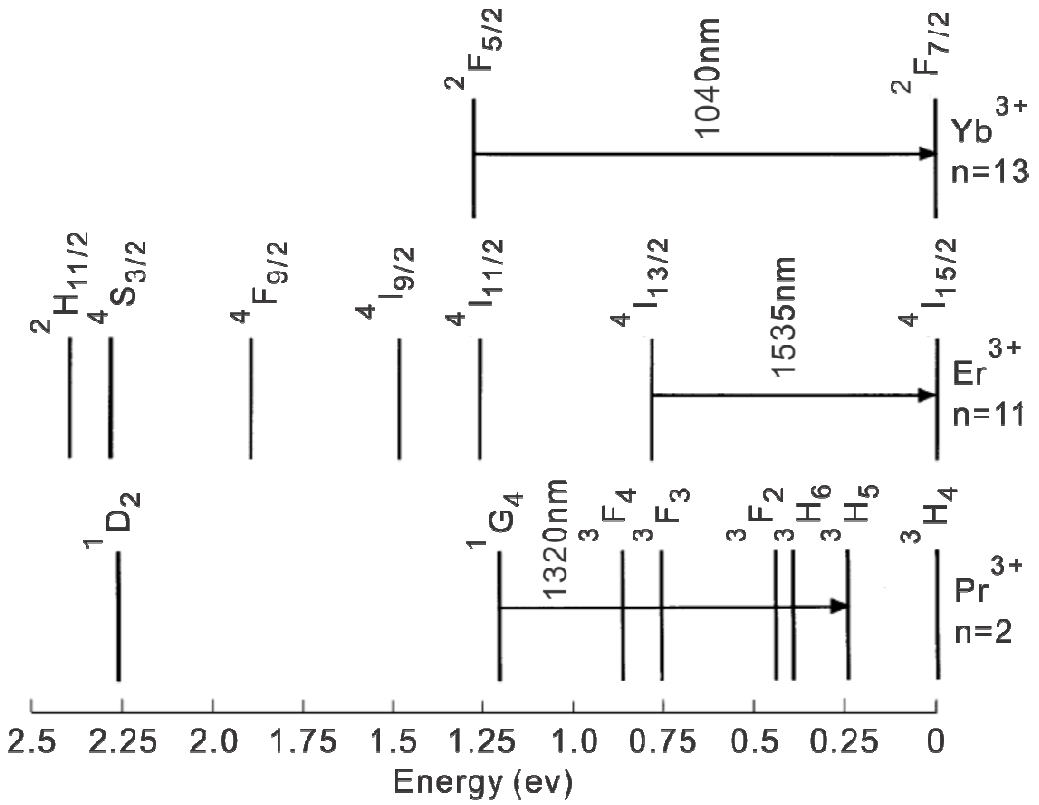

Figure 8: Energy levels of a few isolated 3+ rare earth ions. *n* is the number of electrons in the partially filled 4*f* orbital. [33]

Rare earths or lanthanides are normally used as dopants for most gain fibers. They have a partially filled 4f electron shell, which is shielded from external fields by $5s^2$ and $5p^6$ electrons [18, 33]. The variety of lanthanides also enables a wide range of emission wavelengths, see Figure 8. When doped in an amorphous host, they are triply ionized and through the loss of two 6s electrons and one 4f electron. Due to the shielding from $5s^2$ and $5p^6$ electrons, their ion energy levels or optical properties are largely independent of the host. This is one of the reason that rare earth doped gain fibers are widely used. However, full Stark splitting is observed for rare-earth ions in glasses, due to the low point symmetries of the rare-earth sites in amorphous matrices [33-35]. This leads to more possible transitions than those between the original ion energy levels, see Figure 9 [36]. The Stark levels broaden and overlap to produce an

inhomogeneously broadened emission band [33]. The millisecond long fluorescence lifetime (upper-state time) of lanthanides also results in the need for only a relatively low pump power to maintain a significant population inversion [18], which means a relatively low lasing threshold.

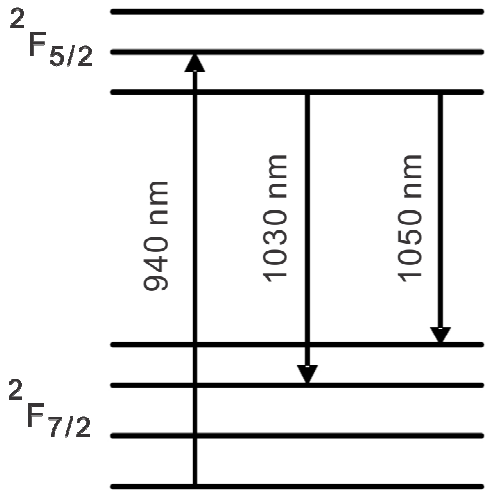

Figure 9: Energy level diagram of Yb3+ ions containing split sub-levels [36]. 940 nm transition is for the pump light, 1030 nm and 1050 nm transitions correspond to the emissions wavelengths.

Depending on the rare earth dopant, emission wavelength varies with different gain fibers. Nd, Er, Tm and Yb doped gain fibers are most commonly used. The first fiber laser was based on a Nd gain fiber [37]. For Er-doped fiber, the emission wavelength is around 1500 nm, which coincides with the minimum loss of silica and is the standard wavelength for optical communication. Tm doped fiber emits around 2000 nm, which is in the near IR and considered an ‘eye-safe’ laser. It has important applications in both medical and sensing technology. As for Yb-gain fiber, the solubility of Yb in glass is much better than Er, which can result in a much higher gain. Also the emission wavelength of Yb is around 1030 nm, which is close to the common diode pump laser wavelength of 976 nm. The Yb gain fiber has very good quantum efficiency and is suitable for making high-power fiber lasers. The average power of a CW Yb fiber laser can be routinely scaled up to 10 kW [38]. Recently, the first commercial 100 kW CW

fiber laser has been developed by IPG Photonics [39]. In the past decade, mode-locking ultrafast fiber lasers have also developed greatly, in terms of both pulse duration and pulse energy. Benefiting from the development of fiber technology, fiber lasers delivering different output pulses such as soliton [40], Gaussian pulse [41] and all-normal-dispersion [31], have been developed. By manipulating cavity dispersion and intra-cavity pulse shaping, different mode-locking regimes can be achieved or switched between.

Soliton fiber lasers were studied and developed in the early years of the history of fiber lasers. John Scott Russell first observed the phenomenon of soliton formation in 1983 [42]. He noticed that solitary waves could form on water and propagate long distances without change in its profile. The optical soliton was studied after the invention of optical fibers and attracted much attention [43]. It was discussed above that the phase distortion induced by dispersion and SPM in a fiber can change the pulses in the temporal or spectral domains or both. In order to support the formation of solitons in a fiber, the phase induced by dispersion needs to balance that of SPM. According to Equation (12), the nonlinear phase shift induced by SPM is always positive. The dispersion can be either positive or negative, depending on the optical wavelength and fiber materials. So, a fiber that has appropriate anomalous dispersion to compensate the positive nonlinear phase shift can support solitons. After solitons are formed, they can propagate a long distance while keeping their spectral and temporal profile unchanged.

Since solitons have zero phase distortion, it should be possible to produce transform-limited pulses directly out of soliton lasers. No extra phase correction or pulse compression is needed, which is ideal for many laser applications. In order to generate soliton-like pulses, anomalous dispersion components are needed in laser cavities and net cavity dispersion must be negative. In a standard solid-state Ti:sapphire laser, prism pairs are normally used to provide

negative dispersion. For fiber lasers, anomalous dispersion fiber can be used. Fox example, normal silica fiber has negative dispersion for wavelength > 1.3 μm. The first soliton fiber laser was demonstrated in 1989 by Kafka et al. [40] and later, an all-fiber soliton laser was developed [29]. Both of them were Er fiber lasers with emission wavelength at 1.5 μm. The pulse evolution through the laser cavity is illustrated in Figure 10 [44]. Soliton pulses take the form

$$U(t) = U_0 \text{sech}(t/\tau)\exp(i\phi) \tag{13}$$

where the FWHM pulse duration $\Delta t = 1.763\tau$. Since soliton results from the cancellation of negative phase due to dispersion and positive phase due to SPM in a negative dispersion cavity, the requirement can be expressed as [18]

$$\frac{L}{L_D} = \frac{L}{L_{NL}} \Rightarrow \frac{\tau^2}{|\beta_2|} = \frac{1}{\gamma P_0}. \tag{14}$$

where L is the length of fiber used in the soliton fiber laser, L_D is the dispersion length, L_{NL} is the nonlinear length, β_2 is second order dispersion, γ is nonlinear coefficient, and P_0 is the peak power of soliton. The peak power P_0 is defined by

$$P_0 = 0.88\frac{E}{\Delta t} = \frac{E}{2\tau}, \tag{15}$$

where E is the soliton pulse energy. Based on Equation (14) and (15), the pulse energy can be presented as

$$E = \frac{2|\beta_2|}{\gamma\tau} = \frac{3.53|\beta_2|}{\gamma\Delta t} = \frac{3.53|D|}{\gamma L\Delta t}, \tag{16}$$

where $D = \beta_2 L$ is total cavity dispersion (negative for soliton fiber laser). Meanwhile, the length of fiber used in solition fiber laser is limited by [18]

$$L = 0.322\frac{\pi\Delta t^2}{|\beta_2|} \Rightarrow \Delta t = \sqrt{|D|}. \tag{17}$$

So the pulse energy E of soliton fiber laser can be approximated by

$$E = \frac{3.53\sqrt{|D|}}{\gamma L}. \tag{18}$$

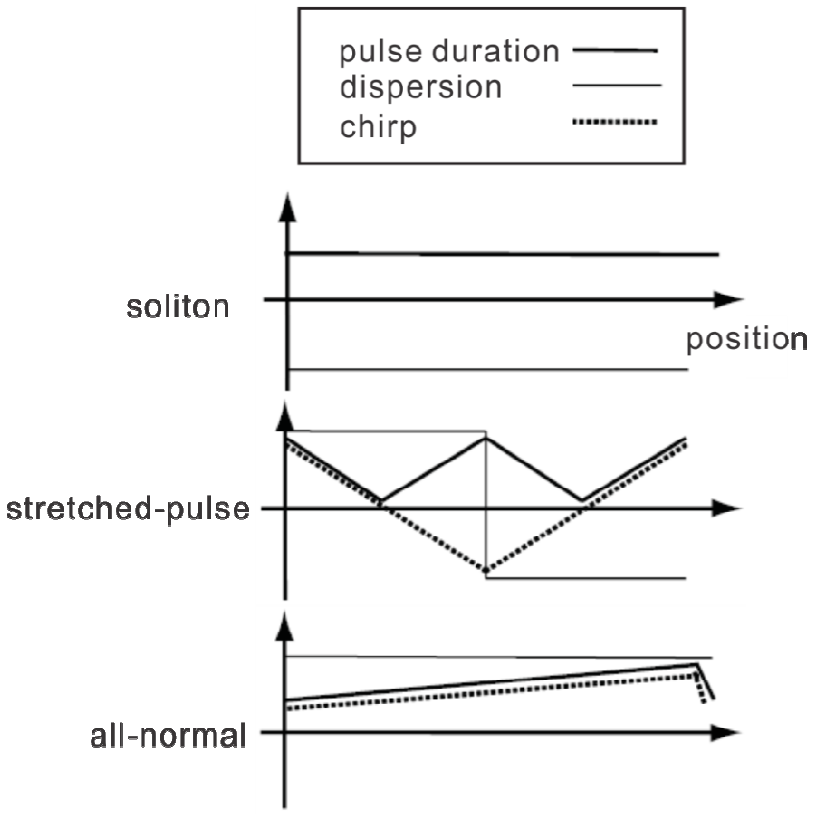

Figure 10: Illustration of pulse evolution in different fiber laser cavities. [44]

Besides cavities with negative net cavity dispersion, fiber lasers with zero net cavity dispersion were also studied. These lasers typically have a normal dispersion component (normal dispersion fiber) and a negative dispersion component (such as anomalous fiber or grating compressor) that compensate each other. So these lasers are also called dispersion-managed or dispersion-mapped fiber lasers. The output pulses have Gaussian profile [45],

$$U(t) = U_0 \exp\left[-\left(t/2\tau\right)^2\right], \tag{19}$$

in contrast to the sech profile of soliton pulses. They are called Gaussian pulses, or stretched-pulses. In this laser, pulses are stretched and compressed twice within each round trip of the cavity, as shown in Figure 10. So there are two locations where the pulses are chirp free or transform-limited, which can be selected as the desired output. The pulse energy and pulse duration of Gaussian pulses can be expressed as [45]

$$E = \frac{4.47\sqrt{|D|}}{\gamma L}, \qquad \Delta t = 0.66\sqrt{|D|}. \tag{20}$$

Unlike previous laser cavities all containing anomalous dispersion components, more recently all-normal dispersion (ANDi) fiber lasers were developed [31]. There is no pulse compression or any component introducing negative dispersion inside the laser cavities. The output pulses are normally highly chirped and can be compressed externally. In order to stabilize the mode-locking, spectral filtering is normally applied in ANDi fiber lasers [44]. This idea was first proposed in Kerr-lens mode-locked solid-state lasers [46, 47]. When an optical pulse is highly chirped, different frequencies are distributed at different positions in the temporal domain. In a positively chirped pulse, red frequency occupies the leading edge while blue frequency occupies the trailing edge. So a spectral filter that blocks red and blue frequencies will also shorten the pulse in the time domain (see Figure 11). Thus, the mode-locking can be stabilized. Otherwise the pulse broadens forever, and the system becomes dissipative and non-self-sustaining.

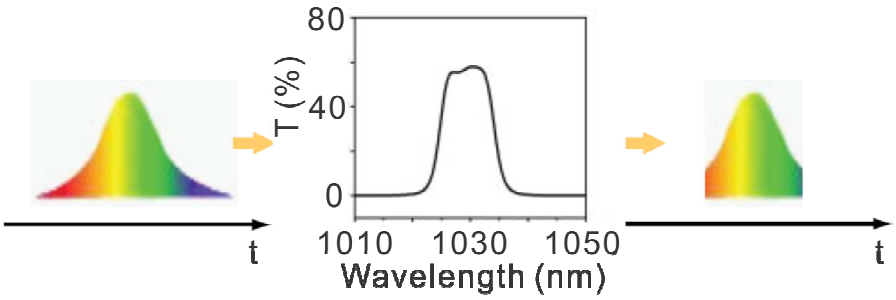

Figure 11: Spectral filtering of highly chirped pulse. T: transmittance.

1.4 Mode-locking methods in fiber lasers

There are two main categories of mode-locking methods. One is active, using acoustic-optic modulators (AOM) and electric-optic modulators (EOM); the other one is passive and uses saturable absorbers or artificial saturable absorbers.

Both AOM- or EOM-aided mode-locking generate up- and down-shifted frequencies. If these newly generated frequencies match the cavity modes, they will be phase locked with the original frequency and all the subsequently generated new frequencies will also be phase-locked. Thus mode-locking is achieved. Another active mode-locking method is seeding the laser with an already mode-locked laser source, which is mostly used in laser amplifiers.

Passive mode-locking usually uses saturable absorbers. A saturable absorber has two main characteristics: intensity-dependent transmission and a fast response time. In solid-state lasers, organic dyes, liquid crystals, and semiconductors are used as saturable absorbers. Among them, a semiconductor saturable absorption mirror (SESAM) is used widely, while the other two have been gradually replaced due to complexity and instability. SESAM is also one of the main types of saturable absorber used in fiber lasers, although it typically has a slower response time and is not suitable for producing very short pulses. Meanwhile, single wall carbon nanotubes (SWCN) and graphene are emerging saturable absorbers, due to their broadband absorption and fast recovery time. [48]

Other than these devices, there are also some artificial saturable absorbers that use nonlinear optical effects, such as Kerr-lens mode-locking used in Ti:sapphire lasers. Due to the optical Kerr effect, the higher the intensity is, the more the refractive index is changed. For a Gaussian beam, the central part has much higher intensity than the edge and will be focused more after a lens. This effect is also called self-focusing. In a Kerr-lens mode-locking laser, a hard or softer aperture is used to favor amplification of the pulsed light over the CW light, since pulsed light has higher peak intensity. For fiber lasers, artificial saturable absorbers based on nonlinear effects are most commonly used due to the large optical nonlinearity in fibers.

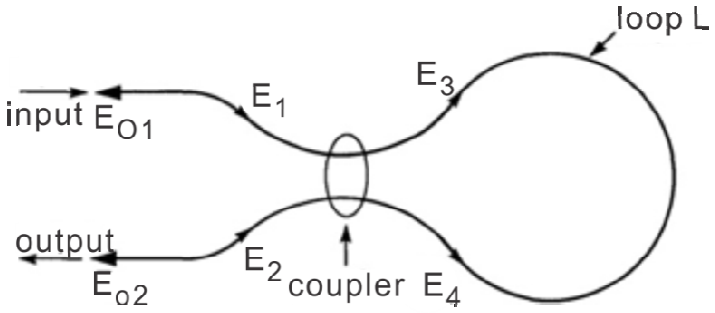

Figure 12: Nonlinear Optical Loop Mirror. [49]

One of the earliest developed fiber artificial saturable absorbers is the nonlinear optical loop mirror (NOLM) [49], based on the principle of nonlinear phase shift. A typical NOLM is shown in Figure 12. The input signal splits to two after going through the coupler. One of the split pulses is going clockwise and the other one is counter-clockwise. Depending on the power of the pulses in each arm, the phase accumulated by going clockwise and counter-clockwise will be different. They will have either constructive or destructive interference with each other at the coupler. By properly adjusting the coupling ratio, NOLM can favor the output of high intensity light, which essentially is the same as Kerr-lens mode-locking.

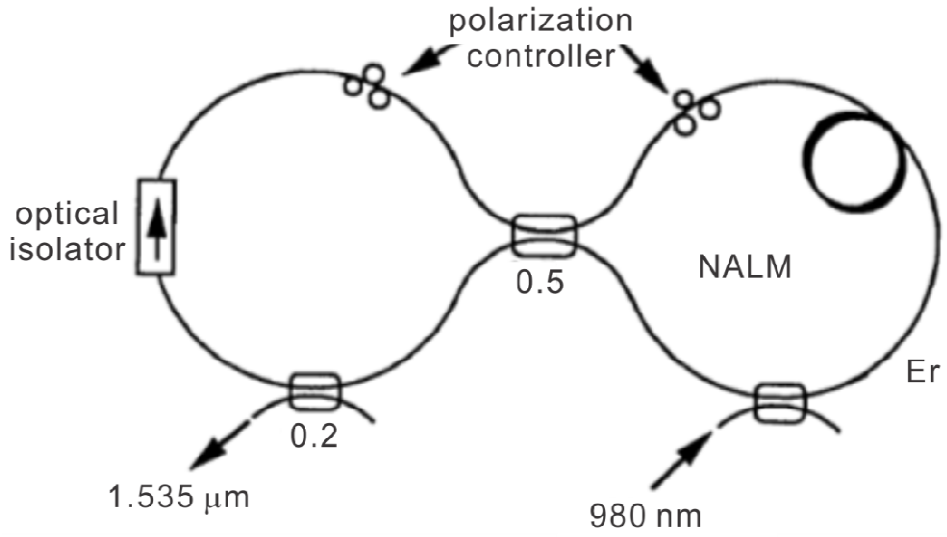

Figure 13: NOLM Fiber laser [29]. NALM: nonlinear amplifying loop mirror.

Figure 13 shows a typical fiber laser using NOLM [29]. A setup of two rings is used and looks like a figure ‘8’, which is why this type of laser is also called a ‘figure-8’ fiber laser. On the right side, a piece of gain fiber is added and a coupler is used to couple the pump laser in. In between two rings, a 50% coupler is used. The left ring is usually called the resonator, and the right one is the NOLM or nonlinear amplifying loop mirror (NALM), since it contains gain fiber. Light from the resonator equally splits and propagates in opposite directions in the NOLM. In the clockwise direction, light goes through a large segment of passive fiber and gets amplified later. For the counterclockwise direction, it is amplified first and gains additional phase shift through the long passive fiber than does the clockwise one. If the phase difference happens to be π, interference will send all the light to the bottom of the resonator where it gets ejected out of the output coupler. The non-pulsed signal, experiencing very little phase difference in the clockwise and counterclockwise directions in the NOLM, is coupled back to the top of the resonator and rejected by the isolator. In this case, the residual signal in the resonator is mainly from the pulsed laser and mode-locking is achieved.

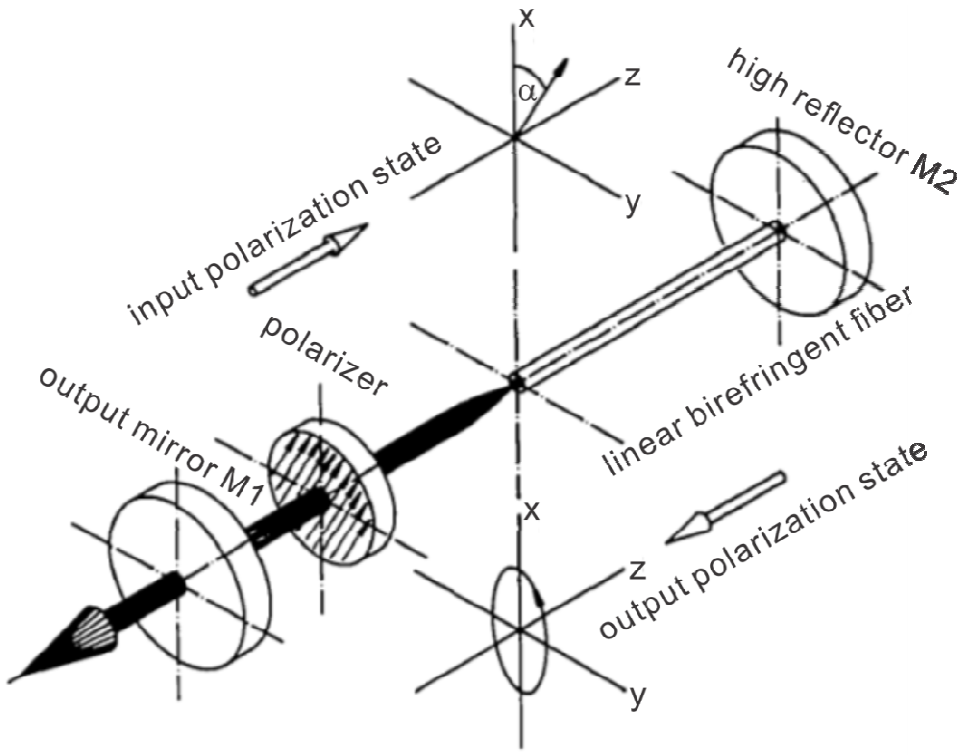

Figure 14: Mode-locked fiber laser based on nonlinear polarization evolution. [50]

Nonlinear polarization evolution (NPE) [50, 51] is another popular mode-locking method used for fiber lasers, see Figure 14. In addition to rotation by the natural birefringence of the fiber, the polarization of the input light is also rotated by the effects of SPM and XPM. As mentioned above, SPM induces an intensity-dependent nonlinear phase shift. XPM also introduce a nonlinear phase shift to the optical pulse induced by a second propagating pulse either with different wavelength or a different polarization. The total nonlinear phase shift caused by SPM and XPM is approximately given by

$$\phi_{NL} = \frac{2\pi}{\lambda} n_2 L\left(\left|E_1\right|^2 + 2\left|E_2\right|^2\right). \tag{21}$$

where E_1 and E_2 are the electric fields in two orthogonal polarization orientations. The difference between the phase shifts of the two orthogonal polarization components is defined by

$$\Delta\phi = \frac{2\pi L}{\lambda}\frac{n_2}{3}\left(|E_1|^2 - |E_2|^2\right). \quad (22)$$

An input optical pulse, with either multiple frequencies or polarization not along the axis of the fiber, will change its polarization in ellipticity and angle (see Figure 14), which is frequency or intensity-dependent. By applying a polarizer after the fiber output, intensity dependent transmission can be achieved, just like in Kerr-lenses or NOLM artificial saturable absorbers.

Among all the mode-locking methods mentioned above, SESAM, SWCNT and NOLM are most favorable for all-fiber lasers. NPE is more often used for fiber lasers with free space components, especially for producing high pulse energy and ultrashort pulse duration. Active mode-locking is mainly used for picosecond fiber laser.

1.5 Ultrashort Pulse Compression

Due to the dispersion and the nonlinear phase shift, the output of an ultrafast fiber laser can have a significant amount of phase distortion. It becomes very important to compensate phase distortions and compress the pulse to its transform-limited duration for most applications. There are many approaches used for pulse compression, such as grating compressors, prism compressors, chirped mirrors, and fiber Bragg gratings. These passive compressors are quite simple to assemble and easy to implement, but they are not able to compensate higher-order phase distortions. In order to do so, active pulse compressors such as pulse shapers [52] are used. A pulse shaper is a device to shape the optical pulse, either spatially or temporally. A normal pulse shaper is illustrated in Figure 15, which is also called 4-*f* pulse shaper. It consists of two gratings, two lenses and one mask in the Fourier plane. This mask can be used as either for phase or amplitude modulation or both of them. Without the mask, it just acts as a grating compressor.

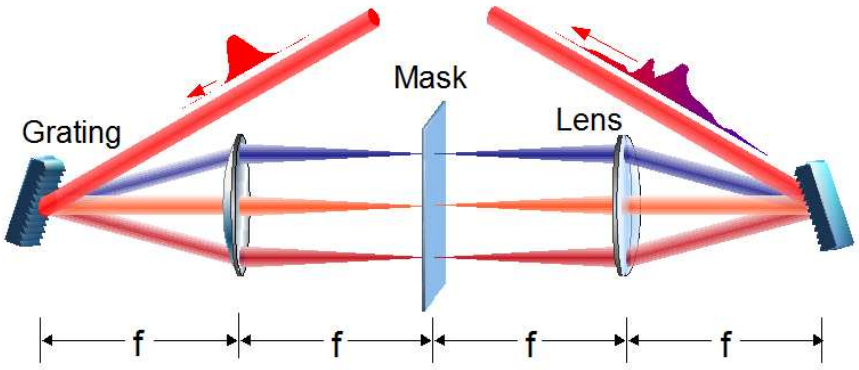

Figure 15: Schematic of a 4-f pulse shaper.

As shown in Figure 15, when the distance between grating and lens (L) is less than the focal length (f), it behaves as a pulse stretcher, where red frequencies come ahead of blue frequencies. In the case of $L>f$, it becomes a pulse compressor. However, this layout will cause some spatial chirp in the output pulses, which is unwanted. So, it is better to keep the shaper at a 4-*f* layout. The 4-*f* scheme can be modified by folding the setup at the Fourier plane using a reflection mirror. Lenses can also be replaced by curved mirrors.

With the development of liquid crystal based spatial light modulators (LC-SLM), it became possible to make adaptive corrections rather than using fixed masks [52]. By applying certain voltages to the pixels of liquid crystal arrays, the liquid crystals rotate and act as birefringent materials. In the Fourier plane, frequencies focused on to different LC arrays accumulate corresponding phase retardance. This applied phase is called the spectral phase and does not change the output spectrum. However, the pulse is modified in the temporal domain.

Based on this technique, the Dantus research group developed a pulse characterization and compression method – multiphoton intrapulse interference phase scan (MIIPS) [53-55]. By adding a defined spectral phase to the laser spectrum and measuring the resulting change in the SHG signal, the phase distortion in the original pulse can be determined. The principle of the

method is based on nonlinear interference, which depends on the spectral phase, and cause changes in the SHG spectrum. The electric field of a pulse can be written as

$$E(\omega) = \left|E(\omega)\right| \exp(i\phi(\omega)), \tag{23}$$

where $E(\omega)$ is the electric field of the pulse in frequency domain, and $\phi(\omega)$ is the spectral phase of the pulse. If this pulse is focused into a SHG crystal, the generated SHG signal can be presented by

$$\begin{aligned} I(2\omega) &= \left| \int \left|E(\omega+\Delta)\right| \left|E(\omega-\Delta)\right| \exp\left(i\left(\phi(\omega+\Delta)+\phi(\omega-\Delta)\right)\right) d\Delta \right|^2, \\ \phi(\omega+\Delta) &= \phi_0 + \phi'(\omega)\Delta + \frac{1}{2!}\phi''(\omega)\Delta^2 + \frac{1}{3!}\phi'''(\omega)\Delta + O\left(\Delta^4\right), \\ \phi(\omega-\Delta) &= \phi_0 - \phi'(\omega)\Delta + \frac{1}{2!}\phi''(\omega)\Delta^2 - \frac{1}{3!}\phi'''(\omega)\Delta + O\left(\Delta^4\right), \\ \phi(\omega+\Delta) &+ \phi(\omega-\Delta) = 2\phi_0 + \phi''(\omega)\Delta^2 + O(\Delta^4), \end{aligned} \tag{24}$$

$$I(2\omega) = \left| \int \left|E(\omega+\Delta)\right| \left|E(\omega-\Delta)\right| \exp\left(i\left(2\phi_0 + \phi''(\omega)\Delta^2 + O(\Delta^4)\right)\right) d\Delta \right|^2, \tag{25}$$

where $I(2\omega)$ is the SHG signal, Δ is the frequency deviation from ω and the variable of integration, and ϕ_0, $\phi'(\omega)$, $\phi''(\omega)$ and $\phi'''(\omega)$ are the zero order, first order, second order and third order derivatives of the spectral phase $\phi(\omega)$, respectively. According to Equation (25), the SHG signal $I(2\omega)$ is maximized when $\phi''(\omega) = 0$.

When a reference phase $\phi_{ref}(\omega)$ is introduced, the SHG intensity at certain frequency is maximized when

$$\phi''(\omega) = -\phi''_{ref}(\omega), \tag{26}$$

where ω is the angular frequency, $\phi''(\omega)$ is the second derivative of the original phase of input pulses, and $\phi''_{ref}(\omega)$ is the second derivative of the reference phase. Normally a sinusoidal

reference phase or second order dispersion phase is applied, as defined by either of the two expressions, respectively:

$$\begin{aligned} \phi_{ref}(\omega) &= \alpha \cos\left(\gamma(\omega-\omega_0)+\delta\right), \\ \phi_{ref}(\omega) &= \frac{1}{2}\beta_2(\omega)(\omega-\omega_0)^2, \end{aligned} \tag{27}$$

where α is a modulation amplitude with value around 2π, γ is the FWHM pulse duration of transform-limited pulse, δ is the scanning phase parameter, and β_2 is the scanning second order dispersion. The SHG signal will be maximized when

$$\begin{aligned} \varphi''(\omega) &= \alpha\gamma^2 \cos\left(\gamma(\omega-\omega_0)+\delta_{\max}(\omega)\right), \\ \varphi''(\omega) &= -\beta_2{}^{\max}(\omega). \end{aligned} \tag{28}$$

In the case of a transform limited pulse, $\varphi''(\omega)$ is 0 and

$$\begin{aligned} \delta_{\max}(\omega) &= (2n\pm1)\frac{\pi}{2}-\gamma(\omega-\omega_0), \\ \beta_2{}^{\max}(\omega) &= 0, \end{aligned} \tag{29}$$

where $\delta_{\max}(\omega)$ and $\beta_2{}^{\max}(\omega)$ are the scanning parameters corresponding to the local maximum SHG signal. It can be easily noticed that $\delta_{\max}(\omega)$ is simply a straight line with slope of γ and repeats every π; $\beta_2{}^{\max}(\omega)$ is simply a horizontal line equal to zero. If there is second order phase dispersion, then $\varphi''(\omega)$ is a non-zero constant. $\delta_{\max}(\omega)$ is still a straight line but the spacing becomes smaller or larger than π; and $\beta_2{}^{\max}(\omega)$ is just a constant meaning a straight line across all frequencies. With higher order dispersions, the functions will change correspondingly, as illustrated in Figure 16.

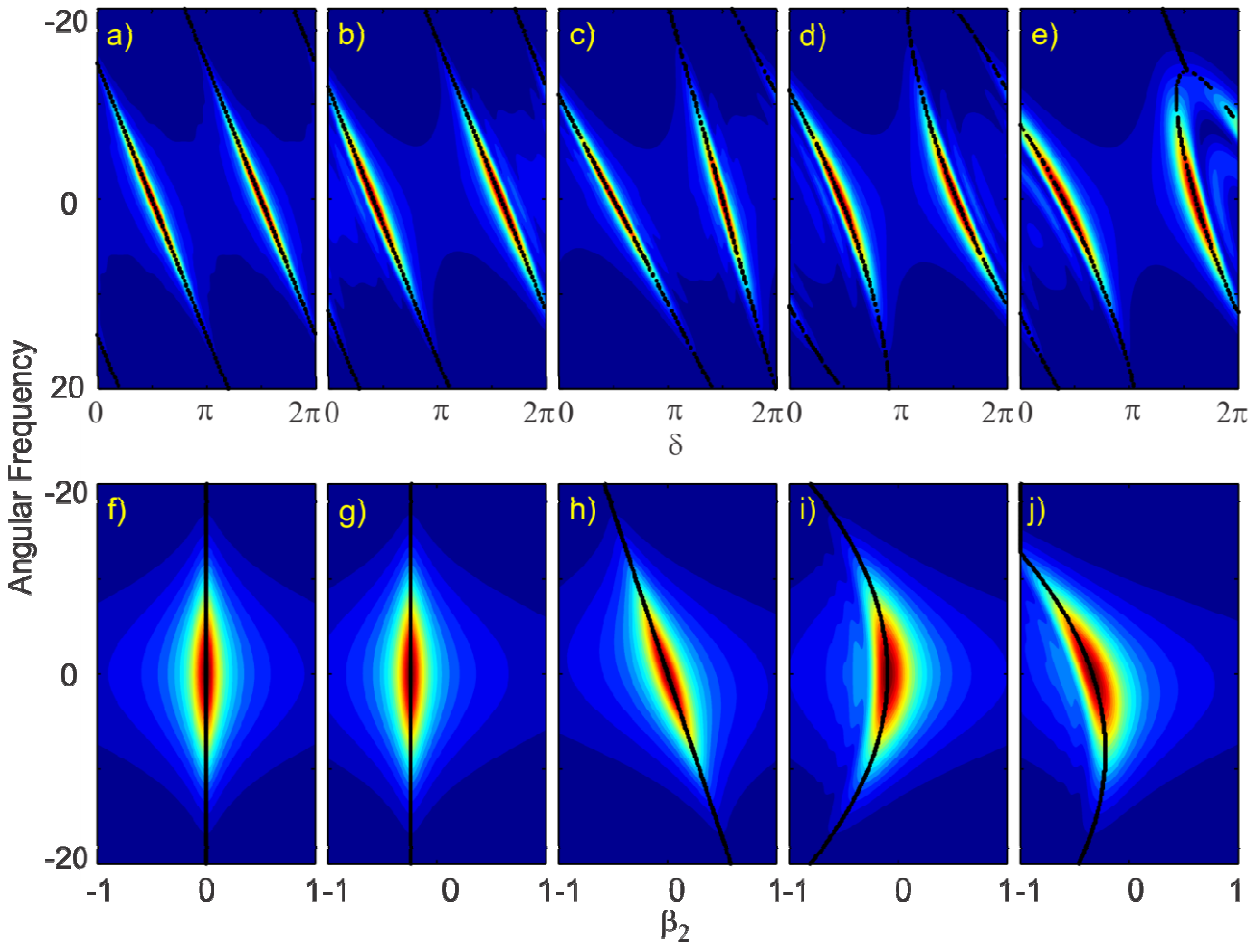

Figure 16: MIIPS simulation results. Top: sinusoidal scan of pulses with (a) flat phase, (b) second order dispersion, (c) third order dispersion, (d) fourth order dispersion and (e) all of them; bottom: second order dispersion scan of pulses with (f) flat phase, (g) second order dispersion, (h) third order dispersion, (i) fourth order dispersion and all (j) of them. Dot lines: local maxima of SHG signal.

Chapter 2 Sub-50 fs High Energy Ultrafast Fiber Laser

This chapter discusses the development of sub-50 fs fiber lasers producing tens of nJ pulse energy, which achieved the highest peak power of the pulses from a single-mode fiber laser. Different cavity designs are discussed. Dependence of laser performance on several key cavity parameters is studied. Both simulation and experimental results are demonstrated.

2.1 Introduction

One principal application of ultrafast fiber lasers is biomedical imaging, such as multiphoton microscopy [6]. It is known that multiphoton efficiency is dependent on pulse duration [56]. As shown in Figure 17, the SHG signal is inversely proportional to the laser pulse duration and the THG is inversely proportional to pulse duration squared [Figure 17] [57].

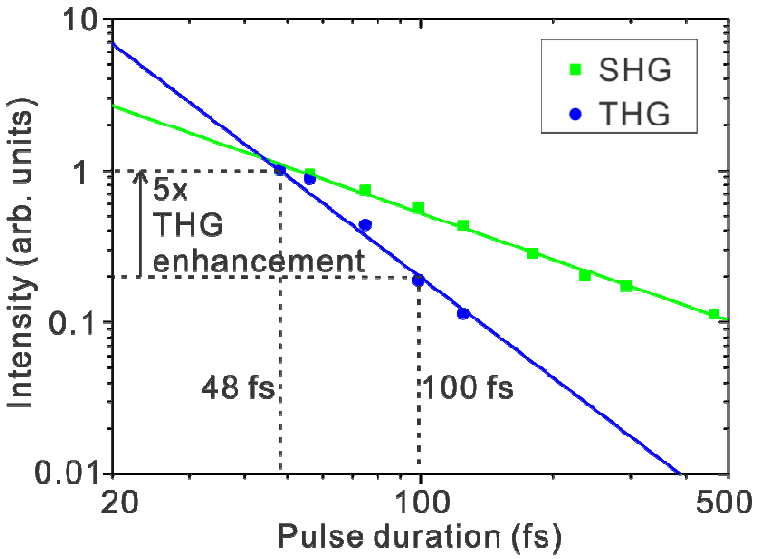

Figure 17: Pulse duration dependent multiphoton efficiency. Symbols: experimental results; Lines: fit of experimental data.

It is clear that shorter pulses increase the multiphoton signal. On the other hand, in order to image biological samples, laser pulses need to overcome the large loss from tissue scattering. So a fiber laser that can provide both ultrashort pulse duration (sub-50 fs) and high pulse energy

(tens of nJ) is highly desirable for this application. As discussed in Chapter 1, there are several types of fiber laser designs. A proper design needs to be chosen to produce pulses as mentioned above.

Intuitively, a soliton or Gaussian pulse fiber laser is considered as the first option, since both of them can deliver transform-limited pulses. It is known that pulse energy E and FWHM pulse duration Δt of soliton pulses are approximately [45]

$$E = \frac{3.53\sqrt{|D|}}{\gamma L}, \qquad \Delta t = \sqrt{|D|}, \tag{30}$$

or

$$\frac{E}{\Delta t} = \frac{3.53}{\gamma L}, \tag{31}$$

where D is the net cavity dispersion (usually negative), γ is the nonlinear coefficient, and L is total fiber length in laser cavity. As shown in Equation (30), the larger the net cavity dispersion, the higher the pulse energy and the longer the pulse duration. In other words, pulse duration is proportional to pulse energy. For a typical 100 MHz soliton fiber laser using about 2 m long 6μm core diameter fiber operating at 1.5 μm wavelength, the ratio between pulse energy and pulse duration or peak power is limited to about 400 W according to Equation (31). This means that a 100 fs pulse from a soliton fiber laser can only contain about 40 pJ of energy, which is too low for most imaging applications. While a 10 ps soliton pulse can deliver 4 nJ pulse energy, the pulse duration is too long. Therefore, soliton fiber lasers would be ideal for producing transform-limited picosecond pulses, which is not suitable for biomedical imaging. This limitation can also be understood as follows. Since soliton pulses are transform-limited through the whole laser cavity, the corresponding peak power will be very high for femtosecond pulses with nJ pulse

energy. This will cause significant high order nonlinear effects such as self-steepening, stimulated Raman scattering and even self-focusing (for peak power larger than 6 MW). Soliton propagation cannot be sustained under those conditions.

For Gaussian pulse fiber lasers, pulse energy and pulse duration can be expressed as

$$E = \frac{4.47\sqrt{|D|}}{\gamma L}, \qquad \Delta t = 0.66\sqrt{|D|}, \tag{32}$$

or

$$\frac{E}{\Delta t} = \frac{6.77}{\gamma L}. \tag{33}$$

According to the energy-to-pulse-duration ratio, Gaussian pulses can deliver about twice the pulse energy as soliton pulses with the same pulse duration. This higher pulse energy is attributed to partial stretching of the pulses due to the normal dispersion components. However, the pulse energy for femtosecond pulses is still not high enough.

Different from soliton and Gaussian pulse fiber lasers, all-normal dispersion fiber lasers have pulses that are highly chirped through the entire cavity; and higher pulse energy can be tolerated without generating significant nonlinear effects in fibers, so an all-normal dispersion fiber laser is a better option for high pulse energy delivery. On the other hand, Yb fiber lasers are favored for high power fiber laser designs. The emission wavelength is around 1 μm, fused silica has normal dispersion at this wavelength. Therefore, the output pulses of all-normal dispersion fiber lasers usually have significant phase distortion since there is no dispersion compensation inside the cavity. External pulse compression is needed for this type of lasers. The maximum nonlinear phase shift experienced by pulses in a normal dispersion cavity can be as large as ~10π [58], compared to only ~π in soliton and Gaussian pulse fiber lasers [44]. In previous report [59],

pulse energy as high as 31 nJ was delivered from an all-normal dispersion fiber laser. The output pulses were compressed to about 80 fs FWHM pulse duration, resulting in a peak power of 200 kW. It is desirable to explore the limit of this fiber laser design in terms of the pulse energy, the pulse duration and the peak power.

2.2 All-normal dispersion fiber laser

2.2.1 Experimental setup

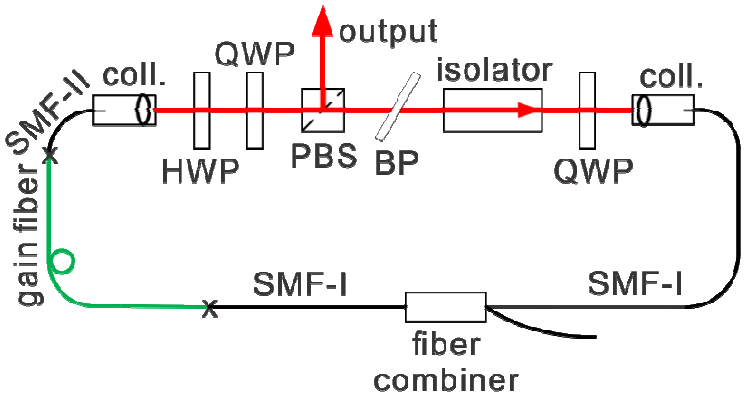

Figure 18: Schematic of an all-normal dispersion fiber laser. PBS: polarizing beam splitter; QWP and HWP: quarter- and half-wave plate respectively; SMF: single mode fiber; coll.: fiber collimator; SF: spectral filter.

A typical all-normal dispersion fiber laser is illustrated in Figure 18. It has a ring cavity with some free-space components used. A pump laser (976 nm laser diode) is coupled into an Yb doped gain fiber by a fiber combiner. The gain fiber used here is a double-clad fiber with 10 μm core diameter (CorActive, 6 dB/m absorption @ 975 nm). The pump laser is delivered by a 100 μm core diameter multi-mode fiber and coupled into the inner cladding of the gain fiber. The excess pump laser is forced to leak out by applying index-matching gel at the end of gain fiber. Two segments of passive single mode fiber (SMF-I and SMF-II) are fusion spliced to gain fiber using a fiber splicer (Fujikura LMA-PM-400). Two fiber collimators are used to couple the input and output light of the fiber, respectively. Several quarter- and half-wave plates are used to help

the mode-locking based on nonlinear polarization evolution (NPE). The polarizing beam splitter (PBS) acts as an output coupler and is also part of the NPE mode-locking. The isolator is a very important component. It establishes the direction of the laser propagation and prevents damage to the gain fiber. If even a small amount of light couples back to the gain fiber, it can destroy the fiber cavity due to the high gain. A spectral filter is used to stabilize the mode-locking. In principle, all the free-standing components mentioned above can be replaced by all-fiber components. For example, the wave plates can be easily replaced with a fiber polarization controller. By adding forces to a non-polarization maintaining fiber, the birefringence of the fiber can be easily changed. Thus the polarization of the output light will also be changed. The PBS can be replaced with a fiber coupler. However, our research focuses on developing the concept of a fiber laser design instead of engineering an integrated all-fiber laser. (Detailed fiber laser cavity alignment is presented in the Appendix.)

The principles behind using each of these components to achieve mode-locking is described below.

2.2.1.1 Nonlinear polarization evolution

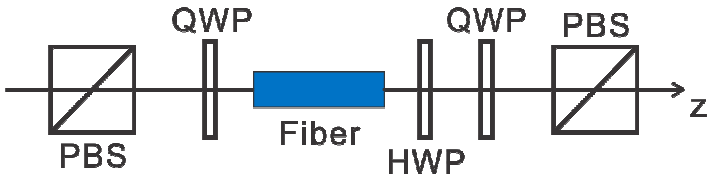

Figure 19: Schematic of artificial saturable absorber. PBS: polarizing beam splitter, HWP and QWP: half- and quarter-wave plate, and +*z* is the pulse propagation direction. Note: color has no meaning in this figure.

As mentioned in Chapter 1, a fiber laser can be mode-locked using an artificial saturable absorber based on NPE of the optical field in the fiber. A schematic of the artificial saturable

absorber used in our laser is shown in Figure 19. It is formed by a PBS, three wave plates, and the fiber.

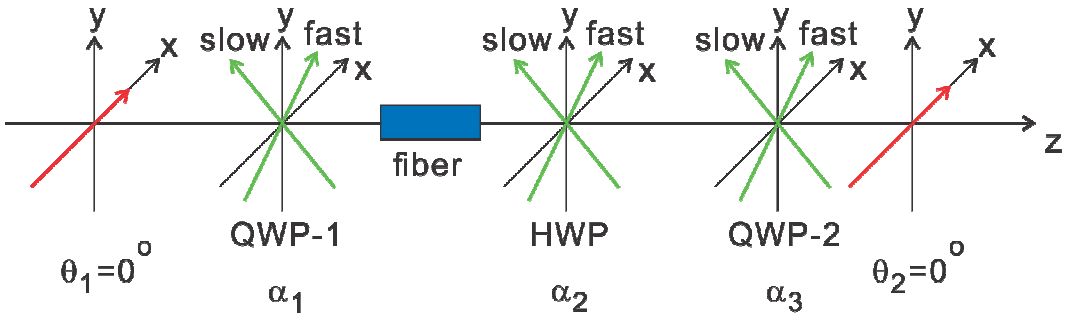

Figure 20: Illustration of propagation of electric field through the artificial saturable absorber. α_1, α_2, α_3 are the angles between the fast axis of the wave plates and the x-axis, θ_1 and θ_2 are the angles between the axis of the polarizers and the x-axis, *x*, *y*, *z* are the coordinate axes, and +*z* is the pulse propagation direction. Note: color has no meaning in this figure.

As shown in Figure 20, a pulse after the PBS is horizontally polarized. The input optical field E_0 is

$$E_0 = a\begin{pmatrix}1\\0\end{pmatrix}, \tag{34}$$

where *a* is the amplitude of the input optical field. Due to cross-phase modulation (XPM), the phase change for each frequency through the fiber can be written as

$$\Delta\phi(\omega) = \frac{2\pi L}{\lambda}\frac{n_2}{3}\left(\left|E_+(\omega)\right|^2 - \left|E_-(\omega)\right|^2\right). \tag{35}$$

where L is the length of the fiber, λ is the wavelength of the input pulse, n_2 is the nonlinear refractive index, and E_+ and E_- are the electric field of the two orthogonal polarization components along the fast and slow axes of the fiber, respectively. Here, we assume that the fast axis of the fiber is along *x* axis and the slow axis of the fiber is along *y* axis. The evolution of the

electric field through these components can be calculated using Jones vectors. Two simple results are shown below,

$$\text{If } \alpha_1 = 0, \alpha_2 = 0, \alpha_3 = 0, I_{out}(\omega) = a^2 \sin^2\left(\Delta\phi(\omega)\right). \tag{36}$$

$$\text{If } \alpha_1 = \frac{\pi}{4}, \alpha_2 = \frac{\pi}{4}, \alpha_3 = \frac{\pi}{4}, I_{out}(\omega) = a^2\left(1+\cos\left(\Delta\phi(\omega)\right)\right). \tag{37}$$

So, by rotating these wave plates, the transmission function of this setup varies. With fixed wave plate angles, the transmittance of each frequency is different, depending on their intensities and input polarizations. Thus, by properly adjusting the wave plates, the coupling and amplification of frequencies with high intensity can be favored t. After a number of round trips, mode-locking can be achieved.

2.2.1.2 Spectral filter

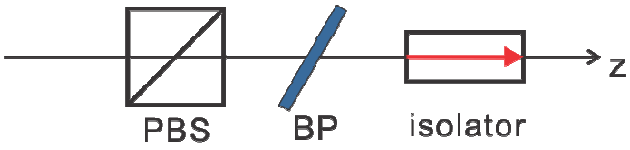

Figure 21: Illustration of spectral filter. PBS: polarizing beam splitter, BF: birefringent plate, and +*z* is the pulse propagation direction.

The spectral filter is another very important component in this cavity. It is formed by a birefringent quartz plate placed between the PBS and the isolator (see Figure 21). The ordinary axis of the birefringent plate is at 45° with the respect to the horizontal axis in the plane perpendicular to the beam propagation direction. The plate is also tilted at the Brewster angle to reduce reflection loss. Meanwhile, the polarization of the input port of the isolator is set as horizontal. The input light from the PBS is horizontally polarized. Then we can get the equations below,

$$
\begin{aligned}
&\vec{E}_{in} = E_0\hat{e}_x = \frac{2}{\sqrt{2}}E_0\hat{e}_0 + \frac{2}{\sqrt{2}}E_0\hat{e}_e,\\
&\vec{E}' = \frac{2}{\sqrt{2}}E_0\hat{e}_0 + \frac{2}{\sqrt{2}}E_0\hat{e}_e \cdot e^{-i\Delta\phi},\\
&\vec{E}' = \frac{2}{\sqrt{2}}E_0(\frac{2}{\sqrt{2}}\hat{e}_x + \frac{2}{\sqrt{2}}\hat{e}_y) + \frac{2}{\sqrt{2}}E_0(\frac{2}{\sqrt{2}}\hat{e}_x - \frac{2}{\sqrt{2}}\hat{e}_y)\cdot e^{-i\Delta\phi},\\
&\vec{E}' = E_0\cos(\frac{\Delta\phi}{2})e^{-i\frac{\Delta\phi}{2}}\hat{e}_x + \cdots\hat{e}_y,\\
&E_{out} = E_0\cos(\frac{\Delta\phi}{2})e^{-i\frac{\Delta\phi}{2}}\hat{e}_x.
\end{aligned}
\tag{38}
$$

where $\vec{E}'$ is the electric field after the birefringent plate. The transmission function of the output pulse can be written as below,

$$
\begin{aligned}
&I_{out} = E_0\cos^2(\frac{\Delta\phi}{2}),\\
&\Delta\phi = \frac{2\pi}{\lambda}(n_e - n_o)d.
\end{aligned}
\tag{39}
$$

where n_e and n_o are the refractive indices of extra-ordinary and ordinary axes of the birefringent quartz plate, I_{out} is the pulse intensity after the spectral filter.

Here, n_e and n_o are 1.53514 and 1.54392 at 1 μm, respectively. Using the Equations (39) and the refractive indices, transmittance curves for different thicknesses of birefringent plates are plotted in Figure 22. It shows that, the setup with a 3 mm thick birefringent plate corresponds to a 20 nm FWHM bandwidth spectral filter, and the one with a 5 mm thick birefringent plate has a FWHM spectral bandwidth of 12 nm. By rotating the axis of the spectral filter or changing the input or output polarization axis of the polarizers, the wavelength of the peak transmittance can be shifted.

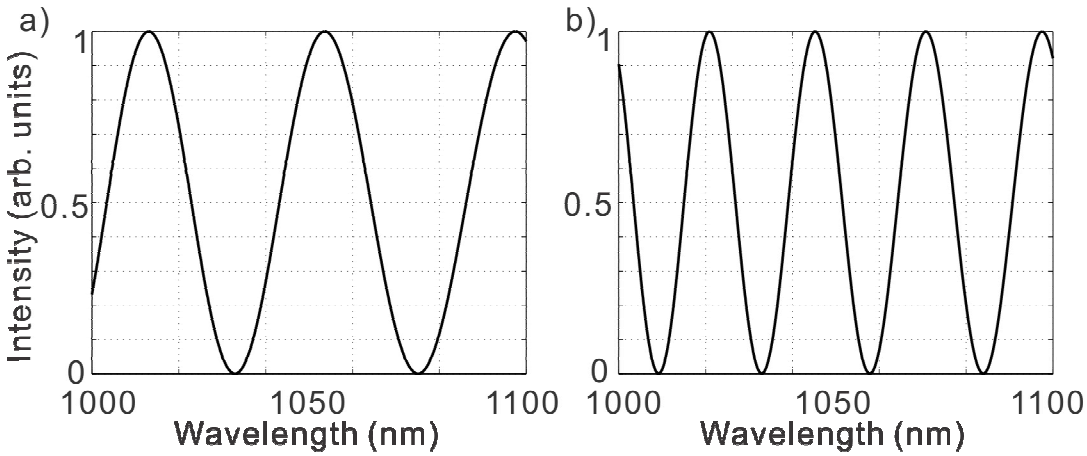

Figure 22: Transmittance of spectral filter using a) a 3 mm thick birefringent plate and b) a 5 mm thick birefringent plate

The spectral filter plays a very important role in stabilizing mode-locking. Initially by adjusting the filter, only the desired spectral range is amplified in the gain fiber. After amplification, high intensity pulse induced SPM will generate new frequencies and broaden the spectrum. After each loop, the filter-induced loss of both spectral bandwidth and pulse energy also balances the gain, which keeps the laser producing stable output pulses. Meanwhile, due to the cavity dispersion (here we only discuss the case of normal dispersion), the generated red frequencies lead the pulse and the blue frequencies lag the pulse. This dispersion broadens the pulse duration. By applying the spectral filter, it not only cuts the spectral bandwidth, but also shortens the pulse in the temporal domain. Other ways in which the spectral filter affects the laser performance will be discussed later in this chapter.

2.2.2 Experimental results and discussion

For the initial operation of the laser, the pump power should be set at a low level and the alignment of the setup is adjusted by monitoring the output power. The most critical thing is the coupling between two fiber collimators. Both angle and height need to be adjusted. Once enough coupling efficiency is reached, the cavity will start lasing and output power will increase

dramatically. Then, finer adjustment can be done to maximize the output power in CW mode. The isolator has to be placed in between the two collimators all the time. Otherwise, the gain fiber will be easily damaged.

Various mode-locking patterns can be obtained by varying the pump power and rotating the wave plates. Typical output pulses from an all-normal dispersion fiber laser are shown in Figure 23. Output pulses with average power of 1.43 W at a repetition rate of 41.2 MHz, corresponding to 34.7 nJ per pulse, are delivered from this laser. Output pulses are highly chirped and compressed to about FWHM 80 fs pulse duration, which already beats the best all-normal dispersion fiber laser (31 nJ and 80 fs) reported previously [59]. The cat-ear like structure of the spectrum is the characteristic of all-normal dispersion fiber laser and is caused by SPM effects. For this demonstrated laser, the parameters are as follows: 2.5 m long SMF-I, 1.9 m long gain fiber, 0.2 m long SMF-II fiber and spectral filter of FHWM 20 nm bandwidth. The gain fiber is pumped at about 6.1 W. Since all the cavity parameters listed above can be adjusted, it is important to study the dependence of the laser performance on these parameters and find proper guidance in cavity design. In the following sections, dependences of laser performance on fiber length and filter bandwidth are mainly discussed.

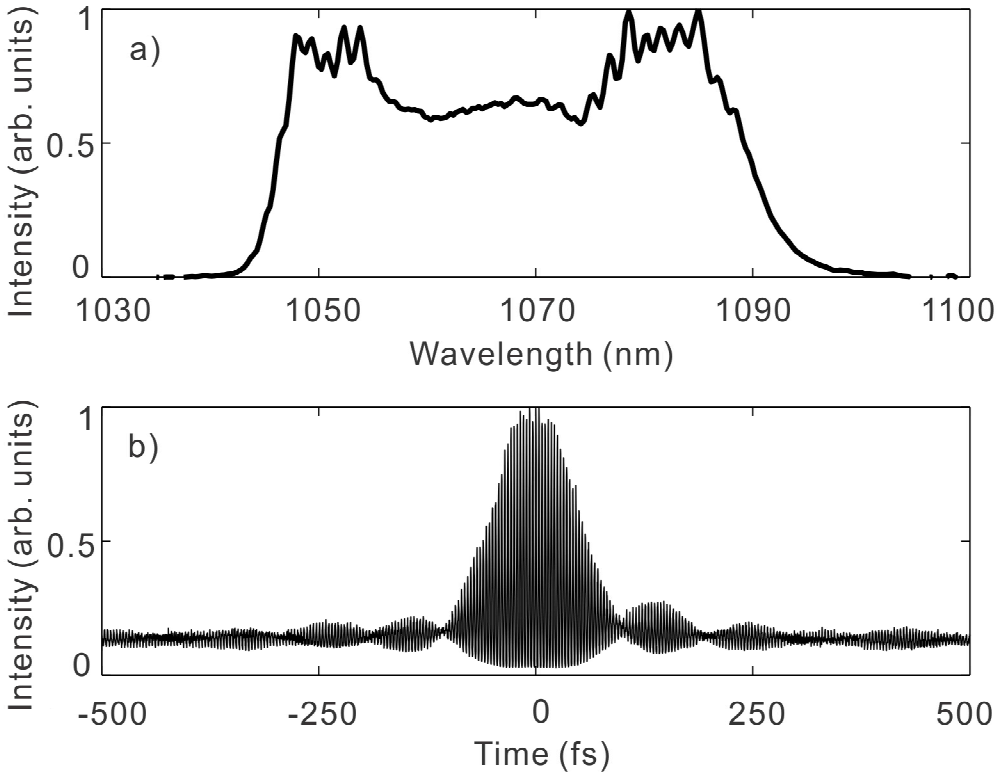

Figure 23: Laser performance of all-normal dispersion fiber laser. (a) Output spectrum; (b) Experimentally measured interferometry autocorrelation of de-chirped output pulses.

2.2.2.1 Fiber length dependence

According to their locations and functions, fibers in the cavity are categorized as SMF-I (passive fiber preceding gain fiber and after spectral filter), gain fiber and SMF-II (passive fiber following gain fiber and before output port).

Normally, the length of gain fiber is chosen to absorb most of the pump light. If the gain fiber is too short, and it will not fully absorb the pump signal. Too long is not good either, since the excess gain fiber absorbs no more pump light but the laser signal instead causing some narrowing. Also it adds more dispersion and nonlinear phase shift to the cavity. Therefore, both excessively long and short gain fiber should be avoided. The proper length can be determined by the absorption rate of the gain fiber, which depends on the density of Yb ion dopant and pump

light wavelength. The gain fiber used here has an absorption rate of 6 dB/m at 975 nm, which means one meter of fiber will absorb about 75% of the pump light. In our system, about 2 m gain fiber is used and the pump-to-laser conversion efficiency can be up to 50% (maximum CW output power divided by the pump power), as shown in Figure 24. Since the length of the gain fiber is not a proper parameter to adjust, the remaining adjustable parameters other than spectral filter bandwidth are the length of SMF-I and SMF-II.

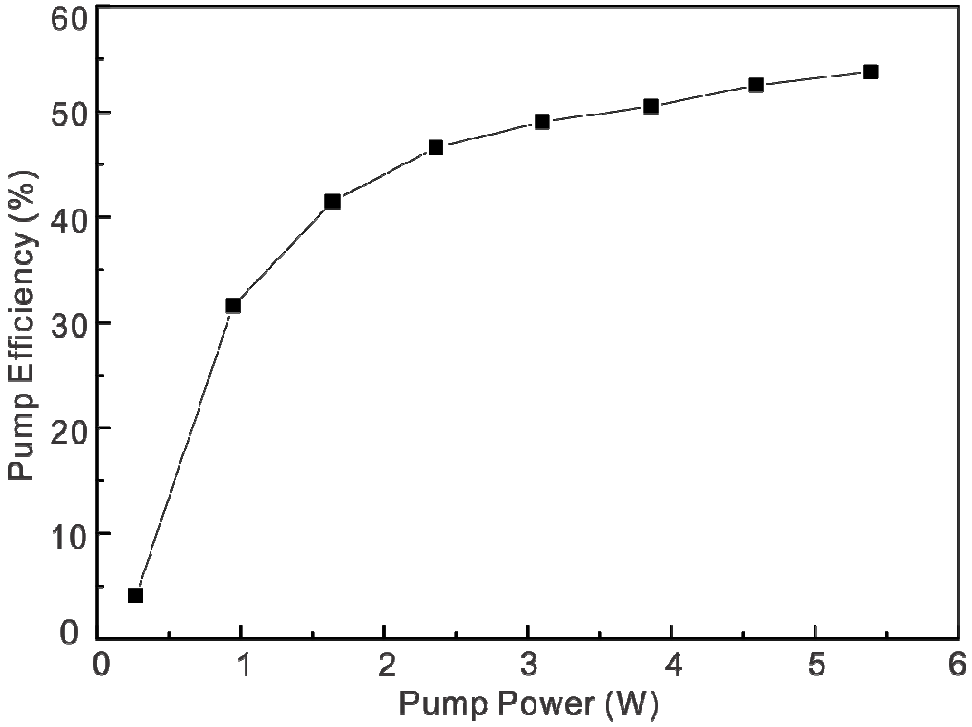

Figure 24: Measured pump-to-laser conversion efficiency.

With other parameters kept the same, the length of SMF-I is changed from 7.5 m to 1.7 m. It is found that the output spectral bandwidth increases with the decrease of SMF-I length, see Figure 25. Shortening SMF-I from 7.5 m to 2.4 m, the output spectra change significantly. However, further reducing SMF-I length does not affect the output spectra much, as seen by comparing the results of 2.4 m and 1.7 m SMF-I.

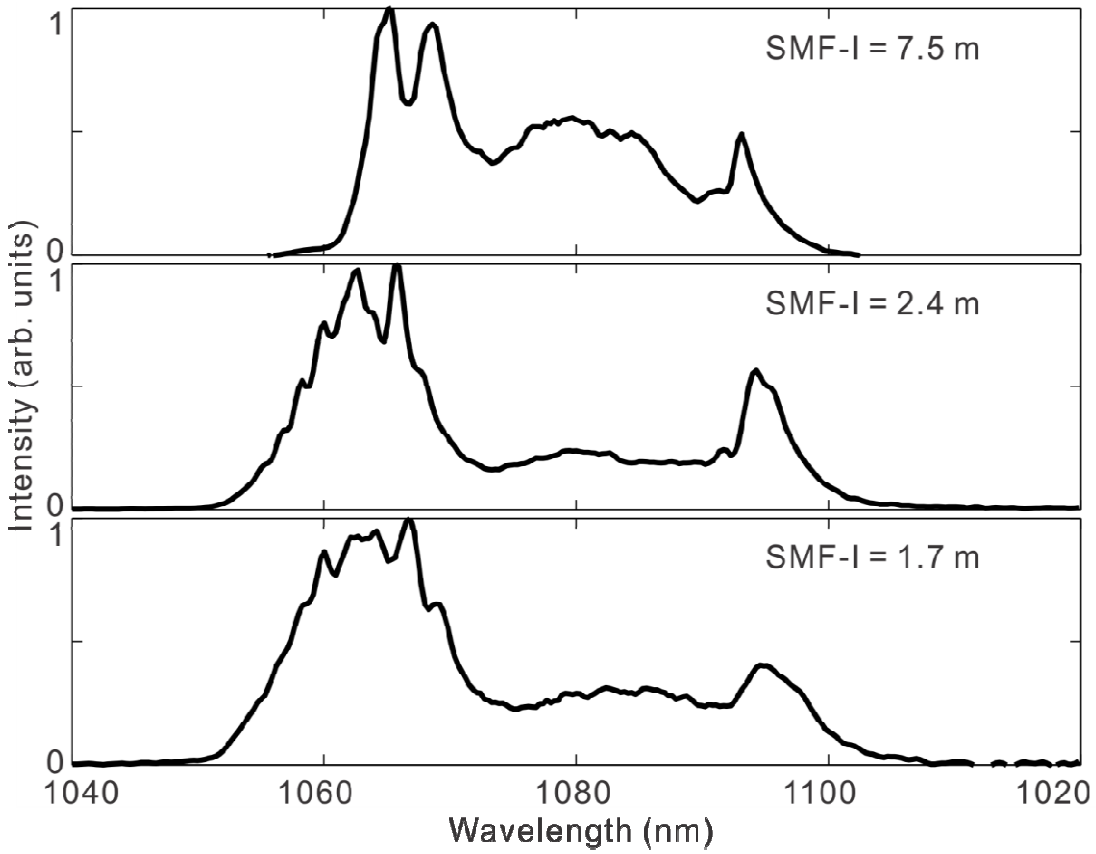

Figure 25: Output spectra of laser cavities using (top) 7.5 m, (middle) 2.4 m and (bottom) 1.7 m SMF-I.

In this laser, SMF-I is used to pre-chirp the pulse before being amplified in the gain fiber. Without pre-chirp, it will just behave like a soliton fiber laser and cannot tolerate the high pulse energy. The pre-chirp lowers the pulse peak power, which helps to avoid too much nonlinear phase accumulation during amplification. To be noted, as shown in Chapter 1, the nonlinear phase shift induced by SPM is associated with spectral broadening and a proper nonlinear phase shift is helpful. When SMF-I becomes very long, the laser pulses would be too chirped to accumulate enough nonlinear phase shift for spectral broadening. Also, SMF-I introduces nonlinear phase shift. The excess nonlinear phase shift can be detrimental to the laser performance. It is experimentally observed that, mode-locking becomes less stable with long SMF-I.

On the contrary, the lengthening of SMF-II broadens the output spectra. The opposite correspondence is due to the different roles of SMF-I and SMF-II in the cavity. SMF-II guides the light out of the gain fiber. Other than that, it also helps broaden the output laser spectra by taking advantage of SPM effects. Ideally, it would be good to use long SMF-II to broaden the laser spectra as much as possible, provided the entire bandwidth is coherent and compressible. However, as we mentioned in Chapter 1, unwanted wave-breaking could happen to prevent this expected pulse evolution. In order to prevent wave breaking, SMF-II length is limited to only about 0.3-0.5 m.

2.2.2.2 Filter bandwidth dependence

As mentioned before, the spectral filter bandwidth varies due to the thickness of the birefringent plate used. Three different spectral filters – 12 nm, 20 nm and 30 nm FWHM bandwidth are tested, while keeping other cavity parameters the same.

It is very hard to mode-lock the laser with a 30 nm spectral filter. The narrower the filter bandwidth, the easier the mode-locking becomes. This shows that spectral filtering does help stabilize mode-locking in all-normal dispersion fiber laser. A FWHM 30 nm bandwidth filter is too large to cause any pulse shaping of the pulses inside the cavity. When it is replaced with a 20 nm spectral filter, stable mode-locking is achieved. It is found that further reducing the filter bandwidth to 12 nm increases the output spectra bandwidth, as shown in Figure 26. The broadening of the output spectra is observed in both the 7.5 m long SMF-I and 2.4 m long SMF-I cavities. The shifted central frequency of the output spectra is due to different axis angles of the birefringent plates relative to the table axis, as mentioned early in this chapter.

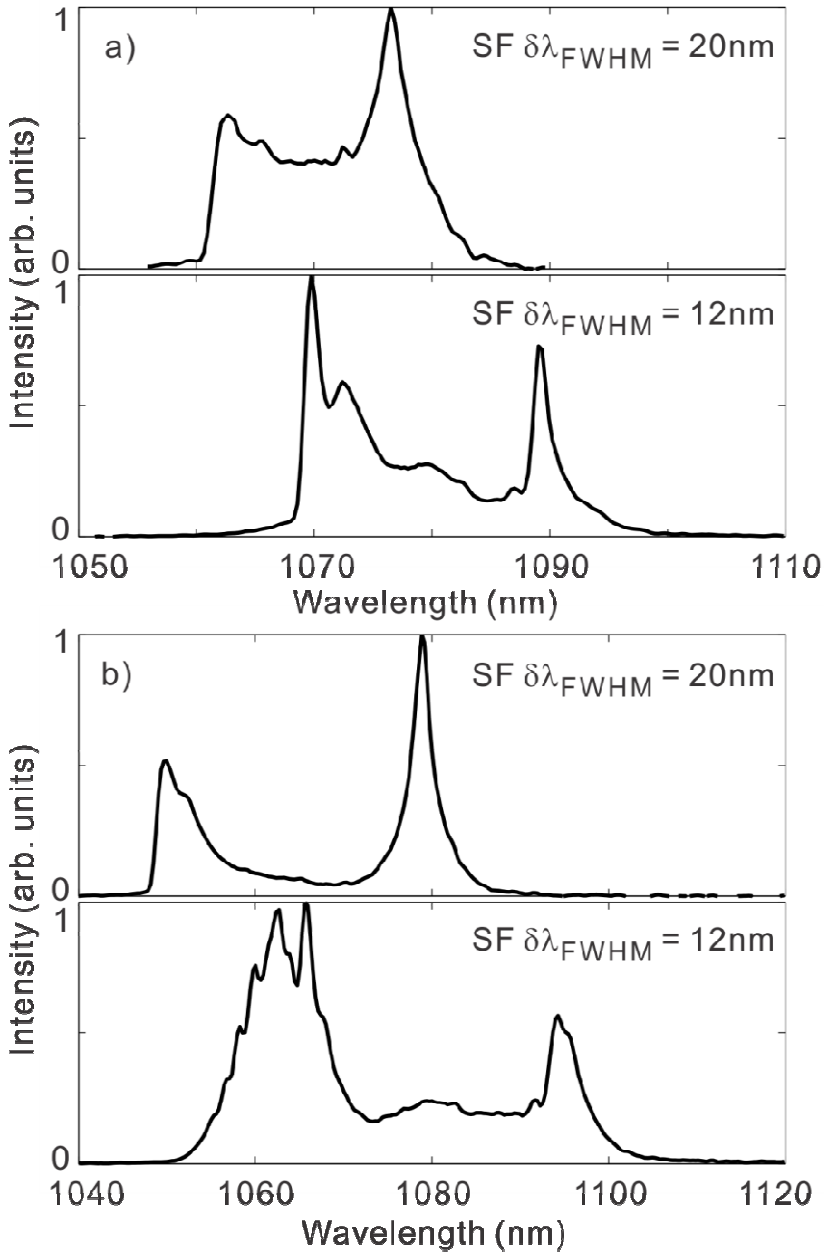

Figure 26: Dependence of the output spectra on the spectral-filter bandwidth (a) Cavity with 7.5 m SMF-I and a 20 nm (top) or a 12 nm (bottom) spectral filter; (b) Cavity with 2.5 m SMF-I and a 20 nm (top) or a 12 nm (bottom) spectral filter.

The spectral filter bandwidth dependent output spectra are observed in various laser cavities with different SMF-I length. Figure 26(a) and Figure 26(b) are the results from two cavities using 7.5 m and 2.4 m SMF-I, respectively. Both of them show the broadening of output

spectra due to narrower spectral filter, which results in shorter compressed pulses. However, it is more significant in the cavity with shorter SMF-I.

2.2.3 Conclusion

Based on the studies shown above, it was found that the output spectrum bandwidth is highly dependent on the length of SMF-I and the spectral filter bandwidth. Generally, the longer the SMF-I is, the narrower the output spectral bandwidth; the narrower the spectral filter bandwidth, the broader the output spectral bandwidth. Increase of SMF-II can also broaden the output spectrum to some extent, but it is not a good parameter to tune in this laser. Meanwhile, the stability of mode-locking is also influenced by these parameters.

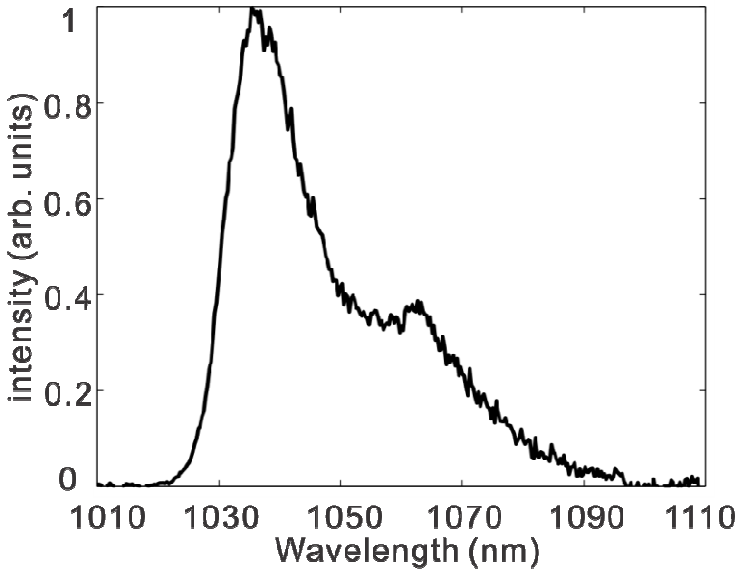

Figure 27: Amplified spontaneous emission of the gain fiber.

Our lasers mentioned above can routinely deliver pulses with tens of nJ pulse energy and as short as 80 fs pulse duration. Output pulses with 34 nJ pulse energy and 80 fs already beats the best all-normal dispersion fiber laser (31 nJ and 80 fs) reported previously [59]. However, it is hard to further push the pulse duration below 50 fs with this design. The output spectrum is not near the gain bandwidth limit (Figure 27), which means there is still room for improvement. The

interesting fiber bandwidth dependence made us wonder whether we can further reduce the spectral bandwidth to broaden the output spectrum though it sounds counter intuitive.

2.3 Similariton fiber lasers

In 2010, Bale et al. proposed that strong spectral filtering in a fiber laser can act as a nonlinear attractor to generate similariton pulses [60], which have a parabolic pulse profile. Later this regime was demonstrated experimentally and pulses with 55 fs FWHM pulse duration and 3 nJ energy per pulse were delivered from a similariton fiber laser with a very narrow spectral filter. [61]

2.3.1 Introduction to the similariton

The similariton in an optical fiber was first investigated theoretically by Anderson et al. [62]. In their work, they found a solution for which optical pulses can avoid wave-breaking and preserve their pulse shape when propagating in optical fibers. The solution is defined by [62]

$$A(x,\tau) = A_p\sqrt{1-\tau^2/\tau_0(x)^2}\,\exp(-ib\tau^2/2), \qquad (40)$$

Where $A(x,\tau)$ is the pulse field, τ is instantaneous time, x is the position in the fiber, A_P is the peak amplitude, τ_0 is the pulse duration, and b is the chirp parameter. In order to achieve this solution, assumptions of high pulse intensity, strong nonlinearity and normal dispersion were made [62]. The quadratic phase term, yielding a linear chirp, is the reason that optical pulses described by this solution can avoid wave-breaking.

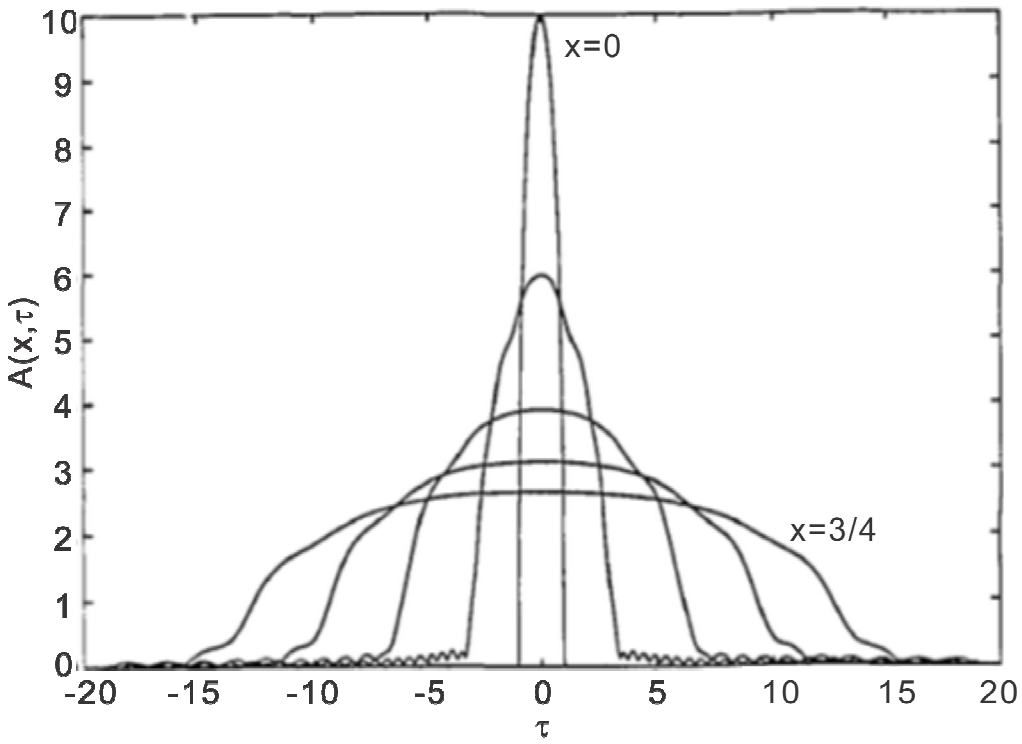

Figure 28: Numerical solution of the nonlinear Schrödinger equation for the pulse amplitude at different propagation distance. [62]

As seen from Equation (40), an optical pulse with this solution has a parabolic profile. The parabolic profile is preserved with increasing width of the pulse as it propagates in the fiber(see Figure 28) [62]. That is why this type of pulses is called ‘self-similar pulse’ or ‘similariton’.

Depending on the change of pulse intensity, they are categorized as passive similaritons, which propagate in passive fibers and dissipate in peak power and amplifier similaritons, which propagate in active fiber and gain peak power (see Figure 29) [44]. Since similaritons can tolerate greater pulse energy than solitons without wave-breaking, it would be useful to design a similariton fiber laser that delivers higher energy short pulses.

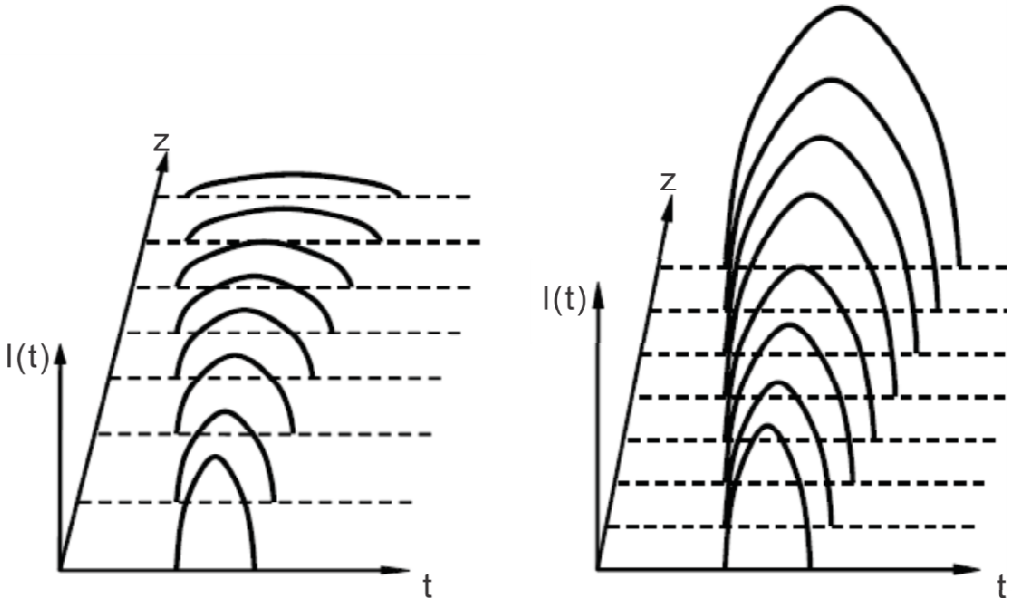

Figure 29: Similariton in passive (left) and gain (right) fiber [44]

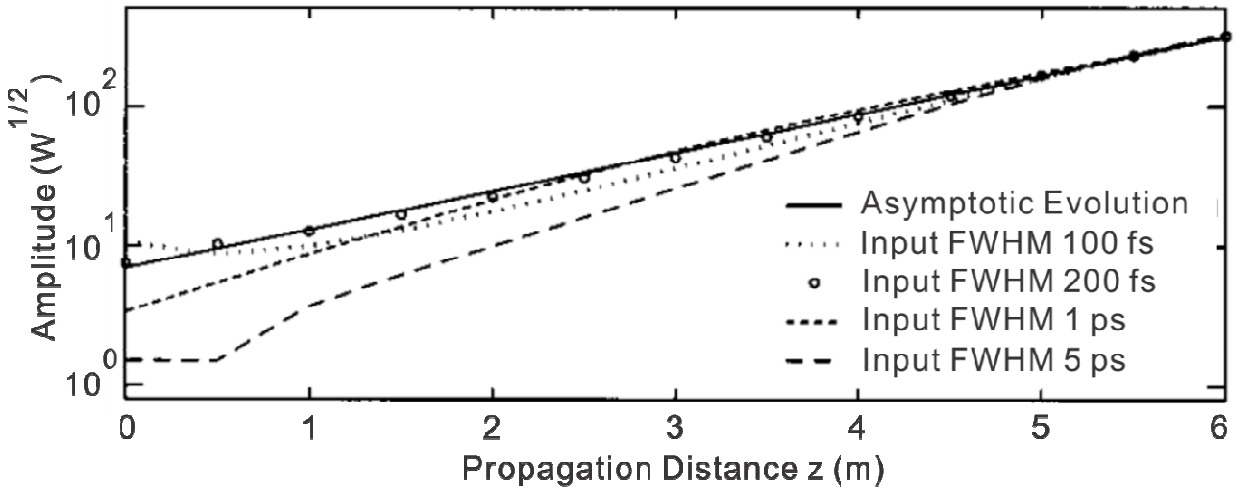

Figure 30: Evolution of pulse amplitude as functions of propagation distance in a normal-GVD fiber amplifier. [63]

Experimentally self-similar pulse evolution was first observed in a fiber amplifier [64], because the requirement for high pulse intensity can be easily achieved in a fiber amplifier. Based on the results in reference [64], the same group of researchers also theoretically studied the amplifier similariton [63]. They found that only the initial pulse energy mattered to determine whether the similariton would form in the gain fiber. As shown in Figure 30, the theoretical

predictions for the asymptotic parabolic pulse evolution (solid curve) were compared with the results obtained for simulations with input pulses of different pulse durations yet identical pulse energy. The pulse duration of the input pulses only determines how fast the input pulse is transformed into a self-similar pulse. The input pulse energy giving the fastest convergence to self-similar evolution is defined by [63]

$$U_{in} = \frac{2T_P^3(0)g^2}{27\gamma\beta_2}, \tag{41}$$

where U_{in} is the input pulse energy, $T_P(0)$ is the input pulse duration, g is the gain, γ is the Kerr-coefficient of the fiber, and β_2 is the GVD of the fiber.

However, similariton generation in a fiber oscillator is not as simple as that in a fiber amplifier. Self-similar pulse propagation in a passive fiber section of a dispersion-managed fiber oscillator was experimentally demonstrated first [65]. The passive similariton pulses stretch in time while their spectral bandwidth stays nearly constant. Recently, Oktem et al. [32], Renninger et al. [61], and Aguergaray et al. [66] have reported similariton formation in the amplifier sections of lasers. Amplifier similaritons undergo strong spectral and temporal breathing in the cavity. In the report of amplifier similariton formation in an all-normal-dispersion cavity [61], the authors focused on the new pulse evolution, not the performance limits. Amplifier similariton pulses having 3 nJ per pulse and compressed down to 55 fs were generated from an Yb fiber laser [61], but there was no attempt to maximize the pulse energy. The short pulses and smooth spectra of amplifier similariton lasers will be attractive for applications, so it is desirable to see if these solutions will be stable at higher energies.

2.3.2 Numerical Simulations

To verify the presence of amplifier similaritons in the cavity, numerical simulations based on the modified Ginzburg-Landau equation [67-69], with a gain term added to the nonlinear Schrödinger equation (8), are performed with the actual fiber parameters, using the split-step Fourier method [70]. The modified Ginzburg-Landau equation is given by [18]

$$\frac{\partial A}{\partial z} + i\frac{\beta_2}{2}\frac{\partial^2 A}{\partial t^2} - i\gamma|A|^2 A - \frac{g}{2}A = 0, \tag{42}$$

where group-velocity dispersion β_2 = 23 fs^2/mm and nonlinear coefficient γ = 0.0016 (W m)$^{-1}$ are used. The gain is defined by

$$g = \frac{g_0}{1 + \omega/\omega_0 + (\omega - \omega_0)^2 / \Delta\omega^2}, \tag{43}$$

where ω is the frequency, ω_0 is the pulse carrier frequency, $\Delta\omega$ is the gain bandwidth, and g_0 is called a small-signal gain, which means that the gain is small enough to avoid any gain saturation. In a fiber laser, the small-signal gain is normally limited by the parasitic lasing. g_0 can be calculated by $(30dB/10)\times\ln(10)/2 = 3.45$ in unit of m^{-1}. $30dB$ is the highest gain that should be used, since higher gain will generate significant spontaneous emission. An instantaneous saturable absorber is used for NPE. The saturable absorber function is given by

$$S(t) = 1 - \frac{m}{1 + P(t)/P_0}, \tag{44}$$

where m is the unsaturated loss, corresponding to the modulation depth, and P_0 is the saturation power.

This numerical simulation is based on a ring cavity design. The sequence of each component is the same as the experimental setup. The saturable absorber precedes the spectral filter. Starting from white noise, pulsing in the cavity is formed after a number of iterations.

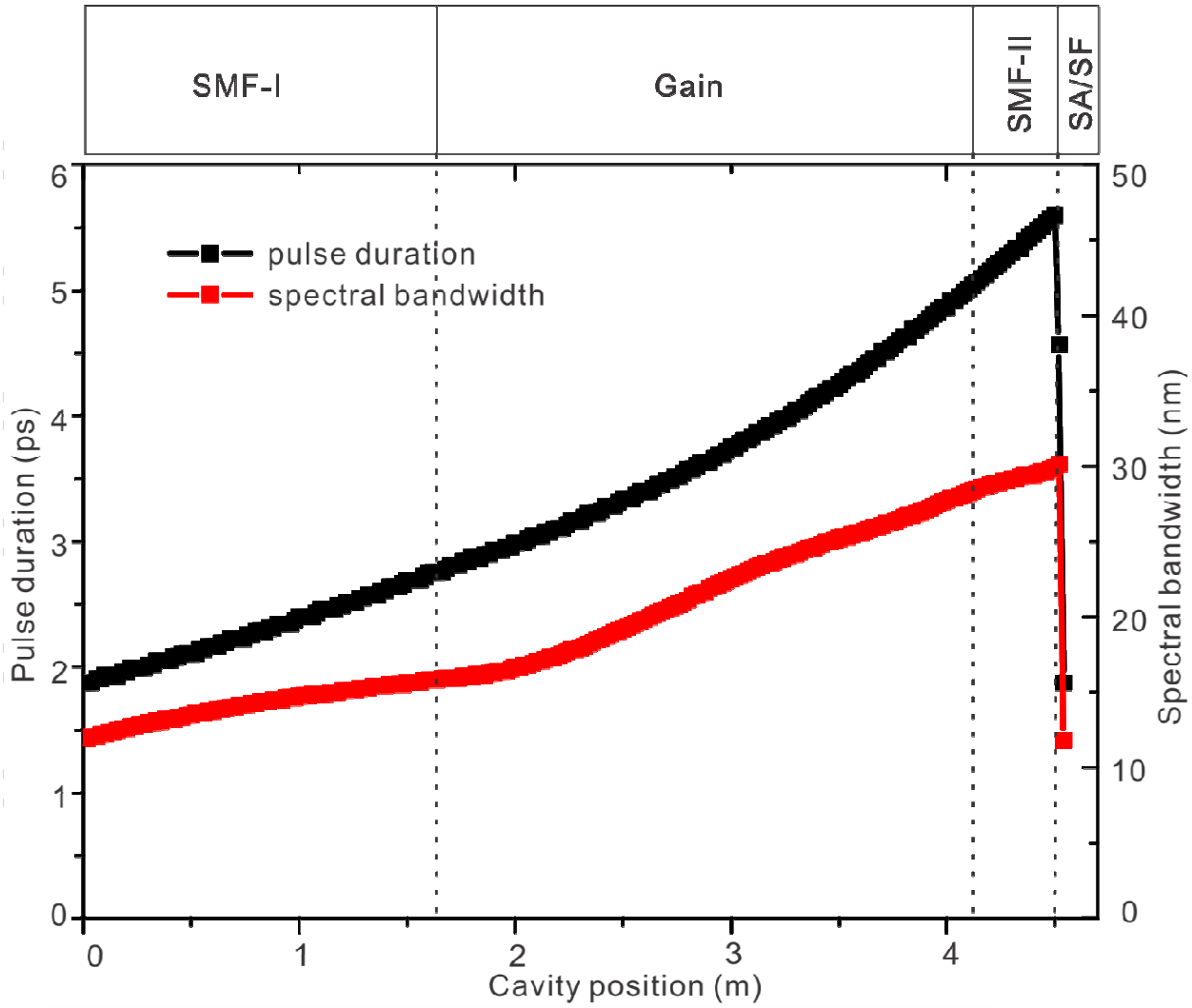

Figure 31: Top: scheme of cavity used for simulation. Bottom: pulse duration (black) and spectral bandwidth (red) evolution through the laser cavity with a 12 nm bandwidth spectral filter.

First, a laser cavity with a spectral filter of 12 nm bandwidth is simulated. The change of pulse duration and spectral bandwidth through the cavity is plotted in Figure 31. A parameter – the breathing ratio – is used to characterize the change, which is defined as the change of the pulse durations or spectral bandwidths. It can be seen that the breathing ratio of both pulse

duration and spectrum is about 2-3 through the entire cavity. To better illustrate the pulse evolution, a two-dimensional plot of spectral change is illustrated in Figure 32(a). The spectrum at the end of SMF-II is shown in Figure 32(b). The 'cat-ear'-like spectrum matches the experimental results very well. The match between the numerical simulation and the experimental results helps to validate our simulation model.

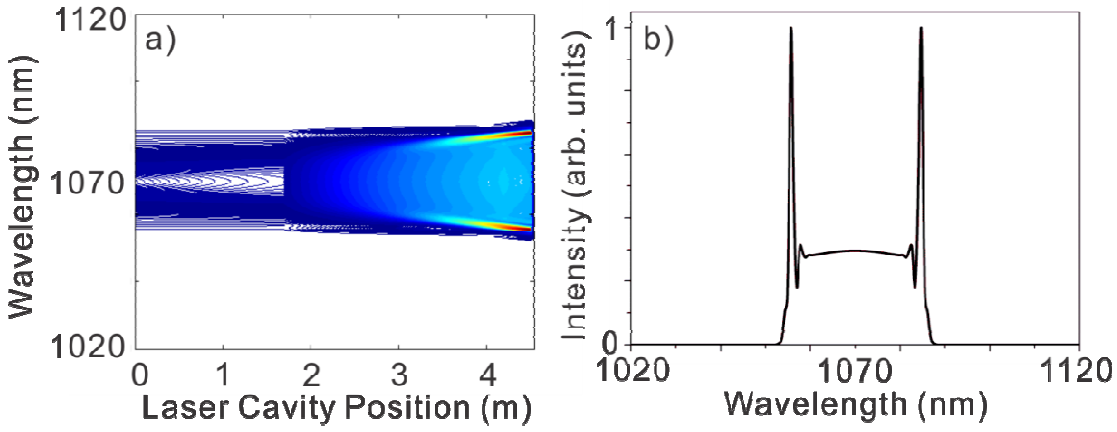

Figure 32: Simulation results of laser cavity using a 12 nm bandwidth spectral filter. (a) 2D spectral evolution through the cavity; (b) laser spectrum at the end of SMF-II

While keeping other fiber parameters the same, the bandwidth of the spectral filter is changed to 3 nm and the corresponding simulation results are shown in Figure 33 and Figure 34.

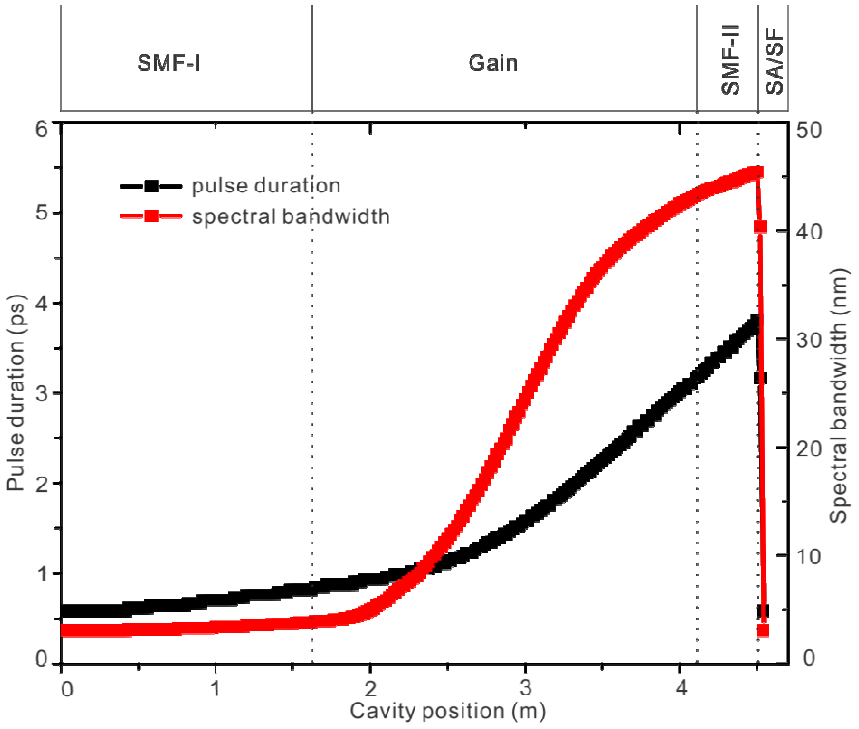

Figure 33: Pulse duration and spectral bandwidth evolution through the laser cavity with a 3 nm bandwidth spectral filter. Top: scheme of the cavity used for simulation.

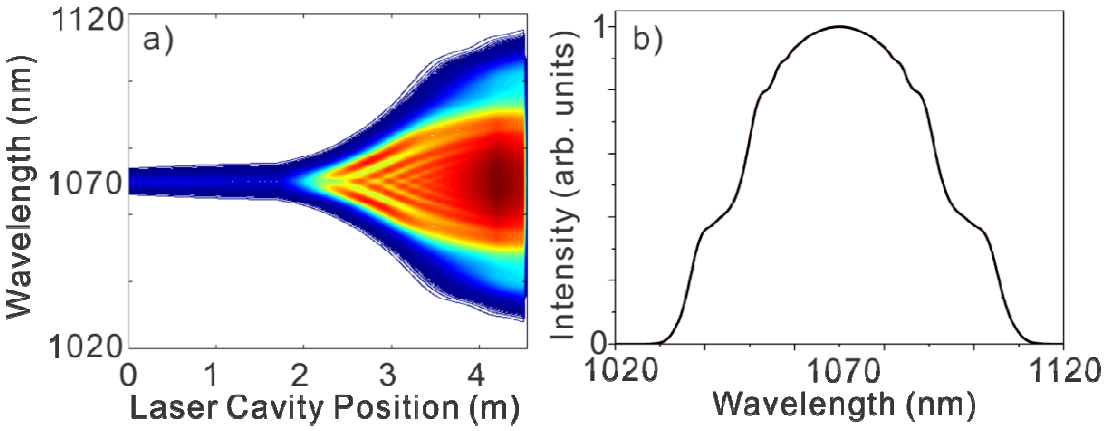

Figure 34: Simulation results of laser cavity using a 3 nm bandwidth spectral filter. (a) Two-dimensional spectral evolution through the cavity; (b) Laser spectrum at the end of SMF-II.

The pulses experience both large temporal and spectral breathing in the gain segment (Figure 33). The spectral breathing ratio is up to 15 throughout the cavity. The saturable absorber and spectral filter shape the pulse and make it self-consistent over the cavity round-trip. Note that the spectral filter does not only cuts the spectral bandwidth, but also reduces the pulse duration significantly. It shapes the pulse more than the saturable absorber and is the key component to attract pulse evolution to this special regime. The spectrum at the end of SMF-II (Figure 34(b)) is also very different from the 'cat-ear' shape and shows a parabolic profile, which is the characteristic of similariton pulses. The temporal pulse shape of the simulated results is also checked, as seen in Figure 35. Parabolic fit is applied to the pulse at the end of SMF-II and shows very good match, which further verifies the formation of similaritons.

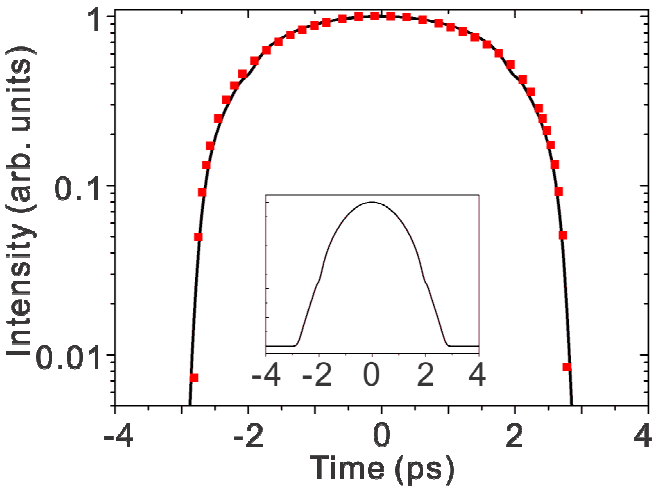

Figure 35: Simulated pulse shape of the pulse at the end of SMF-II plotted on a logarithmic scale. Red dots: parabolic fit; Insert: same plot on a linear scale.

2.3.3 Experimental setup of similariton fiber laser

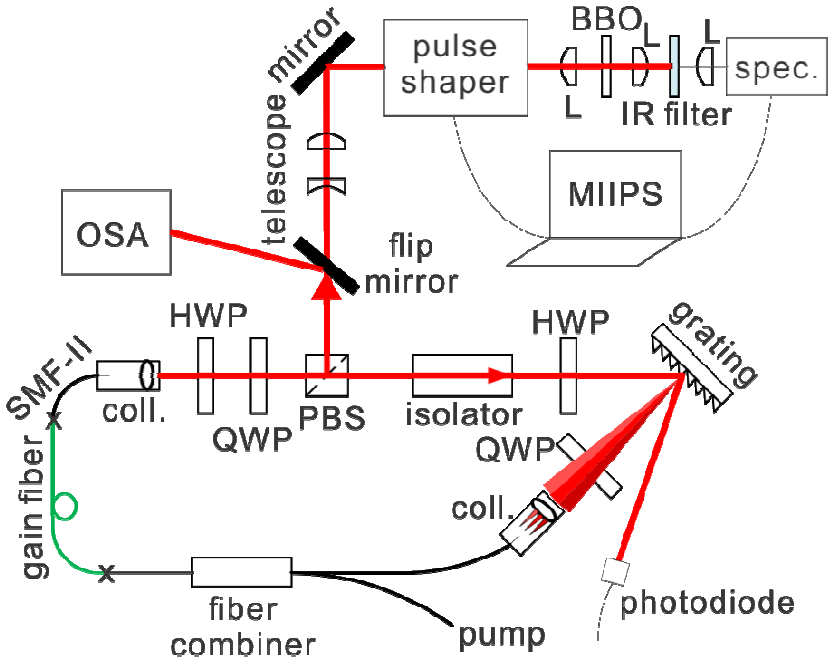

Figure 36: Schematic of the double-clad Yb all-normal-dispersion fiber laser cavity and the setup for pulse characterization. SMF-I and SMF-II: single mode passive fiber section I and II; QWP and HWP: quarter- and half-wave plates; PBS: polarizing beam splitter; coll.: collimator; OSA: optical spectrum analyzer; L: lens; spec.: spectrometer.

An all-normal-dispersion laser cavity is designed to support similariton formation in the gain medium. The narrow intra-cavity spectral filter is formed by the combination of a grating and a collimator [61], as shown in Figure 36. The collimator is set at a distance away from the grating (300 groves per millimeter) and is aligned to couple the 1st order diffraction beam from the grating back into the laser cavity. The small aperture of the collimator acts as a spatial and spectral filter. Also due to the 10 μm diameter core size of the fiber mounted in the collimator, only a very small amount of the 1st order beam couples into the rest of the cavity, as illustrated in Figure 36. Following the collimator is the single mode passive fiber (SMF-I) including the extension fiber of the collimator and combiner. A short section of single mode passive fiber (SMF-II) follows the gain fiber. The 10 μm core diameter Yb doped double-clad gain fiber

(CorActive DCF-YB-10/128) is spliced to SMF-I and SMF-II, respectively. The gain fiber is pumped by a CW diode laser at 976 nm. A PBS, isolator, and several wave plates (HWP and QWP on the left side, and QWP on the right side in Figure 36) act as an artificial saturable absorber based on NPE [50]. By adjusting these wave plates, passive mode-locking can be achieved. The HWP preceding the grating helps to maximize the efficiency of the 1^{st} order diffraction. The 0^{th} order diffraction beam is directed onto a photodiode, connected to an oscilloscope or a radio frequency (RF) spectrum analyzer.

The PBS acts as the output coupler. The output spectrum is measured by an Optical Spectrum Analyzer (OSA, HP70451). A flip mirror near the output is used to direct the beam into the MIIPS-enabled pulse shaper (MIIPS Box 640, Biophotonic Solutions Inc.). Before entering the shaper, the beam is expanded by a 3x telescope. The output of the pulse shaper is focused on a 10 μm BBO crystal (see Figure 36). The resulting SHG signal is detected by a fiber-coupled spectrometer (Ocean Optics, USB4000). The MIIPS program measures the spectral phase of the pulses at the nonlinear crystal and adaptively compensates high order dispersion to obtain transform-limited pulses. A number of tests and shaper-assisted interferometric autocorrelation (AC) are performed to ensure that the results are consistent with independent theoretical calculations.

2.3.4 Experimental results

As learned from previous experimental tests, simulation results and other researchers' reports [61], the length of each fiber segment affects the similariton laser similarly as in a common all-normal dispersion fiber laser. Here, the fiber length of SMF-I and SMF-II is chosen to be 1.7 m and 0.35 m, respectively. These parameters were found to be good in both previous

laser design and numerical simulations. The fiber collimator is placed about 13 cm away from the grating and acts as a ~3 nm spectral filter.

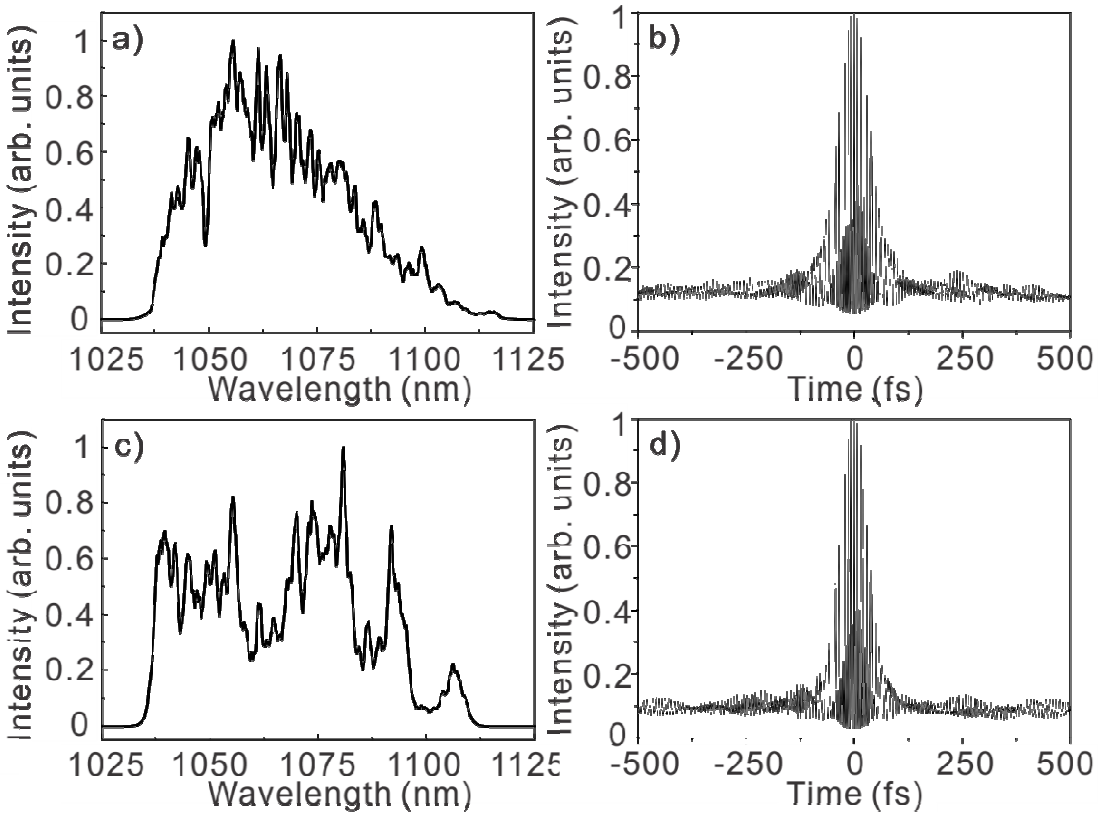

Figure 37: Two output modes with the same pump power. (a) and (c) Output spectrum; (b) and (d) Interferometric autocorrelation. Note: the gray or dark color in (b) and (d) has no meaning. It is caused by the varying density of lines.

Various mode-locked states are possible depending on the diode laser pump power and the orientation of the wave plates. With the pump power at 3.1 W, two different output modes are shown in Figure 37. The fringes on the spectra are due to the interference in the multi-mode fiber used for OSA measurement. The deviation of spectra from parabolic shape is caused by the NPE induced frequency dependent transmission through PBS. By inserting a beam sampler before the PBS, a parabolic spectrum can be observed. The measured AC FWHM is ~80 fs and the calculated deconvolution factor is 1.39, which gives the FWHM pulse duration as 57 fs (Figure

37(b) and (d)). By increasing the pump power, not only the output power but also the output spectral bandwidth increases.

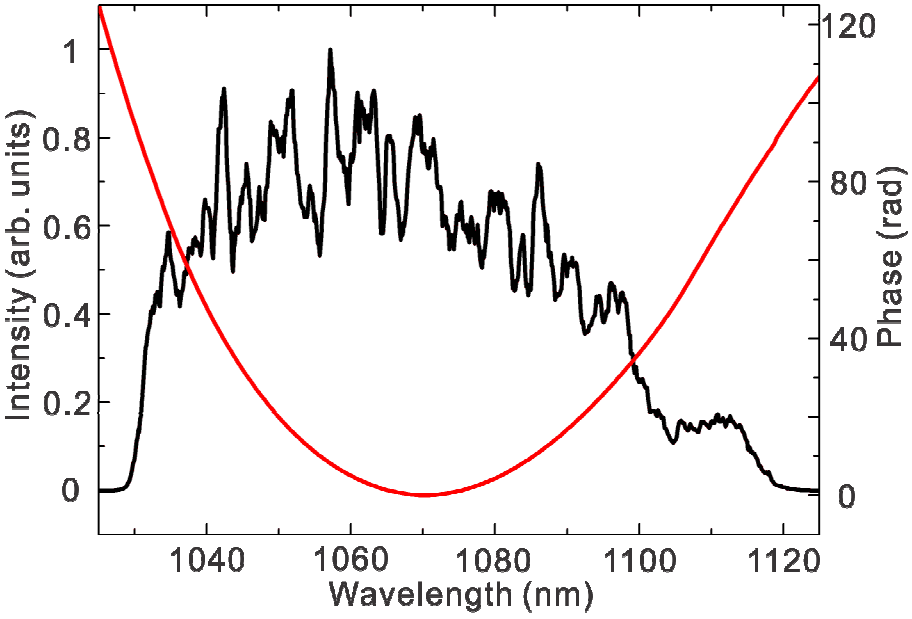

Figure 38: Output laser spectrum (black) and measured spectral phase of the output pulses (red).

When being pumped at 4.1 W, a stable mode-locked state with an average output power of 930 mW is obtained (Figure 38), corresponding to 21.9 nJ pulses emitted at 42.5 MHz rep. rate (Figure 39(a)). The output pulse train is monitored by a fast photodiode on the oscilloscope. There are power fluctuations observed from the pulse train, which are probably due to the unfixed fibers in the cavity. To better check the stability of mode-locking, a RF spectrum analyzer is used to analyze the pulse train. With a 1 MHz frequency span, the RF spectrum analyzer gives a single peak at 42.48 MHz with ~70 dB signal-to-background ratio (Figure 39(b)). No sidebands are observed for the fundamental and higher harmonics over the 500 MHz span [Figure 39(c)], which confirms the stable mode-locking.

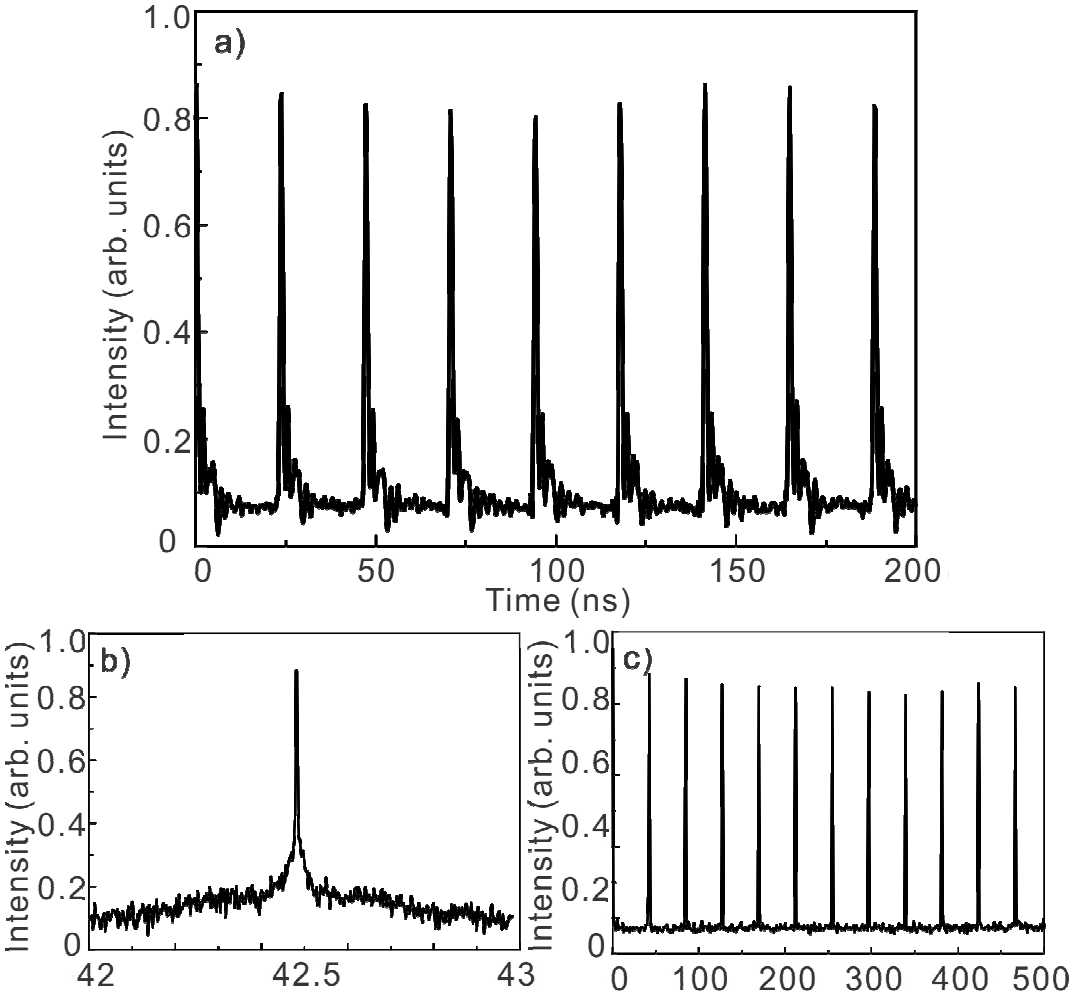

Figure 39: Laser performance. (a) pulse train form oscilloscope. Repetition rate 42.5 MHz; (b) RF spectrum analyzer result, 1 MHz frequency span; (C) RF spectrum analyzer result, 500 MHz span.

Output pulses are compressed and characterized using a MIIPS-enabled pulse shaper. The MIIPS software scans a sinusoidal spectral phase function across the spectrum of the pulses, collects the resulting SHG spectra and derives the corresponding spectral phase distortion [53, 54, 71]. Typically, seven iterations are run for the measurements presented here in order to obtain compensation within 99.7% of the theoretical transform limit, defined by the input laser spectrum. The phase function required to achieve transform limited pulses is the complementary phase obtained after double integration of the shaper-measured second-derivative. To account for phase distortions due to optics in the pulse shaper and thereby measure the pulse phase directly at

the laser output, we have independently measured the phase distortions due to the pulse shaper itself by putting it in line with another pulse shaper. The measured phase at the laser output pulses is shown in Figure 38. Polynomial fitting up to the third order gives ~35,000 fs^2 of second-order dispersion (SOD) and ~166,000 fs^3 of third-order dispersion (TOD). Note that the observed SOD is much less than the cavity dispersion of ~100,000 fs^2, calculated based on the total fiber length and the fiber group-velocity dispersion β_2 = 23 fs^2/mm. This is one of the characteristic signatures of similariton formation in a gain medium [61].

After pulse compression, the pulse shaper has been used to create two pulse replica and scan one of them in time to obtain interferometric autocorrelations [72], resulting in an AC trace with full-width-half-maximum (FWHM) of 57 fs. Based on Fourier transformation of the experimental laser spectrum and autocorrelation simulations, a deconvolution factor of 1.37 is used to calculate the FWHM pulse duration, which is 41.6 fs for the compressed pulses. The measurements show excellent agreement with calculations (Figure 40(c)). Similarly, we have also compared the experimental SHG spectrum for compressed laser pulses with the calculated SHG spectrum based on the measured fundamental spectrum of the laser and a flat spectral phase (Figure 40(a)). Excellent agreement between theoretical and experimental results for both linear and logarithmic scales gives us confidence in the measured parameters and that the laser pulses at the BBO crystal are transform limited.

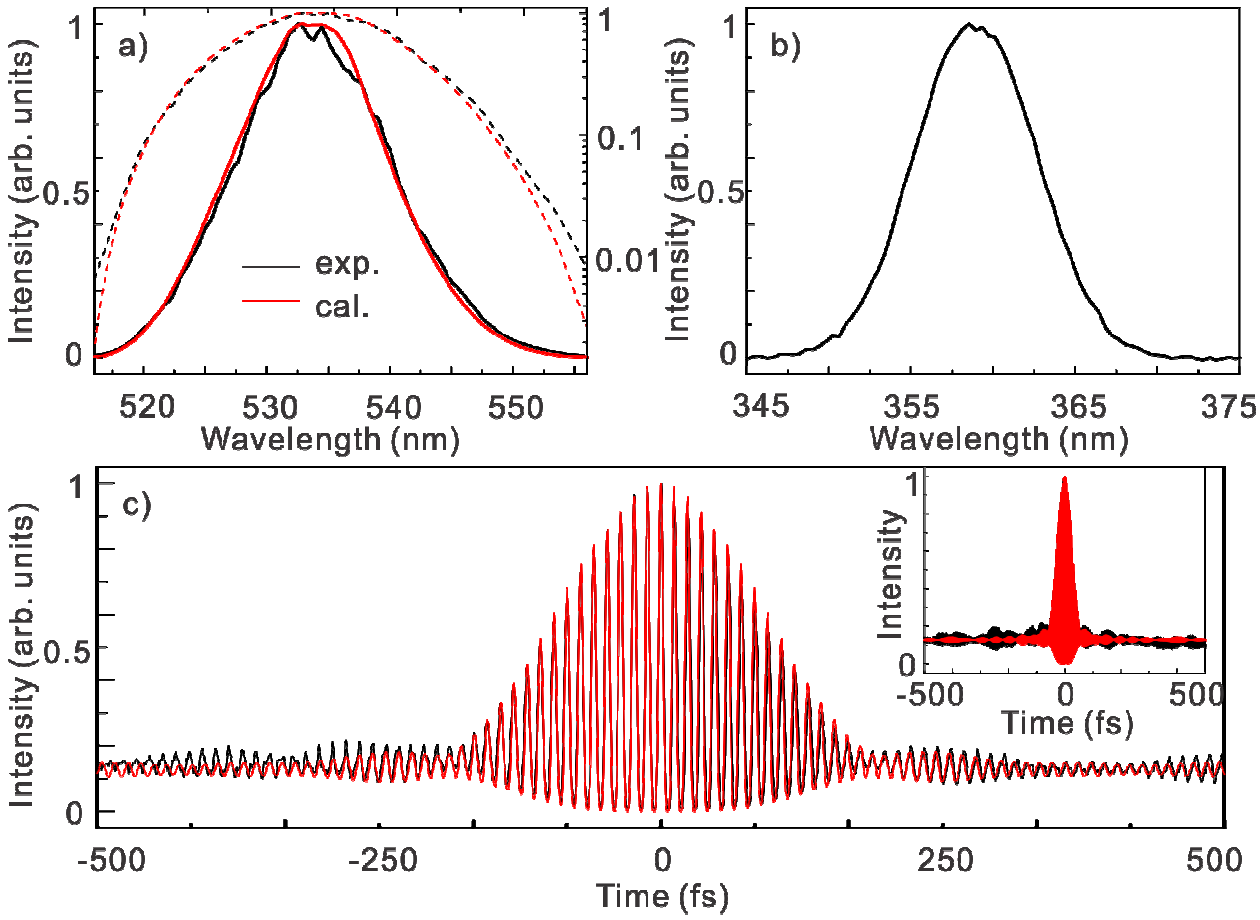

Figure 40: (a) Experimental and calculated SHG spectra shown in linear (solid curve) and log-10 (dashed curve) scales. (b) Experimental THG spectrum obtained by focusing TL pulses at the surface of a glass slide. (c) Experimental and calculated interferometric autocorrelation traces for compressed laser pulses in the range of -150 fs to 150 fs. Insert: Same data in the range of -500 fs to 500 fs.

Taking into account the throughput of our pulse shaper (~50% due to the reflection efficiency of the grating and mirrors), we calculate the peak power for compressed pulses to be about 250 kW. This peak power is sufficient to obtain THG at the interface of air and glass [73], see Figure 40(b). For these measurements, the output from the pulse shaper is first focused via a 10x objective on a BBO crystal. Then, the pulses are compressed at the objective focus. Once pulse compression is achieved, the BBO crystal is replaced by a 1-mm-thick glass slide. The

broad THG spectrum indicates that the third order dispersion is fully corrected. Higher peak power can be obtained by improving the throughput efficiency of the pulse shaper.

We have also observed that for a fixed filter bandwidth, the spectral breathing ratio through the cavity is proportional to the pump power. However, when the pump power is increased over 4.1 W, the output laser spectrum continues to broaden but is no longer stable and fully coherent. Only partial pulse compression has been achieved and the resulting SHG signal is observed to be much weaker than when the output is fully coherent.

The filter bandwidth certainly affects the laser performance. When the collimator is moved closer to the grating (~11 cm in between) and the spectral filter bandwidth is increased to ~4 nm, compressed pulses as short as 52 fs are obtained. Further reducing the filter bandwidth is also tested and no obvious improvement has been observed. The numerical simulations also predict that, it is difficult to achieve stable mode-locking when the filter bandwidth is smaller than 3 nm. According to numerical simulations, the transition from dissipative soliton to amplifier-similariton happens when the filter bandwidth is reduced below ~6 nm. The simulation results are in agreement with experimental results for several filter bandwidth conditions.

Energy loss material is also inserted into the cavity on purpose to increase the coupling loss in between two collimators; losses increase the threshold pump power but do not improve the breathing ratio.

2.3.5 Discussion

The significant change of pulse evolution due to the spectral bandwidth can be understood by the theoretical study of similaritons in fiber amplifiers. It was learned that only the pulse energy of input pulses determines whether a similariton forms in a fiber amplifier. The input pulse energy U_{in} giving the fastest convergence to similariton is defined by Equation (41). Here,

$\gamma = 0.0016(mW)^{-1}$, $\beta_2 = 23\times10^3\ fs^2/m$ and $g = 2m^{-1}$ are used for calculation. According to the simulation results in Figure 31 and Figure 33, the FWHM pulse duration of the pulses reaching the gain fiber input is about 2.8 ps for the laser using 12nm bandwidth spectral filer; and 0.8 ps for the one using 3 nm spectral filter. According to Equation (41), the calculated critical input pulse energy U_{in} is about 177 nJ and 4 nJ for lasers with 12 nm and 3 nm spectral filters, respectively. Even considering the loss caused by filters, the 12-nm-filter laser still requires 10 times higher intra-cavity pulse energy to form similaritons in the same pace as the 3-nm-filter laser. In the case that the output pulse energy of the 12-nm-filter laser is 35 nJ, the non-ejected intra-cavity pulse energy can be estimated to be about 70 nJ. Considering the ratio between the spectral filter bandwidth and output spectral bandwidth of 30 nm, the input energy for the gain fiber is about 28 nJ, which is too small compared to the critical value of 177 nJ. This is not considering the 'cat-ear' like spectra profile, which should experience even higher loss caused by the spectral filter. Hence, it will be impossible to generate similaritons in the laser cavity with 12 nm or larger bandwidth spectral filter. For the 3-nm-filter laser, in the case of an output pulse energy of about 20 nJ, the residual intra-cavity pulse energy is estimated to be 40 nJ and the output spectral bandwidth 45 nm, considering a linear loss due to the spectral filter. Then the input pulse energy to the gain fiber is about 2.7 nJ, which is close to the expected value. Since the similariton pulse has a parabolic spectrum and the 3 nm spectral filter is applied around the peak intensity, it should cause a less than 1/15 loss and result in better transmission. Considering the error in the estimation, this gives us a basic idea about how the pulse evolution is affected by the change of intra-cavity spectral bandwidth. Therefore, the narrow intra-cavity spectral filter provides a good combination of pulse energy and pulse duration for fast convergence to similariton in gain fiber.

The other reason that all the efforts have failed to increase the breathing ratio is due to the gain bandwidth limit, as shown in Figure 27. When the laser spectrum reaches the gain bandwidth limit, the gain fiber itself acts as a filter to stop the spectral broadening.

The only way of increasing the output spectral bandwidth beyond the gain limit is to continue the self-similar evolution in a long SMF-II. It seems very practical since a similariton can avoid wave-breaking while propagating in normal dispersion fiber. However, this idea does not work for standard fibers, due to the high pulse intensity and strong nonlinearity requirements of the similariton solution. A standard normal dispersion fiber does not have a very large nonlinear coefficient. Without high pulse peak power, the corresponding nonlinearity will be fairly weak. Meanwhile, the pulse intensity gets lower as it propagates in this fiber, which further weakens the nonlinearity. In this case, the similariton cannot be sustained and wave-breaking will happen again. This is verified by our experiments.

In one of our similariton fiber lasers, which uses single-clad 6 μm core diameter fiber, about 2 m long SMF-II is used. One of the output spectra is shown in Figure 41(a), which has typical structures of wave-breaking pulses as shown in Chapter 1 Figure 7. Pulse characterization using a pulse shaper shows the existence of wave-breaking. Output pulses are compressed with a MIIPS-enabled pulse shaper and the SHG spectra of compressed pulses match very well with the calculation based on the fundamental spectrum; see Figure 41 (b). In Figure 42, both interferometric AC and background-free intensity AC are measured and compared to the calculations. They also show good match with small deviation on the side-lobes of the trace. Based only on these measurements, it is hard to tell whether this pulse is indeed wave-breaking or not. For further verification, MIIPS traces with sinusoidal phase scan and second order dispersion scan are investigated.

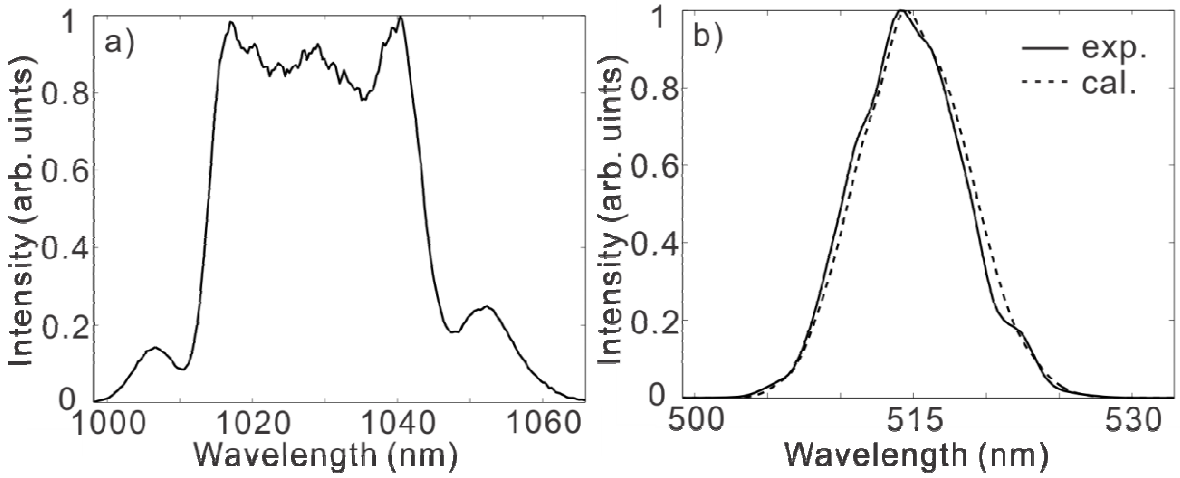

Figure 41: (a) Output spectrum of a similariton fiber laser using more than 1 m long SMF-II; (b) Comparison of experimental (solid line) and calculated (dash line) SHG spectra.

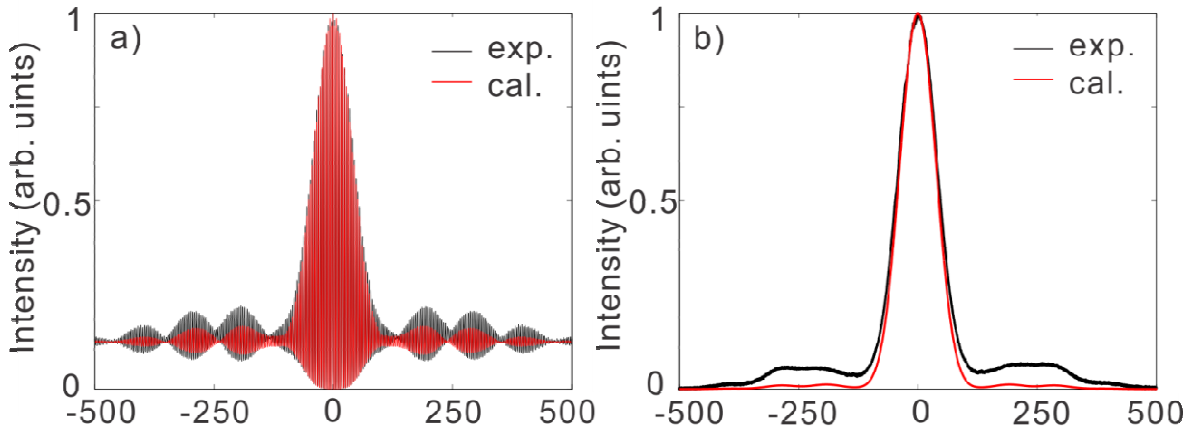

Figure 42: Calculated (red) and experimental (black) (a) interferometric and (b) background-free intensity autocorrelation traces.

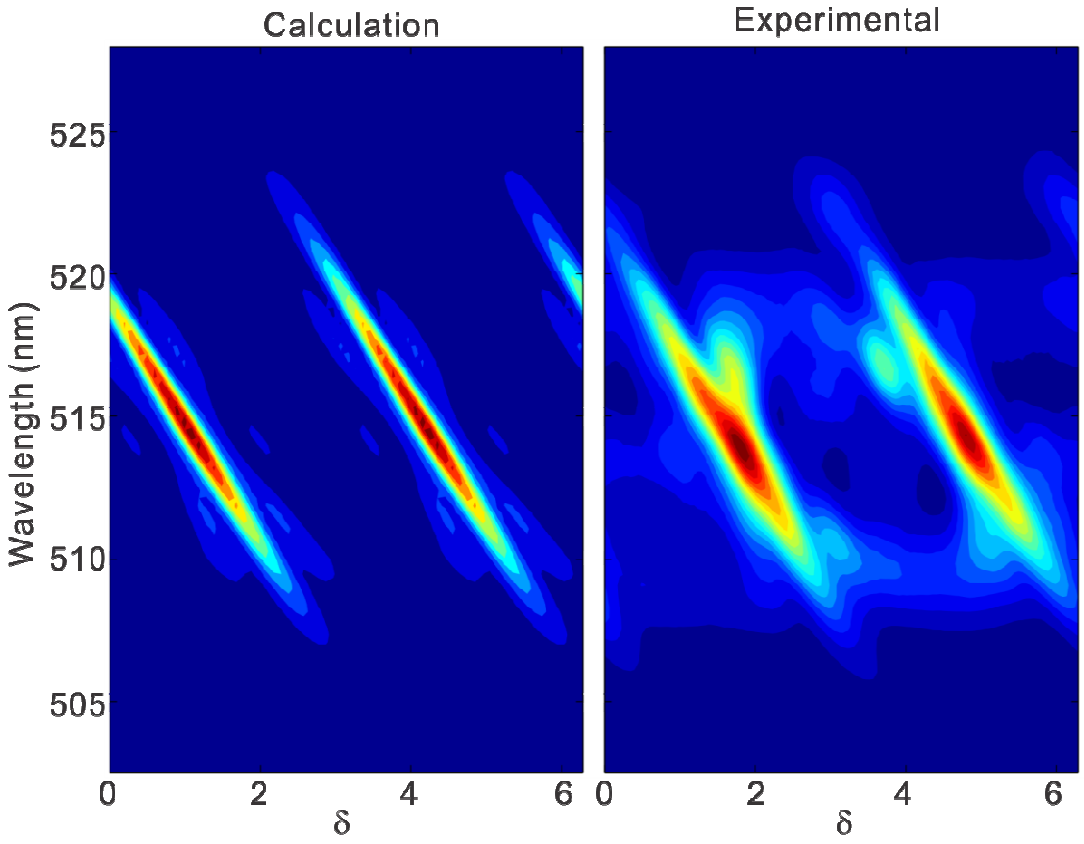

Figure 43: Calculated (left) and experimental (right) sinusoidal phase scan traces. δ is the scan parameter.

The experimental and calculated sinusoidal scan traces of compressed pulses are shown in Figure 43. Some bi-fork structures are observed on the experimental data, which are missing in the calculated result. This indicates the existence of multiple pulses that have different phase responses and generate local maxima in the SHG signal with different reference phase. Since MIIPS traces the maxima of the SHG signal and the main pulse dominates the generation of SHG, the phase distortion of the main pulse is fully corrected and the sinusoidal scan gives a trace of straight lines. Meanwhile phase distortion of minor breaking pulse is still left uncorrected and causes the bi-fork structures. Based on the shape of the trace, it is estimated that there is fourth order dispersion left in the minor breaking pulses, which is further proved with the second order dispersion scan.

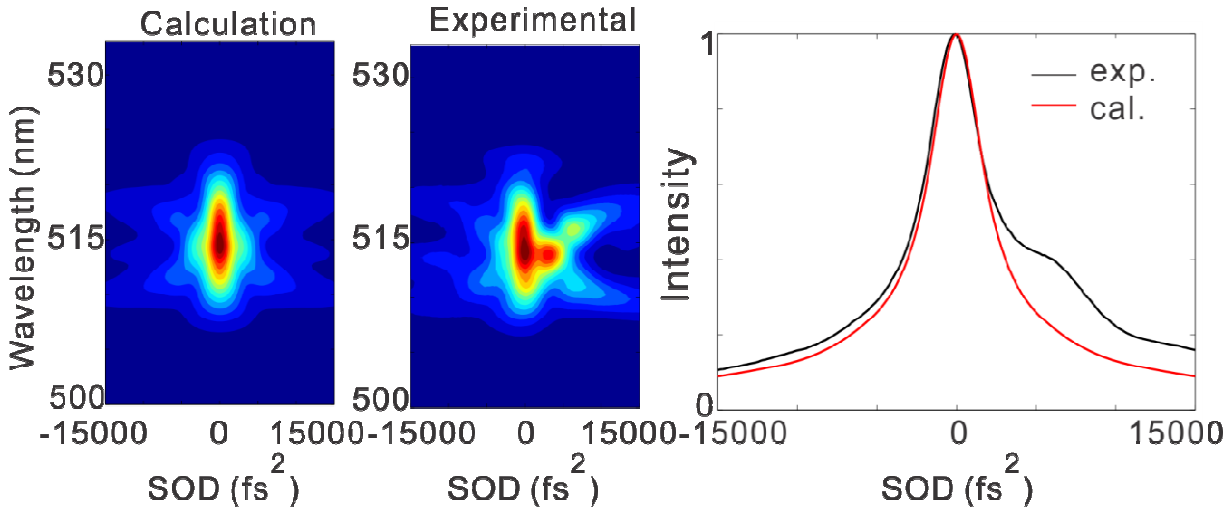

Figure 44: Left: calculated and experimentally measured two-dimensional SOD scan; Right: experimental (black) and calculated (red) SHG-integrated SOD scan.

Both the two-dimensional and SHG-integrated SOD scans (also referred to as chirp-MIIPS [74]) of compressed pulses are shown in Figure 44. On the simulated 2D trace, the SHG signal quickly dissipates after the appearance of the maxima and the trace is symmetric with respective to the scanned reference SOD. The experimentally measured 2D trace is very asymmetric, with the left half matching the simulation very well. On the right half, there is still a significant SHG signal observed when the reference SOD is about 5,000 fs^2, which is very different from the simulated trace. The deviation from the simulation results shows a parabolic-like profile that corresponds to fourth-order dispersion, as shown in Chapter 1 Figure 16. Meanwhile, the integrated SHG signal obtained by scanning of the second-order dispersion is also shown in Figure 44. An obvious deviation after ~2,500 fs^2 is observed. These observed deviations are due to the uncompressed phase distortion in the breaking pulses. These extra scan results provide full information of the pulses, not only the existence of wave-breaking pulses but also the different phase distortions for each part of the pulses.

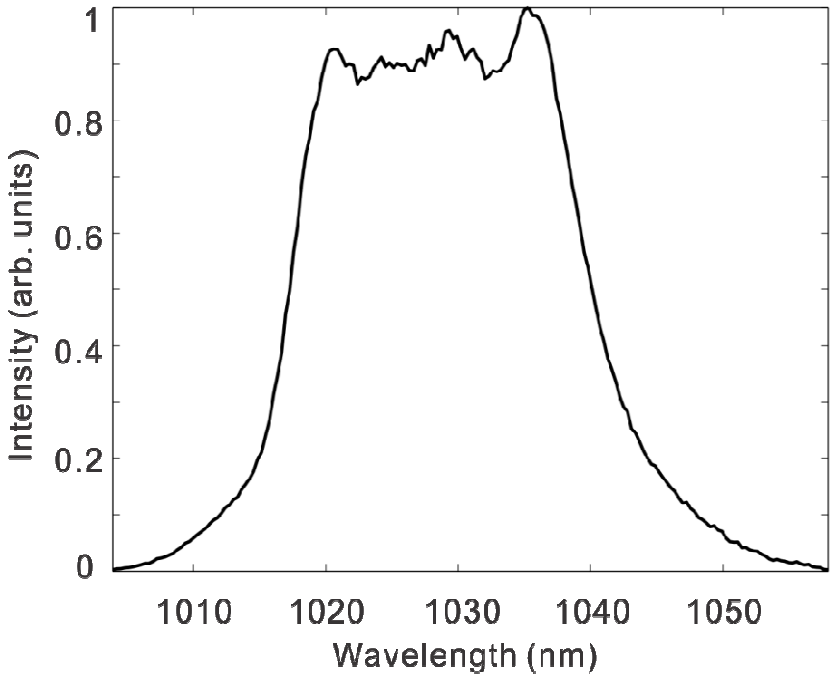

Figure 45: Output spectrum of a similariton fiber laser using more than 1 m long SMF-II with lower pump power.

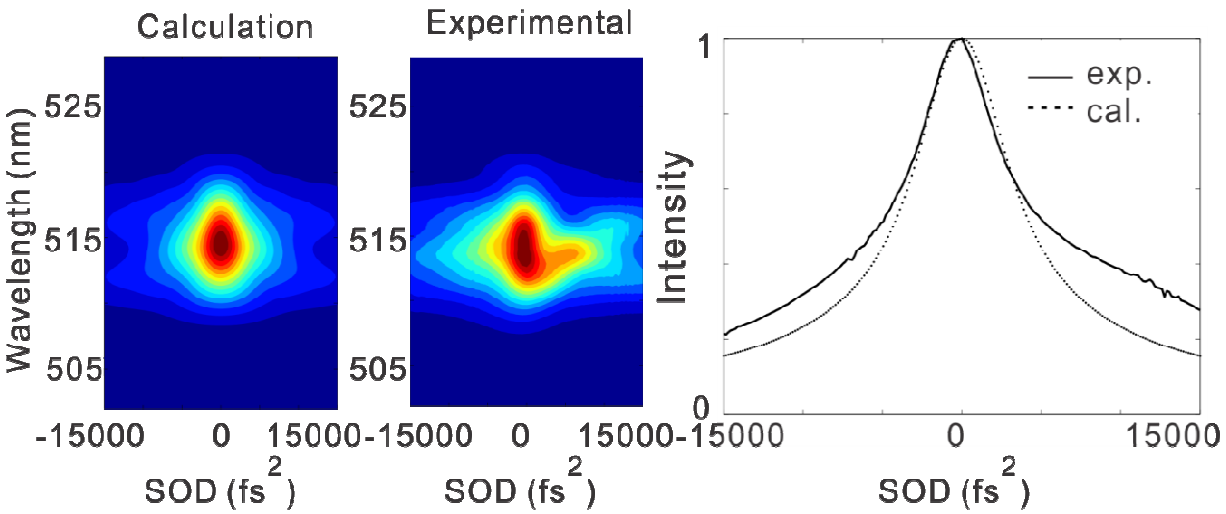

Figure 46: Left: calculated and experimentally measured two-dimensional SOD scan; Right: experimental (solid line) and calculated (dash line) integrated SOD scan.

These pulse characterization methods are very important. This is because normal pulse characterization approaches, such as autocorrelations, do not provide such detailed information which may mislead researchers, especially for the spectra that do not show typical signatures of

wave-breaking. As seen in Figure 45, the side-lobes on the spectrum disappear by lowering the pump power. However, wave-breaking still exists, as proved by the SOD scans (see Figure 46). Since there is quite a lot of energy wasted and phase distortion in the breaking pulses, it is very important to learn about and avoid wave-breaking.

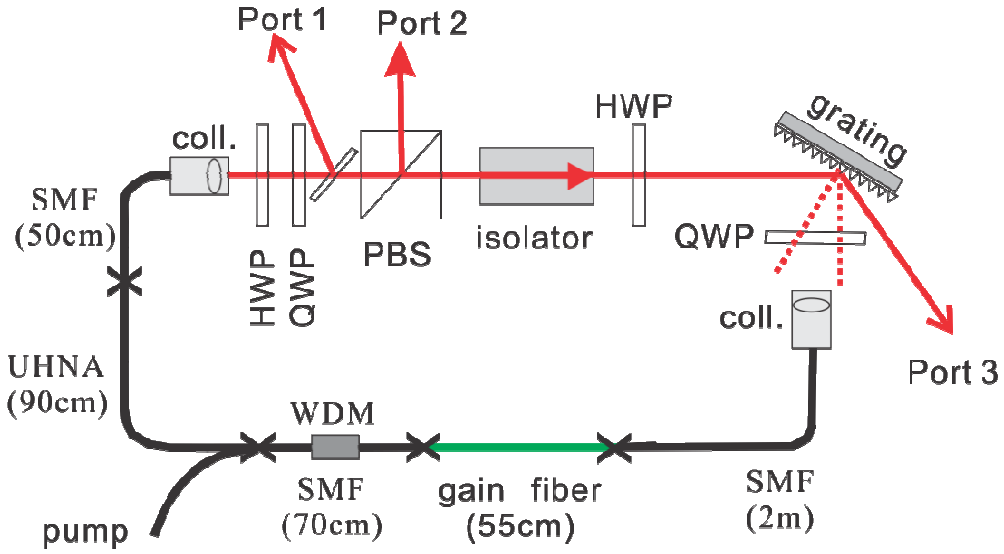

Figure 47: Experimental setup of the similariton fiber laser using the UHNA fiber. UHNA: ultra-high numerical aperture fiber; SMF: single mode fiber; HWP and QWP: half- and quarter-wave plate; coll.: collimator; PBS: polarizing beam splitter; WDM: wavelength division multiplexer.

As mentioned previously, strong nonlinearity is one of the requirements for the validation of the similariton solution. It is possible to use a passive highly nonlinear fiber to extend the self-similar evolution [75]. While keeping other cavity parameters the same as the wave-breaking fiber laser, part of the SMF-II is replaced with an ultra-high numerical aperture (UHNA) fiber (see Figure 47). UHNA fiber's core has a higher GeO_2 dopant than that of normal fiber, which results in a high NA and reduces the effective core diameter to only about 2.5 μm. So the nonlinear coefficient is also about 6 times higher than normal fibers. It also has larger dispersion (~50fs^2/mm) than normal fiber (~23fs^2/mm) due to the high concentration of GeO_2. However, the high nonlinearity still makes the self-similar evolution available. The experimental spectra

are shown in Figure 48. Spectra form ports 1, 2 and 3 are all measured. The output spectrum from port 2, before PBS, clearly shows parabolic profile. Also compared to Figure 41(a), the output spectrum is much broader. Further systematic study of this laser system and pulse characterization is still under investigation.

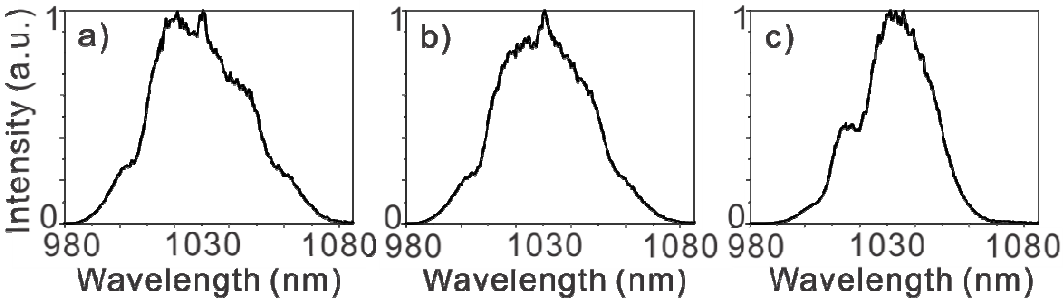

Figure 48: Experimental spectra from (a) port 1; (b) port 2; (c) port 3.

Besides UHNA fiber, photonic crystal fiber can also have a very small effective core diameter due to its microstructure. The experimental work done by Chong et al. has demonstrated that, FHWM 21 fs pulses with a pulse energy of ~ 1 nJ can be generated from a similariton laser using a long photonic crystal fiber (PCF) (see Figure 49 and Figure 50) [75]. The PCF used has an effective core diameter of 2 μm, resulting in about ten times higher nonlinearity than standard fiber. Though the similariton evolution greatly extended after the gain fiber, signs of wave-breaking pulses – side-lobes in spectrum – are observed in Figure 50 (a). So the passive highly nonlinear fiber is not an ultimate solution to sustain similariton evolution in a fiber laser. Hirooka et al. demonstrated that a passive dispersion-decreasing normal dispersion fiber can be used to generate parabolic pulses with 1.5 μm wavelength [76]. This dispersion-decreasing fiber can effectively act as a gain fiber, which supports the similariton evolution. [76]

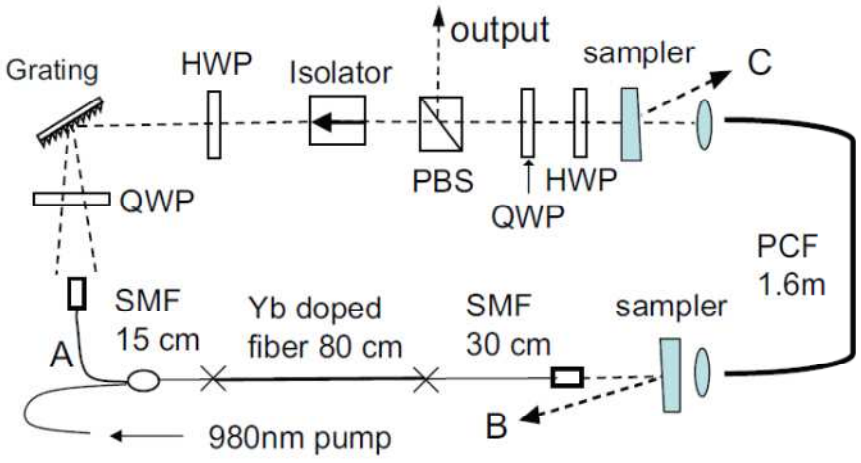

Figure 49: Experimental setup of PCF similariton fiber laser. PCF: photonic crystal fiber; SMF: single mode fiber; HWP and QWP: half- and quarter-wave plate; PBS: polarizing beam splitter.

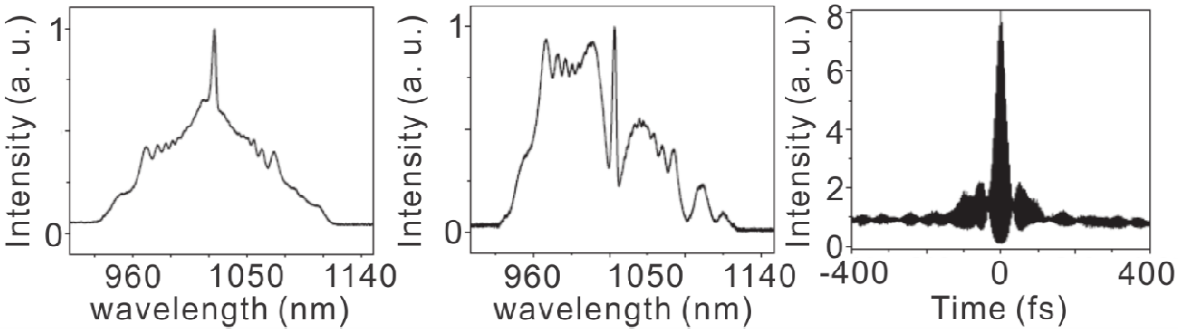

Figure 50: Experimental results. (a) spectrum before PBS; (b) output spectrum; (c) autocorrelation results

2.4 Conclusion

Systematic studies of all-normal dispersion fiber laser system were conducted. A few cavity parameters such as fiber length, spectral filter bandwidth and pump power were tested to see how they affect laser performance. It was found that a narrow spectral filter greatly improve the output spectral bandwidth that resulted in a 41 fs pulse duration. Meanwhile, more than 20 nJ pulse energy was still delivered. The compressed pulses had a peak power of about 250 kW that was the highest value achieved from a single-mode fiber laser. It will be important to test this laser for applications such as multi-photon microscopy.

Chapter 3 Application of Ultrafast Fiber Laser – Multiphoton Microscopy

This chapter discusses the application of an ultrafast fiber laser to multiphoton microscopy. Different multiphoton imaging methods such as two-photon excitation microscopy (TPEF), second harmonic generation (SHG) and third harmonic generation (THG) microscopy are demonstrated. Several biological samples are imaged. Both single layer and depth-resolved images are shown.

3.1 Introduction

Due to the benefits of high contrast ratio, sub-micrometer resolution and depth-resolved imaging, multiphoton microscopy has proven to be a powerful tool for studying living tissues [6, 56]. Especially for SHG or THG microscopy, no sample labeling is needed and no limits are imposed by the two-photon absorption spectrum either, which makes those methods preferable for non-invasive in vivo tissue imaging. In addition, SHG and THG provide complementary information due to their different optical-response mechanisms. One property of THG microscopy is that no signal is generated by a beam focused inside a homogeneous medium. This is caused by the Gouy phase-shift across the focus of the excitation beam (normally Gaussian profile) [19]. Gouy first observed that a spherical converging light wave experienced a π phase change in passing through its focus. Different from an infinite plane wave, a Gaussian beam contains a collection of wave vectors in many directions. The phase difference between a Gaussian beam and an infinite plane wave is defined by [77]

$$\phi(z) = \arctan\left(\lambda z / \pi\omega_0^2\right) \tag{45}$$

where λ is the wavelength, z is the beam position, the beam is traveling in the +z direction, and ω_0 is the beam waist. When the Gaussian beam goes through its focus, z effectively changes

from -∞ to +∞ and the corresponding phase shift $\phi(z)$ is π. Therefore, THG from a homogenous medium is canceled for the case of perfect phase matching (k_3 - $3k_1$ = 0), where k_3 is the wave vector of the third-harmonic field and k_1 is the wave vector of the fundamental field. [19]

In contrast, THG is sensitive to inhomogeneity, where the refractive index or third-order susceptibility $\chi^{(3)}$ changes. It makes THG microscopy ideal for revealing the fine structure of biological samples [78, 79]. SHG is sensitive only to media without a center of symmetry; for example structural proteins such as collagen and tubulin. For both SHG and THG imaging, ultrashort laser pulses are preferred to achieve good multi-photon efficiency. It is found that SHG or THG efficiency is inversely proportional to the pulse duration or pulse duration squared, respectively [57, 80, 81], making them amenable to ultrashort pulse excitation. Laser-pulse-duration dependence has been confirmed for two-photon excitation microscopy down to 10 fs pulses [80].

Different ultrafast solid state laser sources, such as Ti:sapphire at 800 nm [82], Cr:forsterite at 1230 nm [83] and optical parametric oscillator (OPO) at 1500 nm [78], have been used for third harmonic generation microscopy. For clinical use, a compact and environmentally stable laser is preferred to a complicated solid-state laser. In the past decade, compact fiber lasers have drawn increasing attention due to their compact size and greater stability [31, 61, 84]. Typical fiber lasers are operated around 1,040 nm (Yb), 1,550 nm (Er) or 2,000 nm (Tm). Although longer wavelengths increase the scattering length and allow deeper imaging, water absorption beyond 1,200 nm increases rapidly. This makes Yb fiber lasers operating at 1,040 nm a good option for multiphoton microscopy, especially because regular objectives have good transmission in the 400 – 1,100 nm wavelength range. Furthermore, the corresponding THG, at

350 nm, can transmit through BK7 glass and does not cause as much photo-damage as the THG from 800nm light, which occurs at 266nm and coincides with the absorption maximum of DNA. In order to avoid laser induced damage to living tissue and enable microscopic imaging deeper into living tissue, interest has shifted towards imaging using longer wavelength sources [85].

Here two fiber lasers delivering sub-50 fs pulses centered at 1030 nm are evaluated for multi-modal microscopy using fluorescent polystyrene microspheres and a few biological samples including guppy fish (Poecilia reticulata) tails, fruit fly (Drosophila melanogaster) wings, mouse kidneys, mouse intestines and Drosophila larvae. Images generated by TPEF, SHG and THG are compared.

3.2 Multiphoton microscopy using low power sub-30 fs fiber laser

3.2.1 Experimental setup

The experimental setup shown in Figure 51 consists of an Yb fiber laser oscillator (Figure 51(a)) that generates a broadband spectrum centered at 1030 nm with ~50 mW average output power at a repetition rate of 62 MHz. It is based on an all-normal dispersion cavity scheme [61] where self-similar amplification takes place in the gain medium. The pulses gain energy and bandwidth while evolving into a parabolic temporal profile in the gain segment [61] and maintain the parabolic profile in the PCF segment with the temporal and spectrum bandwidth increasing. The condition for self-similar amplification is facilitated by introducing a narrow spectral filter consisting of a grating and a collimator [61]. The self-similar pulses are further extended in both temporal and spectral domains by an intra-cavity segment of normal dispersion photonic crystal fiber (PCF). This novel scheme enables the laser spectral bandwidth to exceed the gain bandwidth and leads to pulse durations as short as 20 fs. The detailed design and principle of the fiber laser is discussed in Ref. [86].

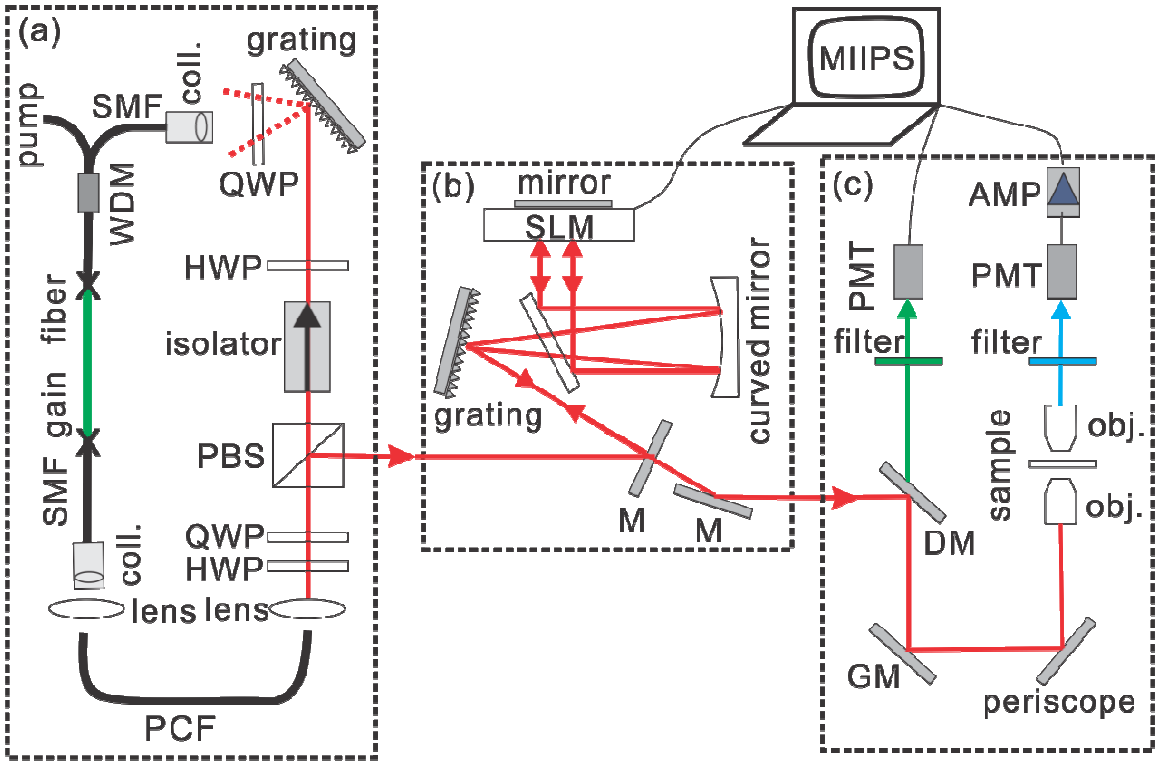

Figure 51: Schematic of imaging setup. (a) Fiber laser cavity layout. PCF: photonic crystal fiber; SMF: single mode fiber; WDM: wavelength-division multiplexer; HWP and QWP: half- and quarter-wave plate; PBS: polarizing beam splitter; coll.: fiber collimator. (b) 4f-folded pulse shaper. SLM: spatial light modulator; M: mirror. (c) Microscopy setup. DM: dichroic mirror; GM: galvanic mirror; AMP: amplifier; PMT: photomultiplier tube.

A folded 4f pulse shaper (MIIPS Box 640, Biophotonic Solutions) [Figure 51(b)], with a dual mask 640-pixel spatial light modulator, is used to measure and compensate the dispersion of the output pulses at the focal plane of the microscope [Figure 51(c)] [53, 54]. The results obtained using automated pulse compression (MIIPS) are confirmed by interferometric AC and by theoretical calculation. Due to the reflection efficiency of the grating and mirrors inside the shaper, the average power out of the shaper is ~25 mW.

The laser beam is raster scanned by a pair of mirrors mounted on galvanometers (QuantumDrive-1500, Nutfield Technology, Inc.) and coupled into a water-immersion objective (Zeiss LD C-APOCHROMAT 40x/1.1) mounted on an adapted Nikon TE-200 inverted

microscope. Laser pulses are compressed to their transform-limit at the focus of the objective. With the sample placed at the focus of the objective, the SHG or TPEF is collected in the epi direction. The SHG/TPEF is separated from the fundamental light using a dichroic mirror (700DCSPXR, Chroma Technology Corp.) and is further filtered by a short-pass emission filter (ET680-SP-2P8, Chroma Technology Corp.). A photomultiplier tube (PMT, HC20-05MOD, Hamamatsu) is used to collect the SHG/TPEF. THG, which is primarily generated in the forward direction, is collected by a UV compatible objective (HP ReflX, NT59-886, NA 0.28, focal length 13.3 mm, transmission more than 85% from 200 nm to 700 nm, Edmund Optics). The THG is also separated from the excitation light by a UV-pass filter (UG11, transmission from 250 nm to 400 nm) and detected by a PMT (H10720-210, Hamamatsu) whose signal is amplified (SRS445, Stanford Research Systems). Tens of frames are taken to generate one image and each frame takes 1s to acquire.

The spectrum of the laser pulses, after the microscope objective, is shown in Figure 52(a). Dispersion compensation for the laser as well as the microscope objective is achieved using MIIPS program [53, 54]. Briefly, the pulse shaper scans reference phase functions across the spectrum of the pulses and uses the SHG spectral information (generated by a KDP crystal mounted at the focal plane of the objective) to measure the second derivative of the spectral phase. Through double integration of the measurement the system determines the dispersion that needs to be corrected and the pulse shaper implements the correction. In order to confirm that the compression is complete, the measured SHG spectrum is compared with calculated results based on the fundamental laser spectrum and assuming no phase distortions. The excellent agreement between the calculated and experimentally measured SHG spectra in both linear and log-10 scales is shown in Figure 52(b) and (c).

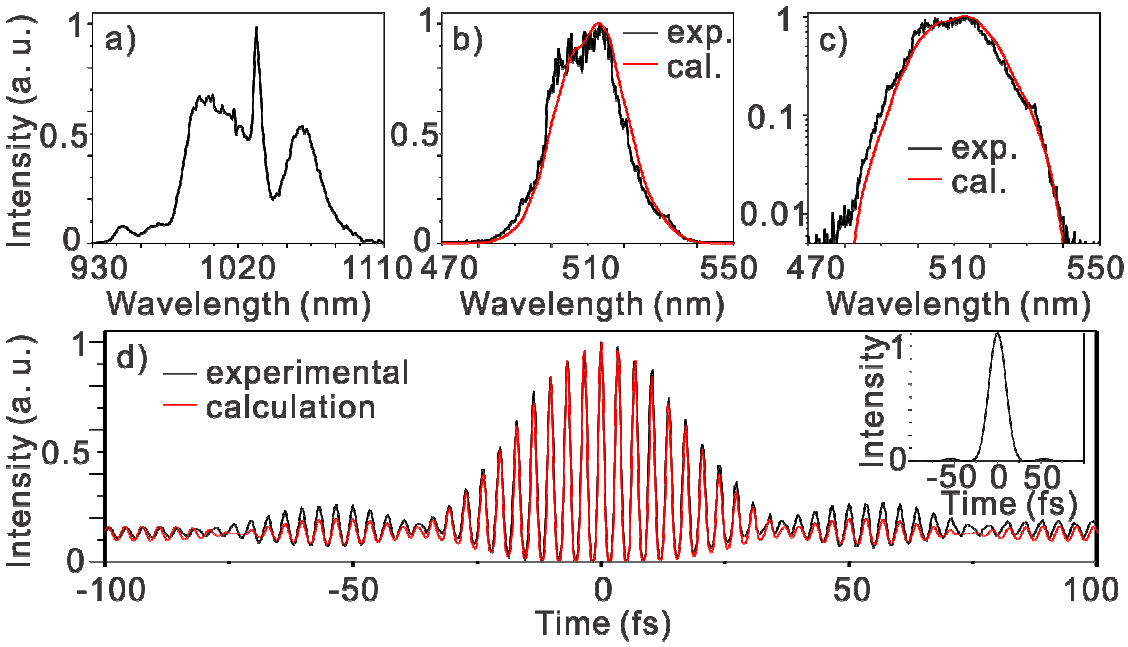

Figure 52: (a) Laser spectrum after the microscope objective. (b) Comparison of experimental (black) and calculated (red) SHG spectrum in linear scale. (c) Comparison of SHG spectrum in log-10 scale. (d) Comparison of experimental (black) and calculated (red) interferometric autocorrelation trace. Insert: calculated temporal profile based on the measured laser spectrum

After pulse compression, the pulse shaper is used to create two pulse replicas and scan one of them in time to obtain an in-situ interferometric AC at the focal plane of the objective [72]. The full-width at half-maximum (FWHM) duration of the experimental interferometric AC, shown in Figure 52(d), is 38 fs corresponding to FWHM pulse duration of 27 fs. This pulse duration is confirmed by comparing experimental and calculated interferometric AC traces, as shown in Figure 52(d). The small wings on the transform limited pulse are caused by the sharp features of the laser spectrum (Figure 52(a)). According to the calculated temporal profile based on the measured laser spectrum, there is around 95% pulse energy within the main pulse. The measured pulse duration after the microscope objective is longer than the 21 fs measured for the compressed pulse duration measured before the objective. The additional pulse broadening is caused by the reduced transmittance of the objective (70% to 50% in the 950 nm to 1150 nm

spectral range). After compression and characterization, the KDP crystal is replaced with the microscopy samples.

3.2.2 Space time coupling

Given that a good spatial mode is required for microscopy, there has been some concern whether 4*f* pulse shapers introduce spatial distortions due to space-time coupling (STC). It is an important issue and needs to be taken care of when using a 4*f* pulse shaper. There have been a number of studies about STC caused by 4*f* pulse shapers and by acousto-optic programmable dispersive filters (AOPDF) in the past two decades [87-90]. According to Ref. [88], under pure phase modulation introduced by a 4*f* pulse shaper, the beam profile at the focal plane of the objective is only determined by the incident beam profile. Basically, in our experiment setup, we focus the laser beam using an objective after the pulse shaper. The spatial distribution of the beam on the focal plane of the objective is only determined by the input beam profile and does not depend on space-time coupling. Space-time coupling only contributes some temporal distortion to the beam at the focal plane of the objective. The effect is very small and can be ignored. Detailed discussion is shown below.

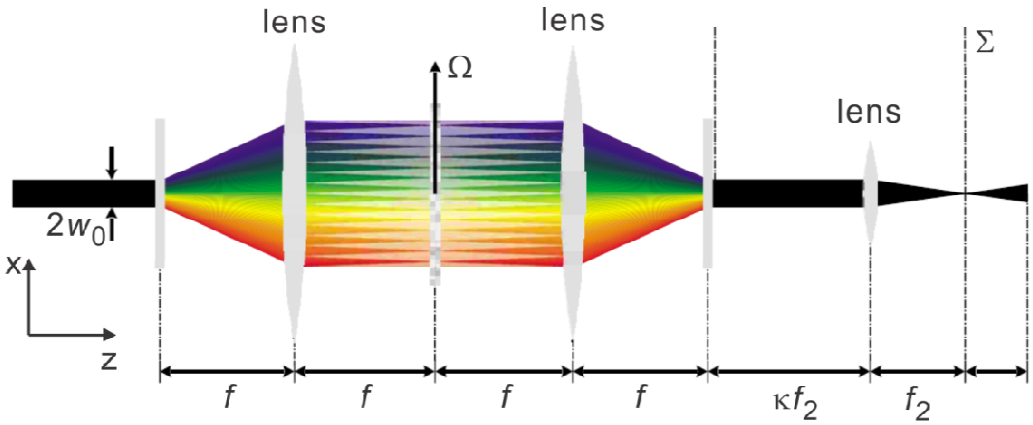

Figure 53: Sketch of 4-f shaper with output beam focused using a lens. [91]

Figure 53 shows the scheme for a laser beam passing through a 4-*f* shaper and being focused by an extra lens outside the shaper. As discussed in Ref. [91], the electric field of the laser beam at the focal plane (Σ) of the focusing lens after the pulse shaper can be described as

$$\tilde{\varepsilon}_f(x,\Omega) \propto \tilde{\varepsilon}_i\left(-\frac{k_c}{f_2}x,\Omega\right) M\left(\frac{f\gamma}{k_c}\Omega+\frac{fb}{f_2}x\right)\exp\left(i\frac{\kappa-1}{2}\frac{k_c}{f_2}x^2\right), \qquad (46)$$

where w_0 is the beam waist, $\tilde{\varepsilon}_f$ is the electric field at the focal plane of the lens after the shaper, $\tilde{\varepsilon}_i$ is the electric field of the input laser pulses, k_c is the wave vector of the center wavelength of the input pulses, f_2 is the focal length of the lens after the shaper, κf_2 is the distance between the shaper output and the lens after the shaper, $\Omega = \omega - \omega_c$ is the relative frequency and ω_c is the center frequency, and grating parameters $\gamma = 2\pi/(\omega_c d\cos\beta_c)$ and $b = \cos\theta/\cos\beta_c$ (d is the groove spacing of the grating, θ is the incident angle, and β_c is the diffraction angle at center frequency ω_c).

Based on Equation (46), the spatial distribution of the beam at the focal plane of the lens after shaper is determined by the incident pulse profile $\tilde{\varepsilon}_i(k_x,\Omega)$ and the transfer function $M(\frac{f\gamma}{k_c}\Omega+\frac{fb}{f_2}x)$. Since we only do pure phase modulation here, the transfer function $M(\frac{f\gamma}{k_c}\Omega+\frac{fb}{f_2}x)$ is supposed to be only a phase term and will not introduce amplitude modulation to change the beam spatial distribution at the focal plane. Therefore the beam shape at the focal plane is only determined by the incident pulse profile $\tilde{\varepsilon}_i(k_x,\Omega)$, which means the input Gaussian beam will end up as a Gaussian beam at the focal plane of the objective in our experiment. Space-time coupling does not affect the beam shape at the focal plane.

The dependence on the x coordinate will introduce some frequency shift to distort the pulses in the temporal domain. This frequency shift can be described as

$$\delta\Omega(x) = -\frac{bk_c}{\gamma f_2} x. \tag{47}$$

The relative frequency shift can be described as $\frac{\delta\Omega}{\sigma_\omega}$, where σ_ω is the spectral bandwidth of the incident beam.

$$\begin{aligned} \sigma_w &= \frac{N\Delta x_p}{\alpha}, \\ \alpha &= \frac{\lambda_c^2 f}{2\pi c d \cos(\beta_c)}, \end{aligned} \tag{48}$$

where α is the spatial dispersion on the SLM, N is the number of pixels covered by input laser spectrum, and Δx_p is the SLM pixel size.

$$\frac{\delta\Omega}{\sigma_\omega} = \frac{bk_c}{\gamma f_2} x \frac{\alpha}{N\Delta x_p} = \frac{bk_c}{\frac{2\pi}{\omega_c d \cos(\beta_c)} f_2} \frac{\frac{\lambda_c^2 f}{2\pi c d \cos(\beta_c)}}{N\Delta x_p} x = \frac{b}{N\Delta x_p} \frac{f}{f2} x, \tag{49}$$

$$\begin{aligned} x &= 2\frac{f_2 \lambda_c}{\pi w_{in}}, \\ w_0^{SLM} &= \frac{f\lambda}{\pi w_{in}}, \end{aligned} \tag{50}$$

where x is determined by the beam size at the focal plane of the focusing lens after the pulse shaper, and w_0^{SLM} is the beam radius of monochromatic light on the SLM. Hence,

$$\frac{\delta\Omega}{\sigma_\omega} = \frac{2bw_0^{SLM}}{N\Delta x_p}, \tag{51}$$

where N is the effective pixel numbers. Here we also assume that $2w_0^{SLM}$ is equal to Δx_p and the grating is in Littrow configuration (b=1). In our experiment setup, $2w_0^{SLM}$ is even smaller than Δx_p. We have about 600 pixels of SLM covered by the input laser spectrum. By calculation, the ratio of the shift in our experiment is about 0.17%. This small amount of distortion can be neglected. If we re-organize the formula above,

$$\delta\Omega = b\frac{\sigma_\omega}{N}\frac{2w_0^{SLM}}{\Delta x_p}. \qquad (52)$$

In the Littrow configuration, b=1, and $\frac{\sigma_w}{N}$ is the spectral resolution per pixel, which is also the spectral resolution of the shaper. Basically, the smaller $\frac{2w_0^{SLM}}{\Delta x_p}$ is, the less the space-time coupling. When $\frac{2w_0^{SLM}}{\Delta x_p} = 1$, the frequency shift is equal to the spectral resolution of shaper. Further reducing the spot size of a single color on the SLM will not help to reduce the frequency shift, which is limited by the spectral resolution of the shaper. So using a spot size on the SLM equal to or smaller than the SLM pixel size is the way to minimize the space-time coupling.

3.2.3 Experimental results

Fluorescein (emission from 470 nm to 650 nm) stained polystyrene microspheres (Fluoresbrite® YG Carboxylate Microspheres 6.00µm, Polysciences Inc.) were used to test the system before imaging live tissues.

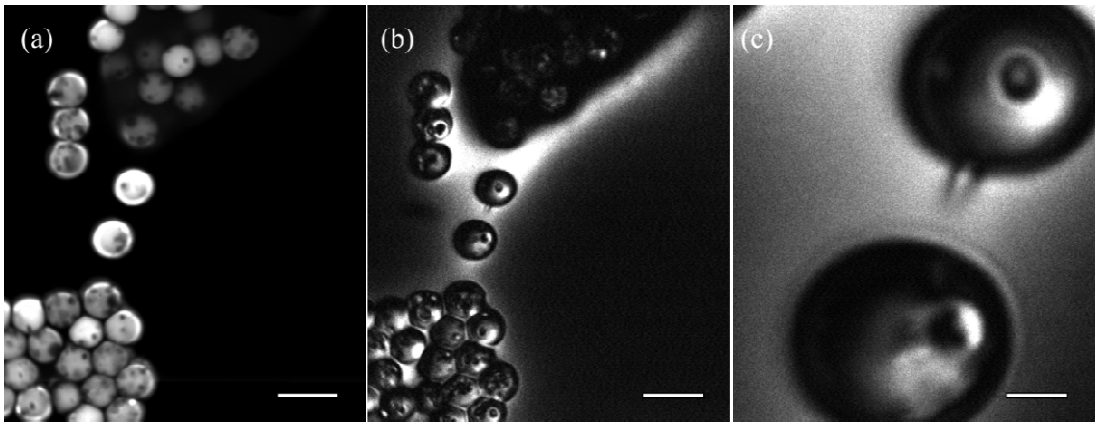

Figure 54: Multiphoton microscopy images of polystyrene microspheres. (a) TPEF image, (b) THG image and (c) THG image of single bead. Scale bar: 10 μm.

The signal in the epi detection corresponds to TPEF, and the signal in the forward direction corresponds to THG. The galvanic mirrors control the area of the sample imaged, as shown in Figure 54. Comparing the images generated by TPEF and THG in Figure 54(a) and (b), THG images have much better contrast. By limiting the scan range (Figure 54(c)), a ~1 μm feature that arises from the fabrication of the microspheres can be seen on the 6 μm microspheres. The conditions for THG in microscopy have been discussed by Silberberg [78]; essentially, a change in index of refraction is required to break the backward-forward symmetry near the focal plane. The index of refraction of polystyrene is ~1.57 for 1 μm wavelength light, a large change compared to the index of refraction of air ~1. Therefore THG is expected and observed from the surface of polystyrene microspheres. Unlike THG, the TPEF is due to the emission from fluorescein that coats all over the microspheres.

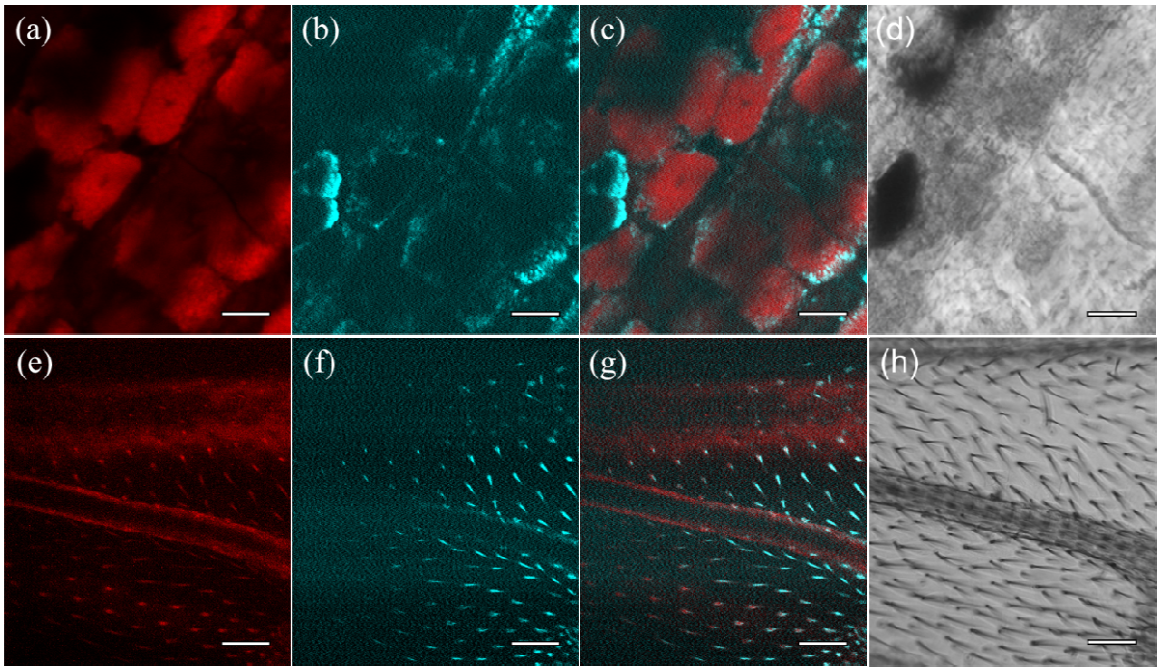

Figure 55: Multiphoton microscopy images of live tissues. (False color) Top line: images of a guppy fish (Poecilia reticulata) tail. (a) SHG image (false color, red), (b) THG image (false color, cyan), and (c) Composition of SHG and THG images. (d) Bright-field microscope image. Bottom line: images of fruit fly (Drosophila melanogaster) wings. (e) SHG image (false color, red) (f) THG image (false color, cyan) (g) Composition of SHG and THG images. (h) Bright-field microscope image. Scale bar: 10 μm.

Imaging of biological tissues, unstained samples of fly wings and fish tails, was used to demonstrate the practical relevance of the laser. The samples were mounted on glass slides with Tissue-Tek O.C.T. compound (Sakura, CA) and allowed to immobilize for 30min before imaging. The laser intensity used for imaging the fish tail was 17 mW. The laser power for imaging fly wings was reduced to 7 mW, because higher power was found to damage the sample. Bright-field images were checked before and after imaging to make sure there is no damage to the sample after excitation (Figure 55(d) and (h)]. The SHG (Figure 55(a) and (e)) and THG (Figure 55(b) and (f)) images are shown in false color.

SHG and THG results are complementary because they arise from different phase conditions. SHG requires non-centrosymmetric structures while THG requires a change in the

index of refraction. By merging the SHG and THG images, we can clearly see the complementary results in Figure 55(c) and (g). The THG from fish tail is not as intense as the SHG because of sample thickness. However, there is some complementary information at the edge of the cells provided in the THG images, which is due to the enhanced THG at the interface. On fly wing, the strongest THG is from the fine hairs. Note that the use of sub-30 fs pulses resulted in comparable SHG and THG signal levels from fruit fly wings even when using only ~0.1 nJ pulse energy from a fiber laser.

As shown above, this sub-30 fs fiber laser is successfully demonstrated for multi-modal biomedical imaging. The shorter pulse durations achieved by the laser greatly enhance two- and three-photon induced modalities in both stained and unstained living tissues. Complementary results of SHG and THG from living tissue are shown under similar laser conditions. However, due to the low pulse energy of this laser, it cannot deliver enough photons to deep tissue to enable depth scan imaging. A high-power fiber laser while still providing ultrashort pulses is needed. This led to the testing of a 40 fs high-energy similariton fiber laser for multi-photon microscopy.

3.2 Multi-photon microscopy using high pulse energy sub-50 fs fiber laser

3.2.1 Experimental setup

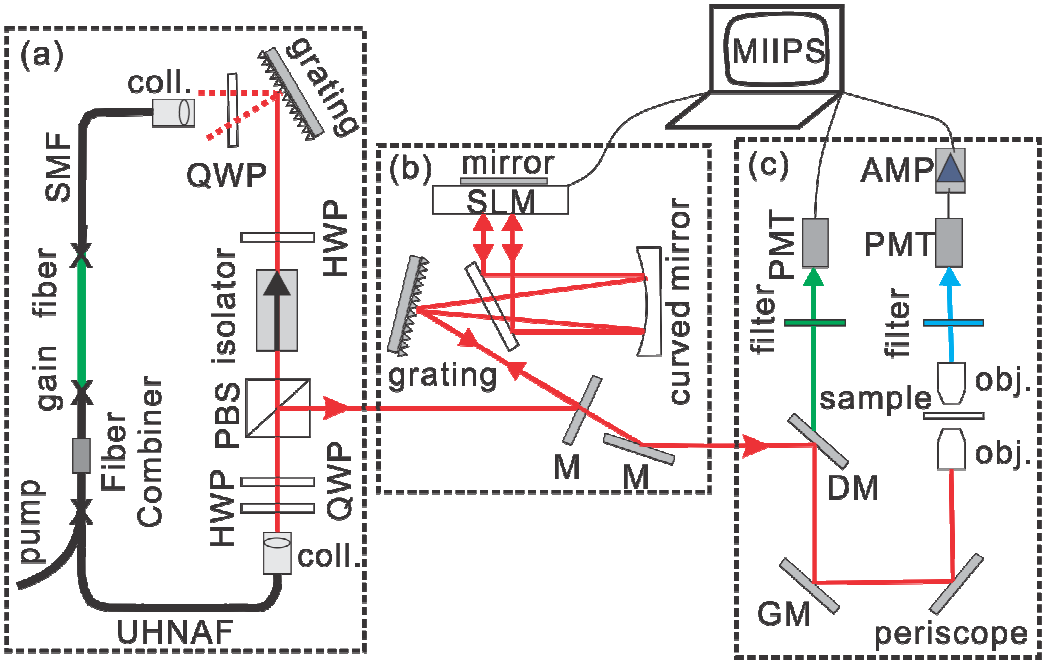

Figure 56: Experimental setup. (a) Fiber laser. HWP and QWP: half- and quarter-wave plate; PBS: polarizing beam splitter; SMF: single mode fiber; UHNAF: ultra-high numerical aperture fiber; coll.: fiber collimator. (b) 4-f folded pulse shaper. M: mirror; SLM: spatial light modulator. (c) Laser-scanning microscope. DM: dichroic mirror; GM: galvanic mirror; obj.: objective; PMT: photon multiplier tube; AMP: amplifier.

The experimental setup, shown in Figure 56, is similar to the previous setup but with the laser source replaced with the similariton fiber laser described in Chapter 2. Since these two laser sources have similar spectral range, all the optics and acquisition devices remain the same.

3.2.2 Experimental results

The pulse compression routine is the same as described previously. No loss of spectral bandwidth is experience for this laser due to its slightly narrower spectrum. After pulse compression, samples are loaded at the focal plane of the objective. To calibrate the microscope, two stained commercial samples (mouse kidney and mouse intestine, Molecular Probes) that

have uniform thickness were imaged. For these two samples, the signal detected in epi direction is mainly from two- or three-photon excited fluorescence, since these samples are stained (Mouse intestine with Alexa Fluor® 350 WGA, Alex Fluor® 568 phalloidin and SYTOX® Green; Mouse kidney with Alexa Fluor® 488 WGA, Alex Fluor® 568 phalloidin and DAPI). In the forward direction, mainly THG/three-photon-excited fluorescence is detected. By combining the signal from epi and forward directions, it is clearly seen that they provide complementary information for each other (see Figure 57).

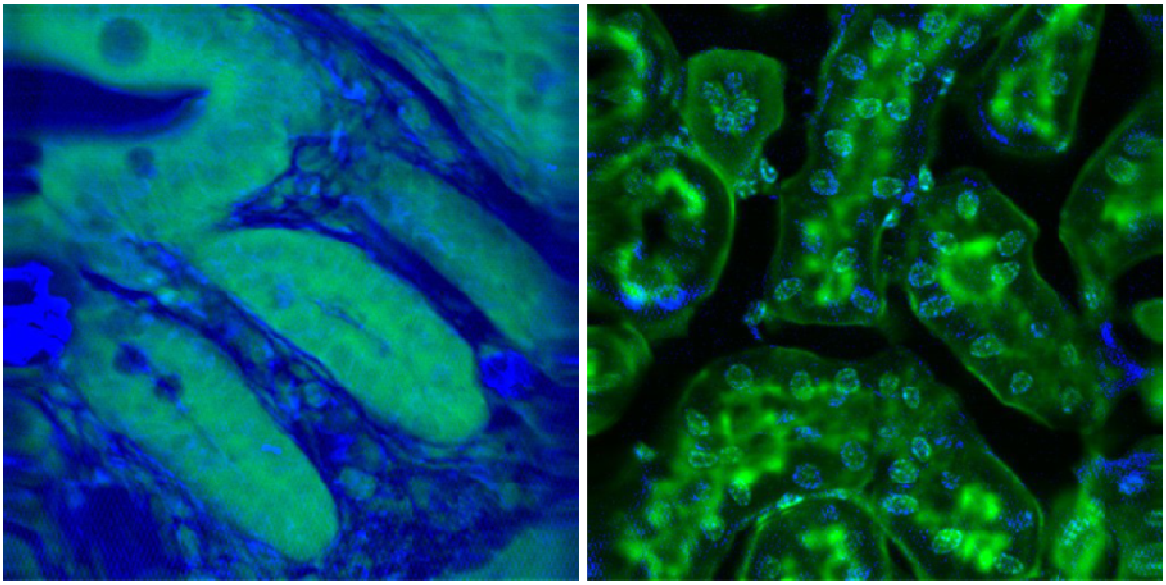

Figure 57: Composition of TPEF (green, false color) and THG (blue, false color) imaging of mouse intestine (left) and mouse kidney (right), 150 μm x150 μm area represented.

Beyond imaging processed and pre-labeled samples, we are more interested in imaging living tissues, especially to elucidate their three-dimensional structures. Compared to the fiber laser delivering 30 fs pulses used for multi-photon imaging of living tissues, this laser can provides 10 times more pulse energy with only slightly longer pulse duration, which enables depth resolved imaging in thick biological samples, such as Drosophila larvae.

Third instar (a stage in the life of an arthropod between two successive molts) Drosophila larvae were mounted onto the sample platform. The trachea of a larva was centered within the image. Here, depth-resolved imaging is achieved by moving the focal plane of the objective across the sample in 2 μm steps. The total scanned depth is about 90 um. SHG and THG signals are collected from epi and forward directions, respectively. Three-dimensional images are constructed by stacking all the frames from each step in order. The projections of the constructed SHG and THG three-dimensional images at different angles are shown in Figure 58. It can be seen that the THG three-dimensional image shows a lot more fine structure and provides more detailed information and less scattering than the SHG image.

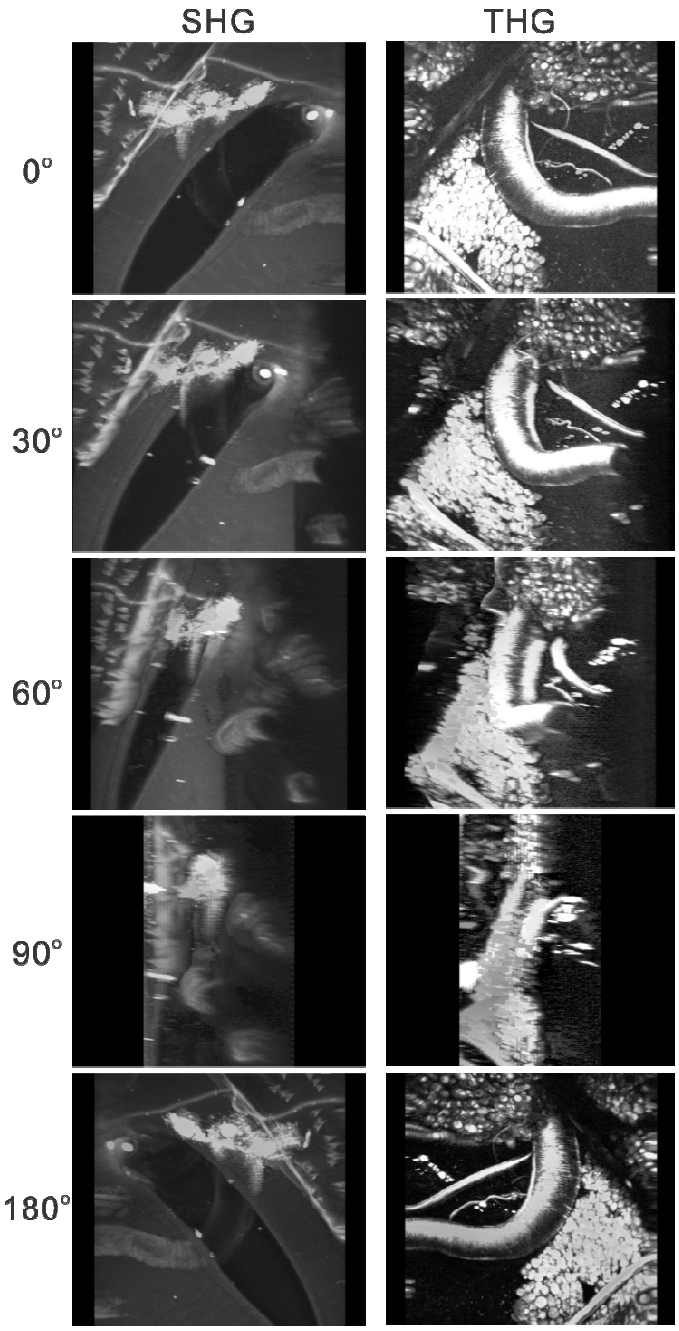

Figure 58: Projection of three-dimensional images at different angles of SHG (left) and THG (right) microscopy of Drosophila Larva. 150 μm x150 μm area represented.

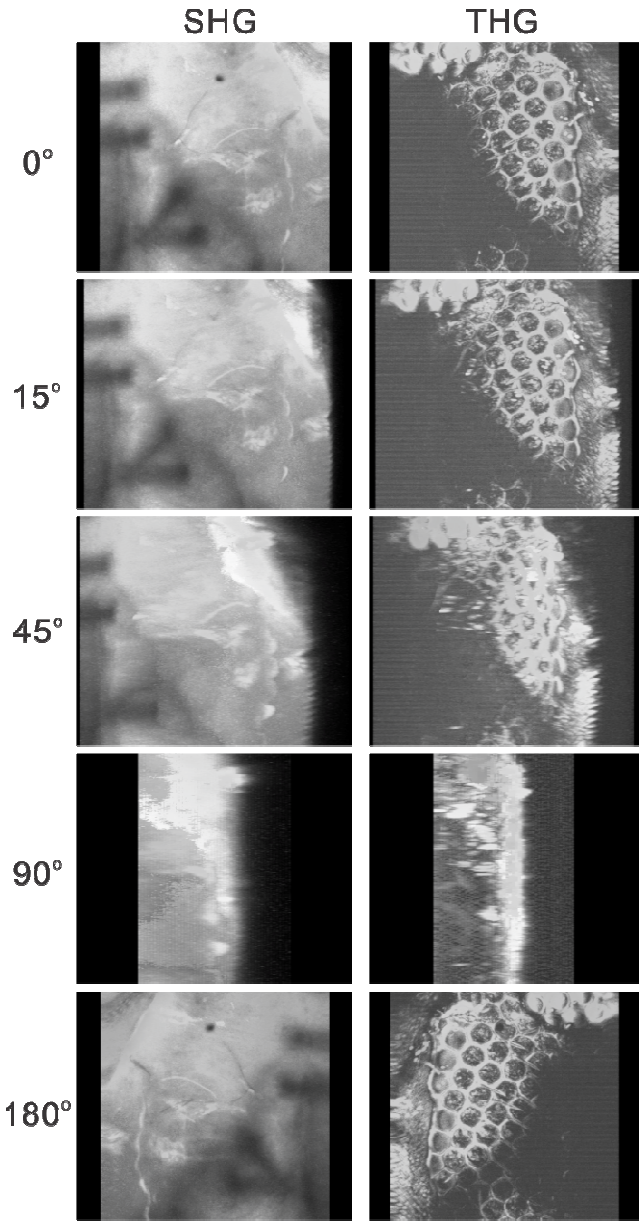

Figure 59: Projection of three-dimensional images at different angles of SHG (left) and THG (right) microscopy of fruit fly eyes. 150 μm x150 μm area represented.

The same SHG and THG three-dimensional reconstructed imaging were also demonstrated using fruit fly eyes. In Figure 59, a few projections are shown and compared. It is found that THG three-dimensional imaging shows much better contrast ratio and is a better solution for depth scanning of biological tissues.

3.3 Conclusion

We have demonstrated the use of two ultrafast fiber lasers for multi-modal biomedical imaging. The ultrashort pulse durations achieved by both lasers greatly enhance two- and three-photon induced modalities in both stained and unstained living tissues. Complementary results of SHG and THG from living tissue are shown under similar laser conditions. Depth-resolved imaging of Drosophila larva and fruit fly eyes using a high energy, sub-50 fs Yb fiber laser is achieved. Three-dimensional reconstructed imaging based on THG shows much better contrast in resolving the tissue structures. It shows that this high-power similariton fiber laser is a suitable source for deep tissue imaging.

Chapter 4 Development of Noise-like Fiber Laser and Their Applications in Laser-Induced Breakdown Spectroscopy

In this chapter, fiber oscillators that can deliver pulses with pulse energy up to 450 nJ is demonstrated. These fiber lasers are operated in a very different mode-locking regime – noise-like – compared to all the lasers discussed in previous chapters. It is found that these lasers are ideal light sources for laser-induced breakdown spectroscopy.

4.1 Introduction

One of the major laser applications is laser ablation [7]. When a laser pulse of sufficient energy and intensity is focused onto a material, a small amount of the material is ablated, forming a plasma spark that radiates on atomic emission lines. By detecting the atomic emission spectra and comparing it to a standard database, elements present in the material can be analyzed. This technique is known as Laser Induced Breakdown Spectroscopy (LIBS) and has become a common analytical method because it is virtually instantaneous, highly sensitive, and suitable for samples in any kind of physical states [92, 93]. Since its discovery, LIBS has been demonstrated for a wide variety of applications including the analysis of products in the steel industry [94, 95], works of art and archaeological artifacts [96], terrestrial and Martian geological samples [97, 98], and the detection of toxic [99] or explosive materials [100]. It is even used for space exploration and there is a LIBS system installed on the famous Mars Rover.

Since most of LIBS measurements are carried out outside the laboratory, portable LIBS instruments are in high demand. As a key part of the system, a portable and powerful laser source is needed. Recent developments in fiber laser technology have provided more robust laser sources. Fber-laser-based LIBS systems in both the nanosecond [101] and femtosecond regimes [102] have been demonstrated. For LIBS systems employing nanosecond laser pulses [103-106],

plasma ablation is a thermal effect with a timescale comparable to that of the laser pulse. The use of nanosecond pulses results in a high ablation threshold due to heat diffusion during the pulse arrival, and the resulting spectrum is mixed with a strong continuum of radiation caused by free-state transitions of electrons in the laser field. Nanosecond LIBS therefore requires a complex gated spectrometer to isolate atomic emission and pulse energies of >10mJ, which leads to extensive thermal damage to the sample. The use of ultrafast pulses can overcome these problems by delivering energy on timescale orders of magnitude faster than thermal effects [107, 108].

Besides pulse duration, there are a few more parameters that affect laser ablation efficiency and threshold. It has been found that a burst of laser pulses can significantly improve ablation efficiency [109, 110]. LIBS results using single pulses and bursts of pulses are compared in [109], see Figure 60. The burst contains multiple pulses with each pulse of about 20 ns and separated by 10 μs interval. The temporal duration of the burst being about 700 μs. It has also been shown that, there is a 5-fold increase in material ablation rates when six lower-energy pulses separated by 20 ns are used, compared to a single pulse with energy equal to the sum of the burst [110]. These observations indicate that a laser with a high repetition rate, like MHz, can help improving ablation rate. Current Q-switched or amplified laser systems usually have low repetition rates down to the kHz or Hz level. These results can be explained through a several-step process. The sample surface absorbs the first laser pulse and gets heated above the melting point, which causes explosive material ablation. If the second pulse comes before the vapor of initially ejected material disappears (the restoration time about 100 μs), it can skip the step of melting the material and generate more atomic emission.

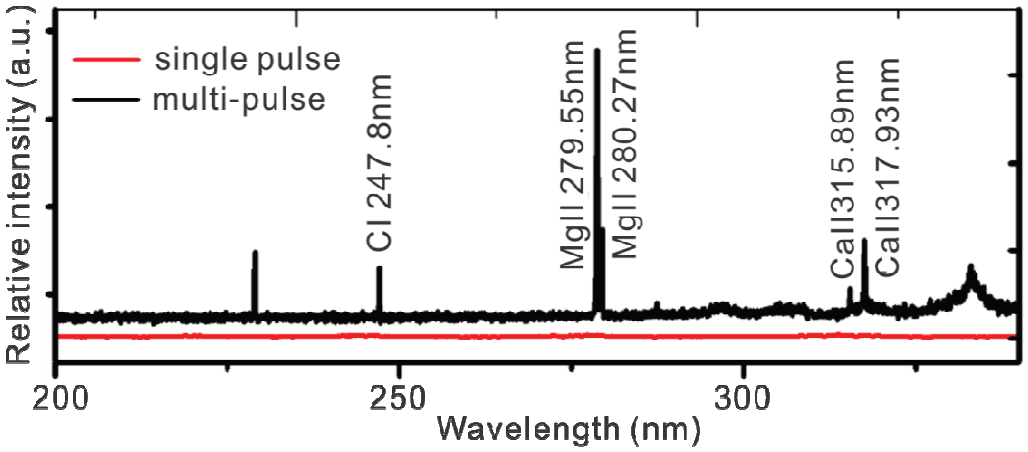

Figure 60: LIBS spectra captured by using multi-pulse (black) and single-pulse (red) configurations. [109]

Although femtosecond laser ablation is not a thermal process, multiple femtosecond pulses also help LIBS by lowering the ablation threshold. These femtosecond pulses are more closely spaced than those of burst mode. It has also been reported that two femtosecond pulses separated by 200 ps lowered the ablation threshold by half compared to a single femtosecond pulse [111]. In that study it was observed that two pulses yield a hotter and longer lived plasma, and pulse delays greater than 50 ps were found to yield greater signal, presumably because they allow time for plasma dissipation [111, 112].

There are also some other factors affecting the ablation threshold, such as pulse duration and spectral bandwidth. The fluence threshold of ablation is known to increase with $\tau^{1/2}$ for τ greater than 10 ps [113-115], where τ is the laser pulse duration. When the pulse duration is less than a few picoseconds, the ablation threshold is nearly constant for metals [114, 115]. It is also found that increasing the spectral bandwidth of a femtosecond pulse lowers the laser ablation threshold [116], see Figure 61. Although changes in the bandwidth also change the pulse duration, it has been shown that pulse duration alone does not affect the ablation threshold by applying second order dispersion to the pulses [116].

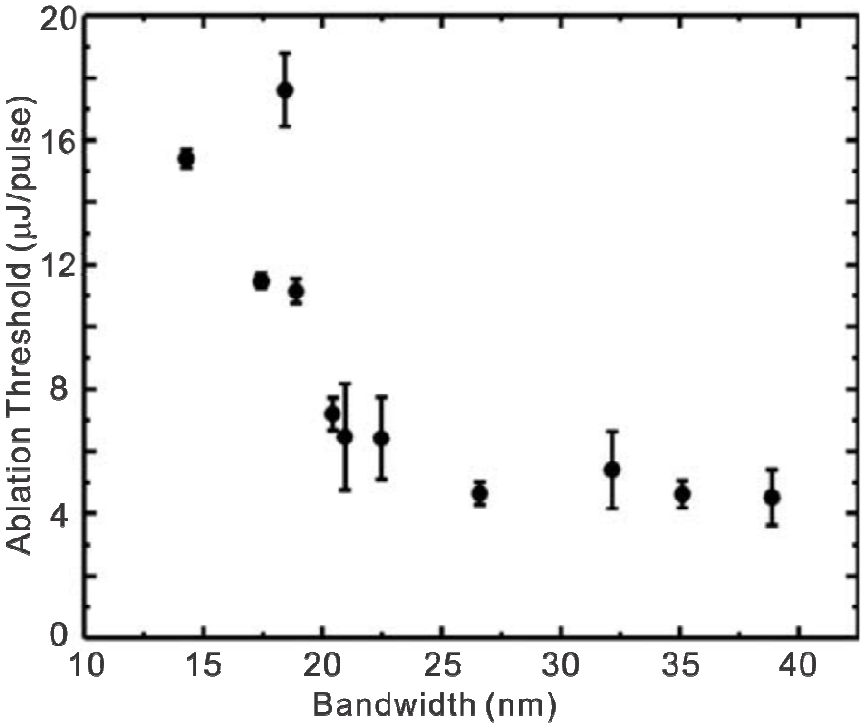

Figure 61: Spectral bandwidth dependence of the LIBS threshold. [116]

Based on these studies, an ideal LIBS laser source should have high pulse energy, high repetition rate and broadband spectrum. It would be also good to have multiple femtosecond pulses with ultrashort time intervals. This leads us to study an unusual mode-locking regime producing noise-like pulses that can provide the laser parameters discussed above.

In the past two decades, ultrafast fiber laser research has led to the observation of different mode-locking pulse formation regimes such as soliton [29], dissipative soliton [31], and similariton [32]. Efforts to generate high-peak-power pulses using conventional single-mode fibers are typically limited to 0.5 MW [84]. Under high-gain and high-dispersion conditions the single-pulses break into multiple pulses, a regime that has been considered as “noise-like” pulses [117-121]. This regime usually generates picosecond or nanosecond long trains of pulses, each containing hundreds of sub-pulses.

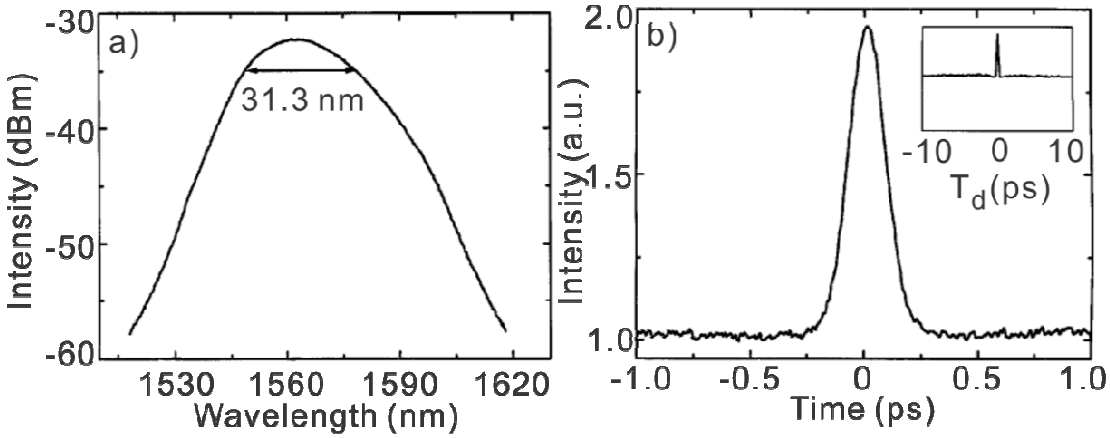

Figure 62: Experimental results of noise-like laser. (a) output spectrum (b) background-free autocorrelation trace. [117]

This regime was first studied analytically and numerically in a soliton laser [122]. In this work, authors found the generation of a train of quasi-stable localized pulses in the region where a single soliton is unstable [122]. Later, it was experimentally demonstrated in an Er fiber laser [117, 123]. A broad output spectrum (Figure 62(a)) was obtained from this laser [117], corresponding to about 50 fs pulse duration. However, autocorrelation measurements showed a much longer pulse duration that lasted over 10 picoseconds with a FWHM 190 fs sharp spike in the middle of the trace (Figure 62(b)). Numerical simulation was carried out to investigate these unusual pulses (Figure 63) [117]. The simulation showed noise-like pulses that contain a large number of sub-pulses with random amplitude and phase within a temporal window lasting tens-of-picoseconds (Figure 63(a)). The simulated autocorrelation trace also matched the experimental results qualitatively (Figure 63(b)). However, this noise-like pulse is different from pure noise or a CW laser. The laser is still mode-locked or at least partially mode-locked, which is indicated by the broad spectrum. The narrow spike on the autocorrelation trace is an artificial coherent spike. Polarization dependent delay (PDD) is explained as the main reason for the generation of these noise-like pulses. Large PDD is caused by the significant birefringence in the fiber, and corresponding nonlinear cavity transmission splits pulses.

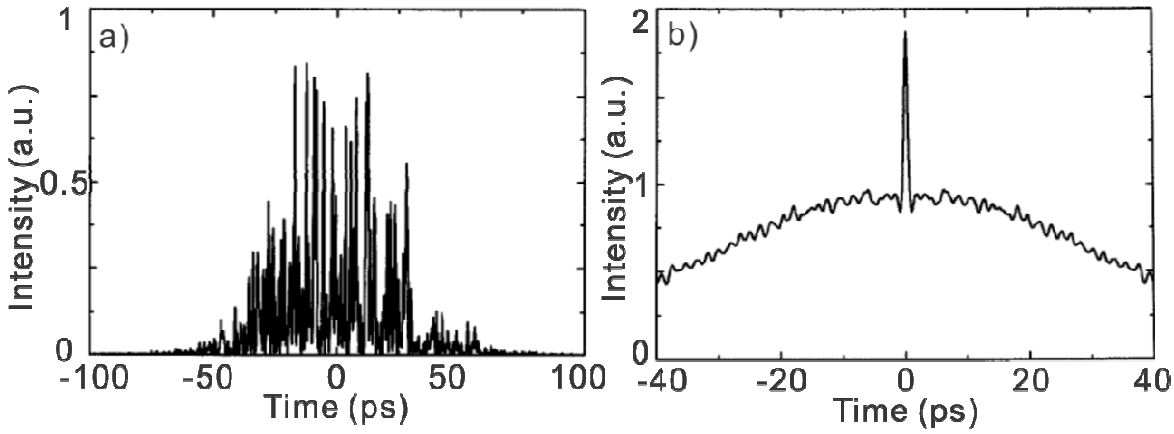

Figure 63: (a) Calculated time-dependent intensity and (b) autocorrelation trace. [117]

Several other Er noise-like fiber lasers [118, 124-126] were reported later and different mechanisms of noise-like pulse formation were proposed. In [126], an Er fiber laser with weak birefringence also showed similar noise-like pulses, which ruled out the possibility that it is generated by the large cavity birefringence [117]. Instead, it showed that the formation of the noise-like pulse was caused by soliton collapse as proposed initially by theoretical work [122], and it was also a genetic feature of passively mode-locked soliton fiber lasers [118]. Basically, these noise-like pulses are attributed to peak-power clamping [118, 127]. In NPE based mode-locking fiber lasers, once the pulse peak power reaches a certain value, it cannot increase any more due to the nonlinear cavity transmission property. Further increasing the pump power will force one pulse to split into two or more pulses to avoid exceeding the peak-power limit. Also, the extra pump will amplify the background noise and the dispersive wave [127]. Thus, pulse collapse happens and noise-like pulses are generated. The highest pulse energy from an Er noise-like fiber laser is 15 nJ [128]. The first Yb fiber laser generating noise-like pulses was reported in [119], with an output pulse energy of 7.5 nJ. In reference [119], numerical simulation was also conducted to understand the noise-like pulse formation.

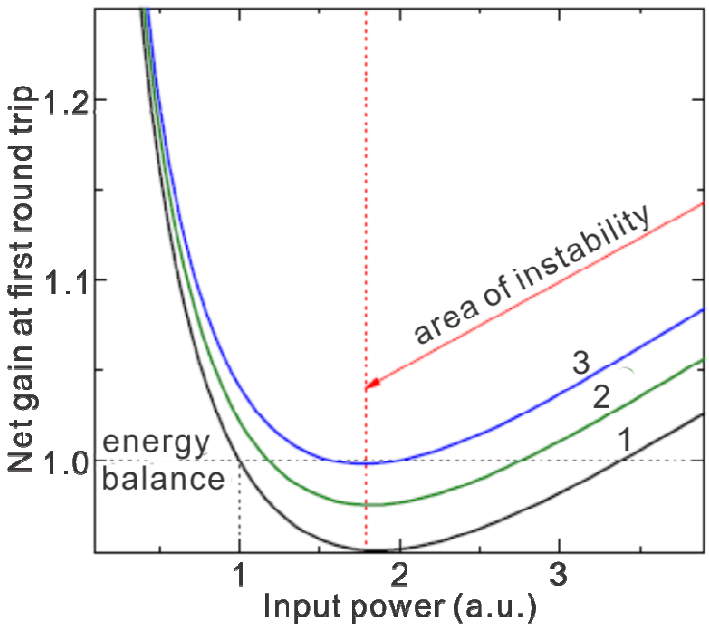

Figure 64 Net gain per roundtrip vs. initial pulse power. Curves 1-3 correspond to slightly different cavity parameters close to the boundary of the single-pulse generation regime. [119]

Figure 64 shows the net gain per roundtrip of the laser cavity, which depends on the initial pulse power and cavity parameters. Plot 1 in Figure 64 represents a cavity that can switch between regular single pulses and noise-like pulses. It shows that the net gain decreases as the initial pulse power increases on the left half of curve 1. Therefore, if the initial pulse power is less than 1, the pulse will experience gain more than 1 and increase its power after one roundtrip. If the initial pulse power of the next round trip is great than 1, the pulse will have gain less than 1 and lower its power after this roundtrip. The cavity finally will be stabilized at the point when the net gain is equal to 1. In this case, the laser is operated in the normal mode-locking regime. If the pulse evolves as in the right haft of plot 1, the net gain increases as the input pulse power increases. In this case, the pulse evolution cannot converge and the laser will switch to noise-like mode.

Due to the partial coherence in temporal domain, this type of laser has been avoided by most researchers and considered undesirable. However, some useful applications such as

metrology, grating-based sensing [117-121] and supercontinuum generation [117-121] have been demonstrated using these pulses. Also due to its broad spectrum and multiple femtosecond sub-pulses with ultrashort time interval, it could also be a potential source for LIBS. Here, we scale up the pulse energy using an unusually long Yb fiber laser cavity and demonstrate its application for LIBS.

4.2 Experimental setup of noise-like lasers

Our noise-like fiber laser was first designed based on a similariton laser. A schematic of the laser design is shown in Figure 65. This fiber laser is based on an all-normal dispersion cavity using 10/125 μm single-mode fibers. A double clad 10/125 μm Yb doped gain fiber (2 m) is pumped with a diode laser (976 nm) through a fiber combiner. A fiber collimator with 0.35 m passive single-mode fiber (SMF-II) is spliced to the gain fiber to guide the laser beam out. A few wave-plates and a polarizing beam splitter (PBS) are used to enable mode-locking based on NPE.

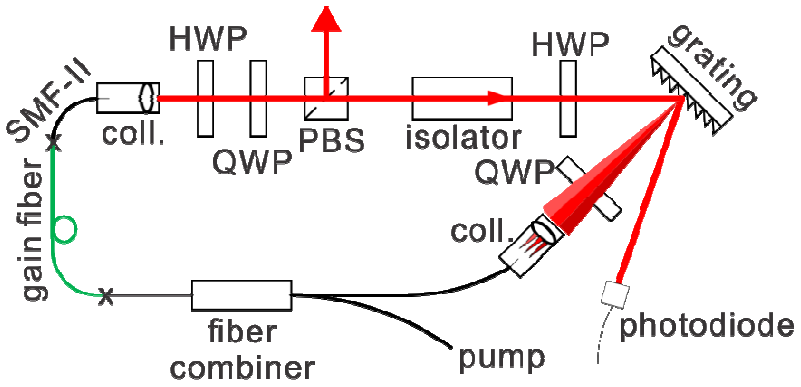

Figure 65 Experimental setup of the fiber laser. SMF-I and SMF-II: single mode fiber; HWP and QWP: half- and quarter-wave plate; PBS: polarizing beam splitter.

The major change compared to the previous laser is the length of SMF-I. As discussed in Chapter 2, the increase of SMF-I length will narrow the output spectrum and increase the corresponding transform-limited pulse duration. But this trend stops when SMF-I becomes excessively long and the laser will switch into the noise-like regime. About 100 m long SMF-I is

used here. Although lasers with shorter fibers have been shown to also reach the noise-like regime, we extend the cavity length to a much larger scale in order to scale up the pulse energy.

4.3 Experimental results

With a 3 nm bandwidth intra-cavity spectral filter and about 100 m long SMF-I, different mode-locking states can be achieved by adjusting the wave plates and pump power, due to the NPE mechanism. In this laser, pump-power dependent variation of the mode-locking state is similar to a normal fiber laser. At low pump power, single pulsing and a clean pulse train is observed. A pulse train at ~2 MHz repetition rate is shown in Figure 66. When the laser is pumped with higher power, mode-locking becomes unstable and multi-pulsing occurs preventing one to define a repetition rate. The switch between CW and mode-locking status is instantaneous and significant spectral broadening is observed.

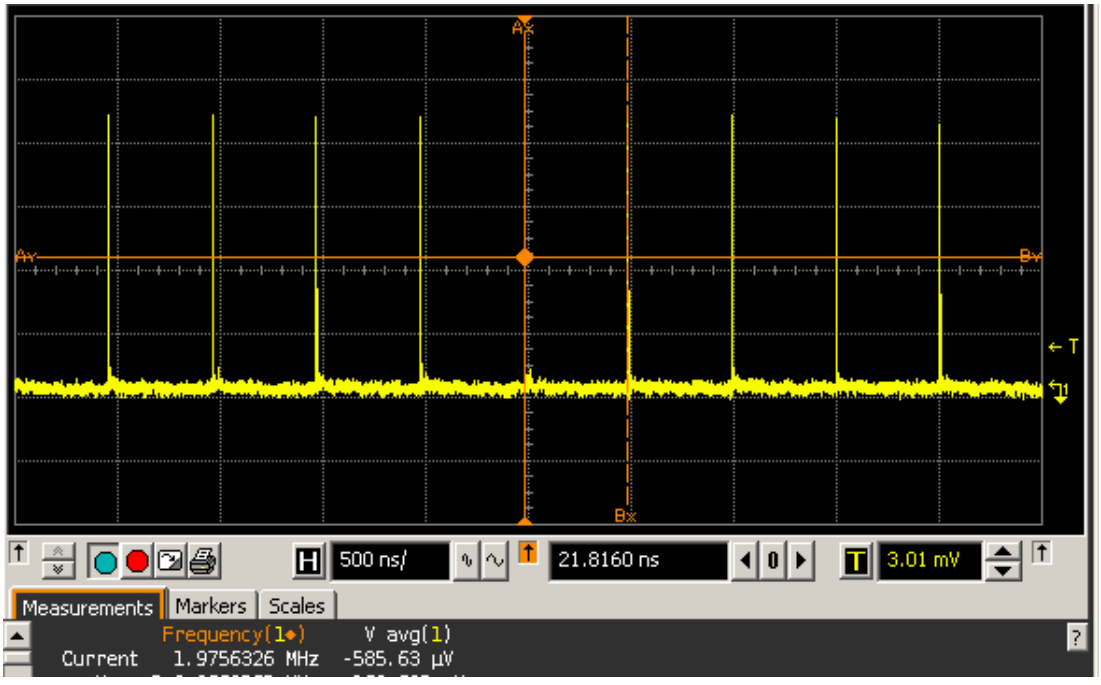

Figure 66: Pulse train of mode-locked fiber laser with 100 m long SMF-I.

An output spectrum is shown in Figure 67(a). It is smooth and corresponds to coherent pulses with about 150 fs FWHM pulse duration. The output spectral bandwidth does not change obviously by increasing pump power, while the output power increases.

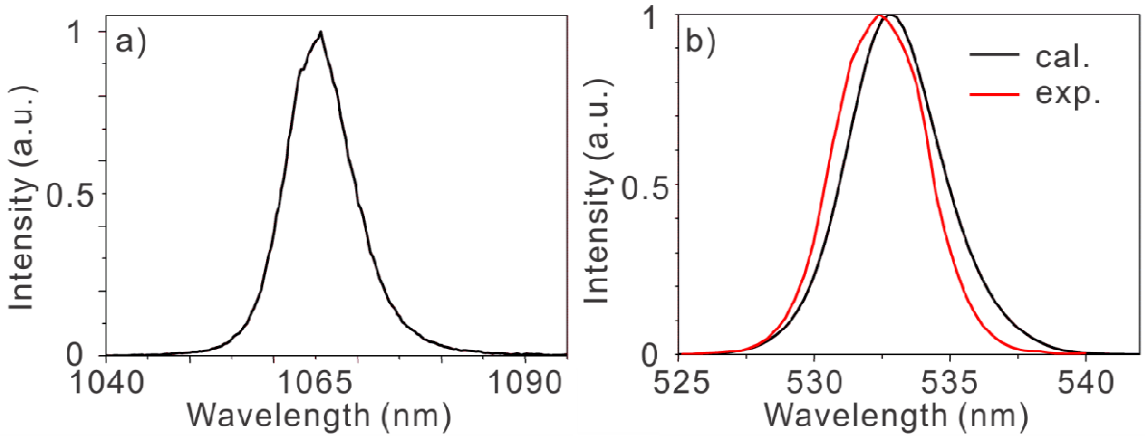

Figure 67: a) Experimental output spectrum; b) Experimental SHG spectrum with second-order dispersion compensation (SOD) applied (red) and calculated SHG spectrum with flat phase based on the fundamental spectrum.

The output pulses are characterized using a MIIPS-enabled 4-*f* pulse shaper. A chirp scan is carried out to find the maximum integrated SHG signals around -60,000 fs^2 (Figure 68 (b)). It is significantly less than the cavity dispersion, which is about 2,300,000 fs^2, indicating something unusual. With a compensation SOD of -60,000 fs^2 applied to the output pulses using the pulse shaper, the normalized measured SHG signal is not far from the calculated SHG spectrum (Figure 67 (b)), which indicates that there is at least some coherence. Also, when the laser is switched to CW mode and the output laser beam is focused on the same BBO crystal, no SHG signal is detected even at much higher average power. This proves that these pulses are real and have much higher peak power than CW mode. However, the change of integrated SHG signal is very small (only ~5 times) compared to a fully coherent pulse that can have three order of magnitude larger changes (see Figure 68(b)).

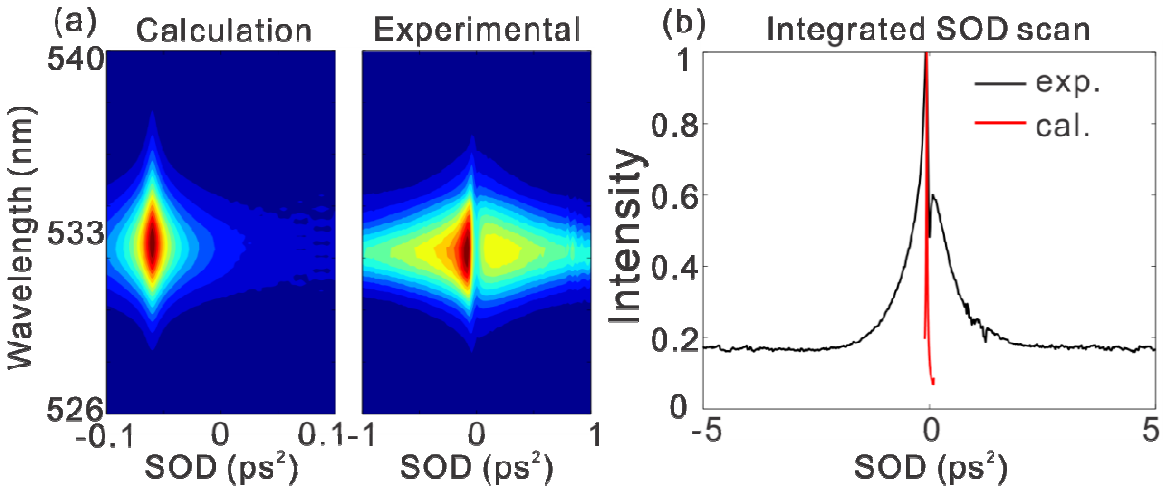

Figure 68: (a) Calculated and experimental two-dimensional SOD scan. The SOD range of the calculated plot is 10 times smaller than experimental plot. (b) Calculated and experimental SHG-integrated SOD scan.

The calculated and experimental results of SOD scan are shown in Figure 68. The calculation uses a fully coherent pulse based on the fundamental spectrum (Figure 67 (a)). A second order phase dispersion of 60,000 fs^2 is added to the coherent pulse to match the systematic phase distortion in the real pulses. In order to see the difference more clearly, the SOD range of the calculated two-dimensional SOD scan is 10 times smaller than that of the experimental results. Their SHG spectral ranges shown on the y-axis are very similar; while the SHG of the experimental result still have significant signal until 1 ps^2 SOD (see Figure 68 (a)). This is better illustrated in the SHG-integrated SOD scan results (see Figure 68 (b)). Compared to the FWHM width of calculated scan, the experimental one is ~30 times larger, which indicates the existence of the incoherent pulses.

Meanwhile, when a sinusoidal phase scan is performed and no convergence of the MIIPS trace is achieved, this also indicates that there is an incoherent part in the laser pulses. However, it can be an advantage that these pulses are much less phase sensitive, since they can be delivered by a fiber with minimal pulse distortion.

To further characterize the pulses, interferometric AC using a pulse shaper and background-free non-collinear SHG intensity AC are carried out. On the short range (± 600 fs) interferometric AC trace (Figure 69(a)), the ratio between the peak and base line is less than 8:1, which indicates the pulse lasts much longer than this time range. A long range background-free intensity AC trace is conducted to show that (Figure 69(b)). On the intensity AC trace, there is a ~200 fs coherent spike while the whole trace last over 15 ps. This matches the characteristics of noise-like pulses observed in previous work [117, 119].

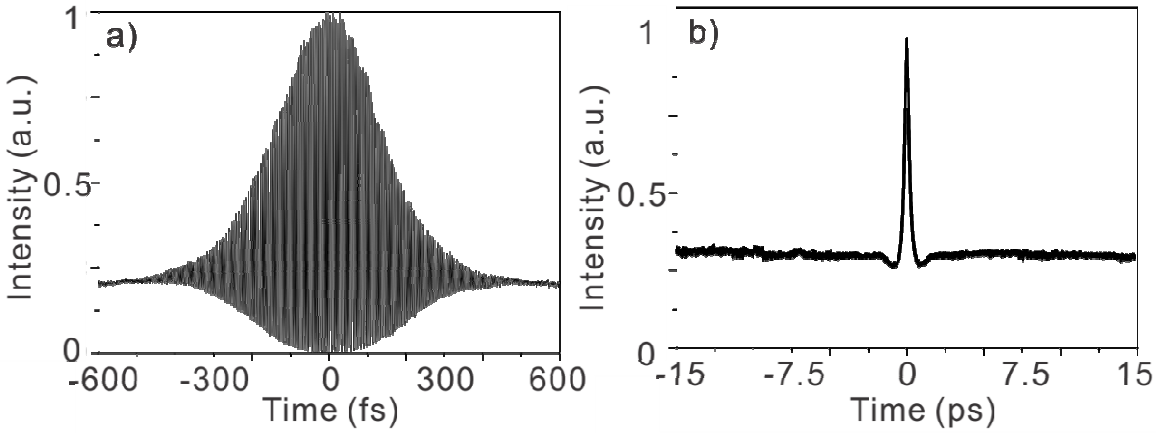

Figure 69: (a) Interferometric AC, peak-to-base-line ratio is less than 8:1; (b) background-free non-collinear intensity AC.

The distance between collimator and grating is adjusted to vary the spectral filter bandwidth. No noticeable change of output spectrum, chirp scan or autocorrelation result was observed. With this type of narrow filter, the maximum average output power is about 420 mW, corresponding to 210 nJ pulse energy.

In order to further study the filter-bandwidth-dependence of laser performance, the grating-based spectral filter is replaced by a birefringent spectral filter (12 nm or 20 nm). The resulting output spectra are broadened while the coherence of the pulses stays the same. Since the spectral filter does not play as important a role as in other lasers, it is completely removed from the cavity and the laser setup is simplified as shown in Figure 70. Similar mode-locking behavior is still

achieved with a much broader spectrum and higher output power. A maximum output power of 640 mW, corresponding to 320 nJ, is delivered from this laser. Pump-power-dependent spectral changes are shown in Figure 71.

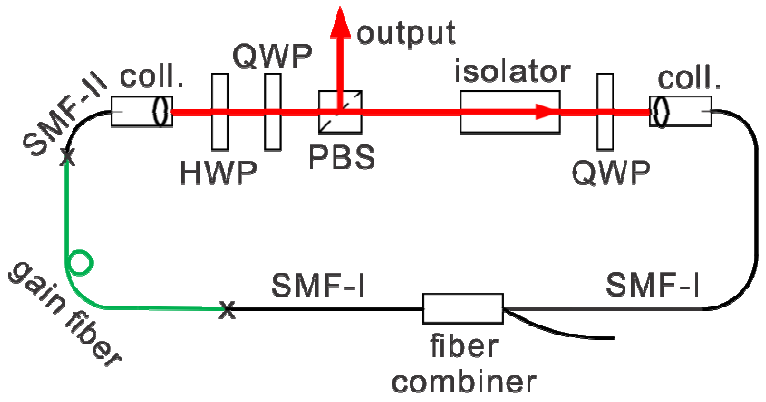

Figure 70: Simplified noise-like fiber laser setup without any spectral filter. SMF: single mode fiber; HWP and QWP: half- and quarter-wave plate; PBS: polarizing beam splitter; coll.: fiber collimator.

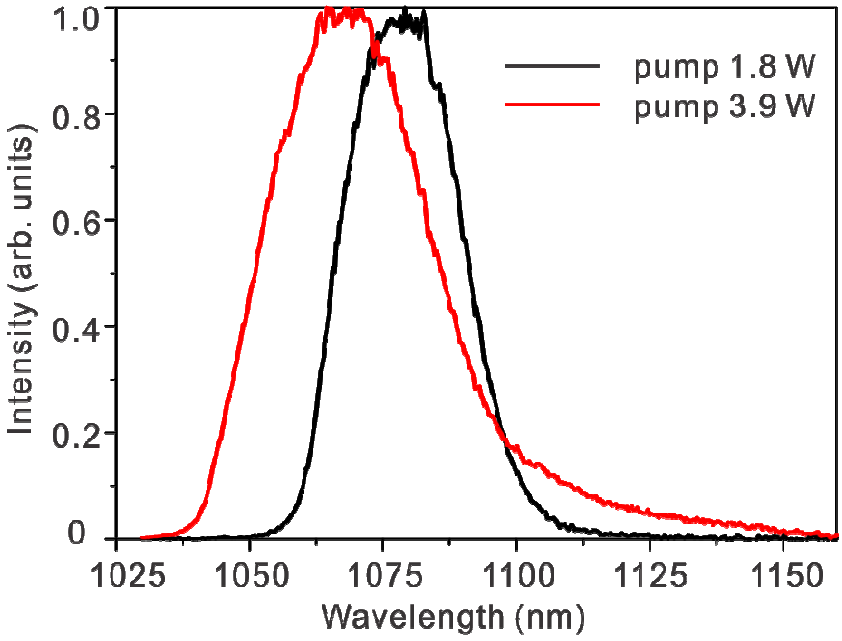

Figure 71: Pump-power-dependent output spectra. Black: pump power 1.8 W; Red: pump power 3.9 W.

With higher pump power, the output spectrum broadens to match the amplified spontaneous emission spectrum of the gain fiber. This also indicates the mechanism behind this

noise-like mode-locking – once the peak power is clamped, the excess pump amplifies the background noise.

In order to further scale up the pulse energy, an additional 100 m long fiber was added to SMF-I, mode-locking is achieved at a repetition rate of about 1 MHz [Figure 72].

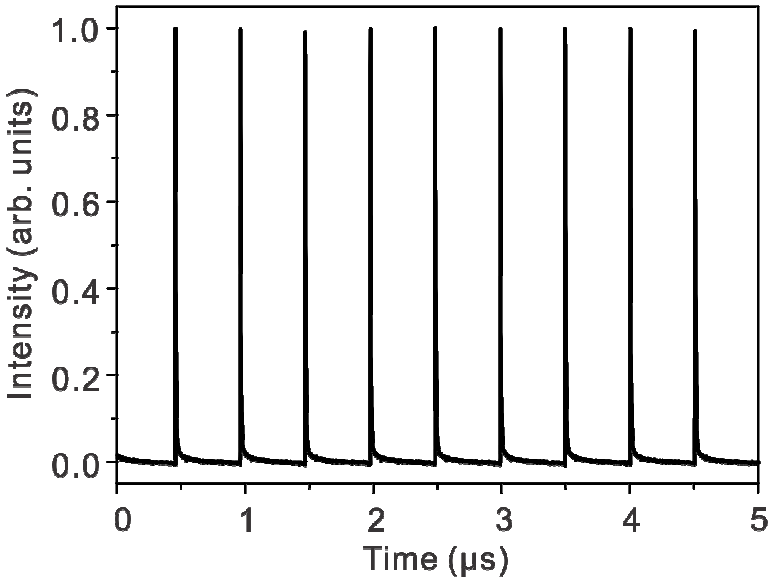

Figure 72: 1 MHz pulse train of noise-like laser with 200 m long SMF-I.

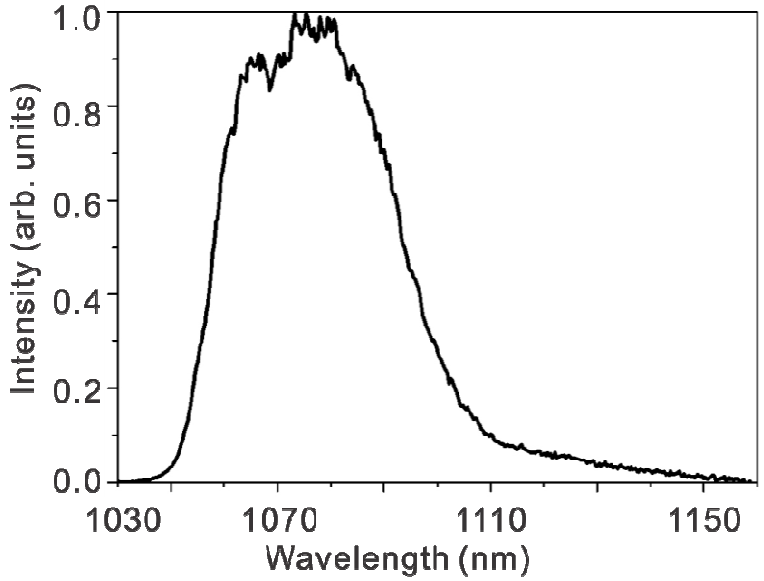

Figure 73: Output spectrum of 1 MHz noise-like laser.

A broad and smooth spectrum (Figure 73) was obtained with a maximum output power of 450 mW, corresponding to 450 nJ per pulse. Efforts to further increase the output power did not work. It was also noticed that, the change of maximum pulse energy is not linearly proportional to the inverse of the repetition rate, as we obtained 320 nJ for 2 MHz and 450 nJ for 1 MHz. Limited by gain bandwidth, no further broadening of the output spectrum was observed either.

Background-free non-collinear SHG AC measurement is used to characterize the output pulses, as shown in Figure 74. Limited by the scan range of the delay stage, only half of the AC trace is scanned to get as much information as possible about the symmetric AC trace. It can be seen that there is a large pedestal lasting over more than 180 ps with a very narrow spike on top of the trace. The base line drops to below 0.1 at 180 ps and it is believed that it will be more than 200 ps before the signal reaches zero.

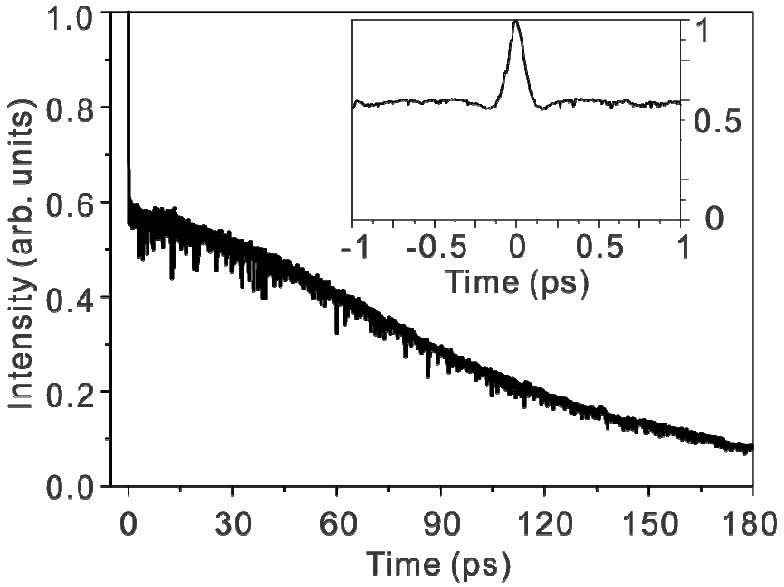

Figure 74: Non-collinear AC trace from 0 ps to +180 ps. Insert: the same AC trace on a small range from -1 ps to +1 ps.

This means that the output is characterized by multiple femtosecond sub-pulses within a 200 ps envelope. The irregular femtosecond sub-pulses result in the narrow spike in the center of AC trace. Another possibility is that each output pulse is about 200 ps long and that these pulses

fluctuate in amplitude and phase. However, according to the mechanism behind the formation of noise-like pulses and numerical simulation, the explanation of a long pulse envelope with multiple sub-pulses is more suitable for this case.

Output pulses from the noise-like fiber oscillator were also tested as a seed for a fiber amplifier. In common ultrashort pulse fiber amplifiers, a long pre-chirp fiber is needed to lower the peak power to avoid too much nonlinearity during amplification. Also, a down-counter is also used to lower the repetition rate in order to achieve higher pulse energy. Since our laser is mainly designed for LIBS and high-repetition pulses are preferred, no down-counter is used in our amplifier system. Also, due to the insensitive phase response of these pulses, no pre-chirp is needed before amplification.

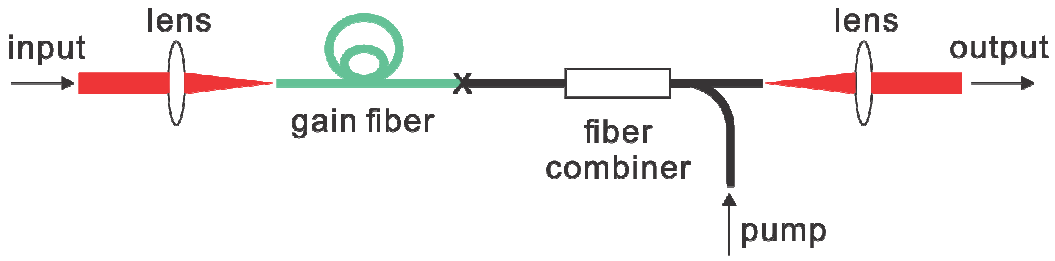

Figure 75: Setup of fiber amplifier using a noise like laser as the seed.

The amplifier setup is shown in Figure 75. A backward pumping scheme is used to achieve better efficiency. The pump laser is coupled into the output end of gain fiber using a fiber combiner. A double-clad 30 μm core diameter gain fiber (Nufern) is used. This large-mode-area (LMA) fiber is not purely single mode. By coiling it tightly, higher order modes can be filtered. The focusing lens and input end of the gain fiber are mounted on a 3-axis stage that is adjusted to optimize the coupling of seed laser into the gain fiber.

By gradually increasing the pump power, the output power increases correspondingly. Since the seed laser already has a broad spectrum close to the gain-bandwidth limit, no significant spectral broadening of the amplifier output is observed. Meanwhile, with the increase

of pump power, ASE from the gain fiber increases due to the excessive pump power. ASE can be suppressed by adjusting the setup alignment and optimizing the coupling efficiency. When the pump power reaches 15 W, the ASE signal becomes too dominant to be suppressed. The maximum clean and stable amplifier output is ~3.87 W, corresponding to 3.87 μJ pulse energy. The output spectrum is shown in Figure 76.

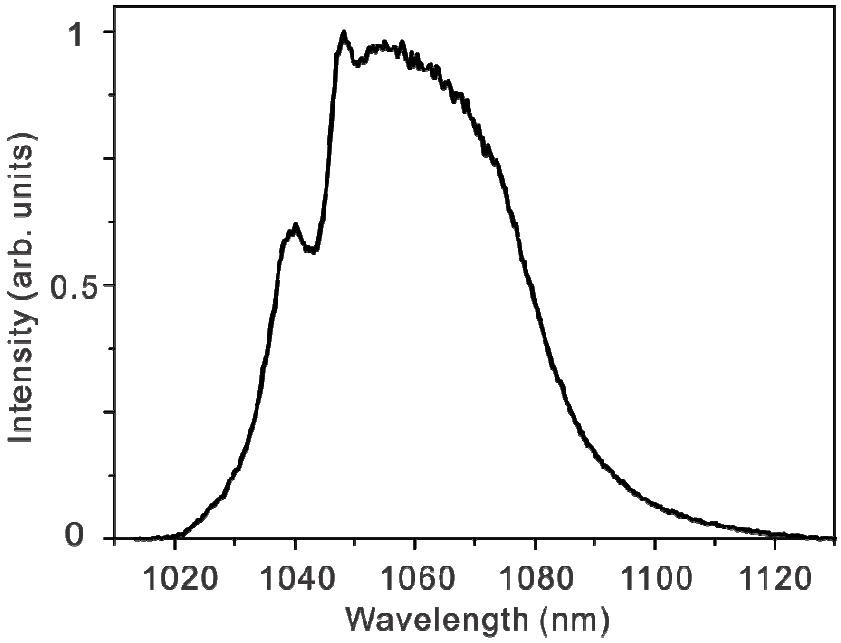

Figure 76: Output spectrum of fiber amplifier.

4.4 LIBS using noise-like laser

As described above, the laser can produce 1-2 MHz repetition rate pulses with high pulse energy and broad spectrum. The picosecond long pulse envelop consists of a number of femtosecond sub-pulses. These characteristics of the unamplified laser match the requirement for an ideal LIBS laser source. It is important to test this laser for LIBS.

4.4.1 Experimental setup

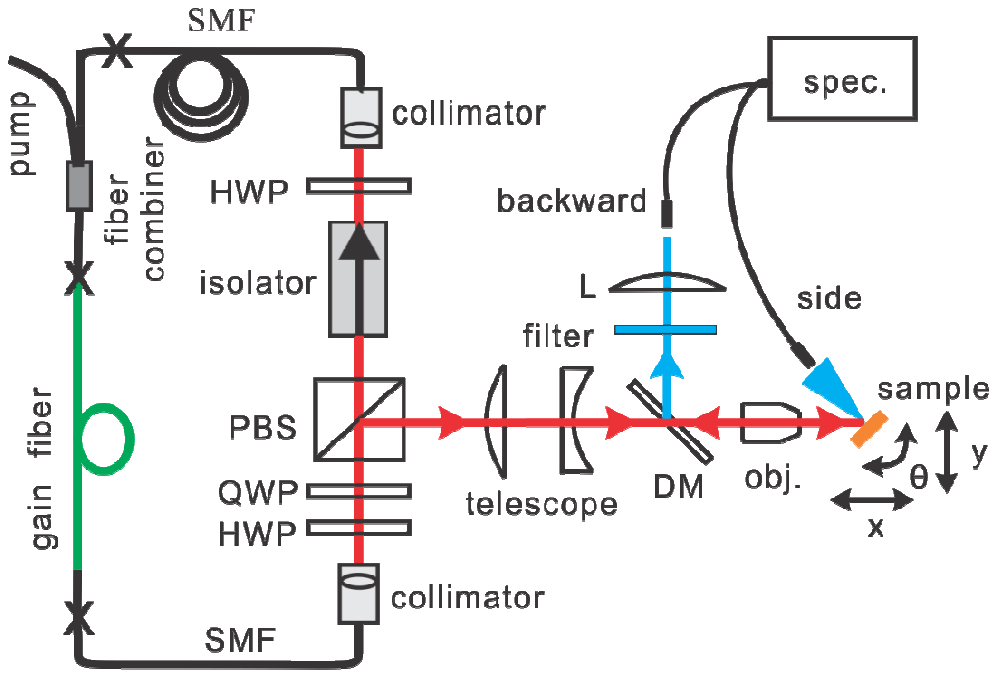

Figure 77: LIBS setup using noise-like laser. DM: dichroic miror; L: lens; spec: spectrometer; obj: objective. SMF: single mode fiber; HWP and QWP: half- and quarter-wave plate; PBS: polarizing beam splitter.

As shown in Figure 77, the output beam of the fiber oscillator is collimated with a telescope before being directed to the LIBS detection setup, without pulse compression. A 20x objective (NA = 0.4) is used to focus the beam onto the sample, which is mounted on a spinning wheel (rotation frequency 133 Hz) so that each pulse sees a fresh spot for ablation. The scattered LIBS signal can be directly collected by placing a collection fiber next to the ablation spot. The other end of the collection fiber is coupled to a compact spectrometer (178 nm – 876 nm, USB4000, Ocean Optics). The advantage of this direct side collection is to avoid any signal filtered by the collecting optics since the atomic emission can extend below 300 nm wavelength and normal glass optics will greatly attenuate those wavelengths. However, this scheme is susceptible to large background scattering in the spectrometer due to the strong excitation laser. It is important to filter all non-atomic emission signals for ablation threshold measurement. So a

backward detection scheme, with a dichroic mirror to filter out the excitation laser, is used for ablation-threshold measurement, though sacrificing the signals below 350 nm.

4.4.2 Experimental results

The results discussed below are obtained using the 2 MHz cavity output, since its pulse energy is enough to cause ablation and too much energy will generate more unwanted plasma emission that will mask the atomic emission spectra. Several samples were tested.

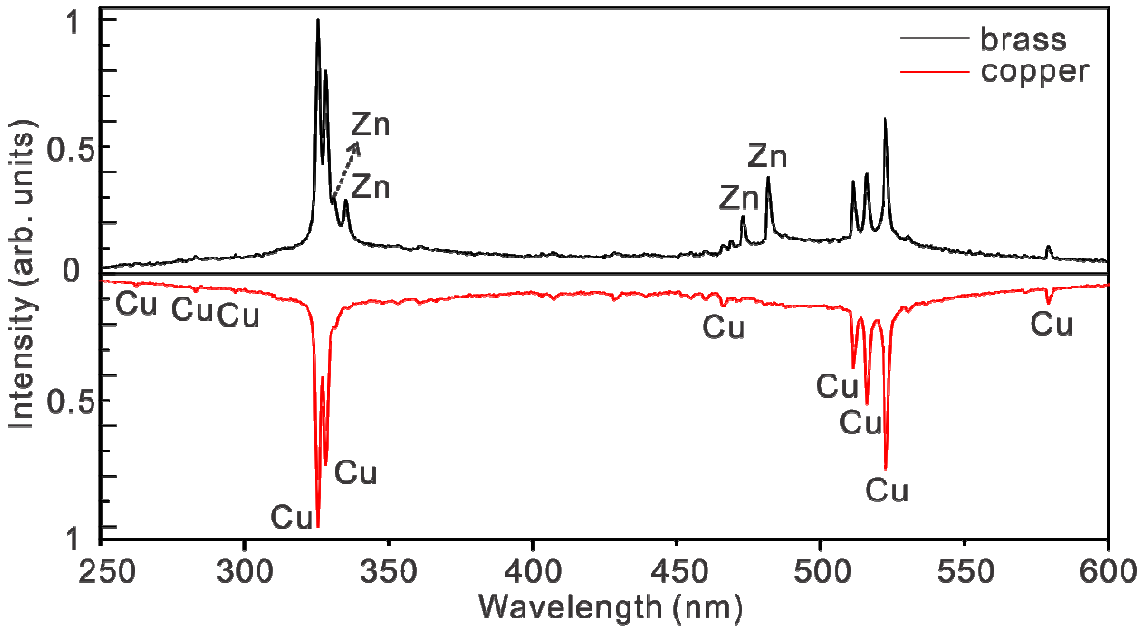

Figure 78: LIBS spectra of brass (top) and copper (bottom).

LIBS spectra of Cu and brass pieces are compared in Figure 78. Brass typically contains ~30% zinc (Zn) and ~70% Cu. On the brass spectrum, peaks are visible at 330.7 nm, 334.3 nm, 472.3 nm and 481.1 nm, which are absent in the Cu spectrum. These peaks match Zn emission lines. The other peaks, which are common to both spectra, correspond to Cu emission lines. The spectra shown above are directly recorded without using a gated-spectrometer and the continuum emission signal is insignificant compared to the atomic emission peaks. The low continuum emission also implies that there is little thermal emission, which indicates that the heat-affected

zone is limited. The simple detection system requirements further reduce the complexity and cost of the LIBS system. The fast repetition rate at 1-2 MHz, comparing to Q-switched lasers, also enhances the accumulation of LIBS signals.

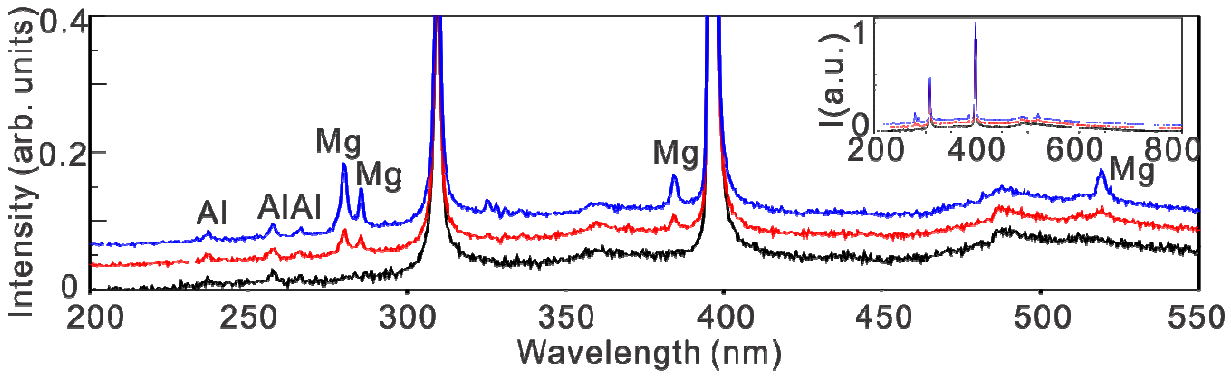

Figure 79: LIBS spectra of three aluminum alloys, Al1100 (black), Al6061 (red) and Al7075 (blue). Insert: the full LIBS spectra.

It is also important to evaluate the system's ability to qualitatively evaluate difference in composition and concentration. The aluminum alloys, Al7075, Al6061 and Al1100, were used for this test. In Al1100, there is no magnesium. Al6061 and Al7075 have about 0.8-1.2% and 2.1-2.9% magnesium, respectively. LIBS spectra of these three alloys are compared in Figure 79. Each spectrum is normalized to its highest aluminum peak. As expected, there is no Mg peak observed on Al1100 LIBS spectra. For spectra of Al6061 and Al7075, not only are multiple Mg peaks (278.3, 285.2, 383.8, 518.4nm) observed, but the change of Mg peak magnitude also qualitatively corresponds to the variation of Mg concentration in these two alloys. Quantitative results would require calibrated samples, which were not available for these tests.

One of the important LIBS applications is to detect hazardous materials. Often these hazardous materials occur only in trace amounts surround by large amounts of other materials, which makes the detection extremely hard. To evaluate our system's ability of trace detection, a $PbNO_3$-contaminated Al plate was prepared. This sample was made by applying a few drops of 6.5 mg/mL $PbNO_3$ solution on an aluminum plate and heating until the water evaporated. The

average concentration of $PbNO_3$ on the surface is <15mg/cm^2. Compared to the LIBS spectrum of Al 1100, Pb peaks are clearly distinguishable at 364.0, 368.3, and 405.8nm, see Figure 80.

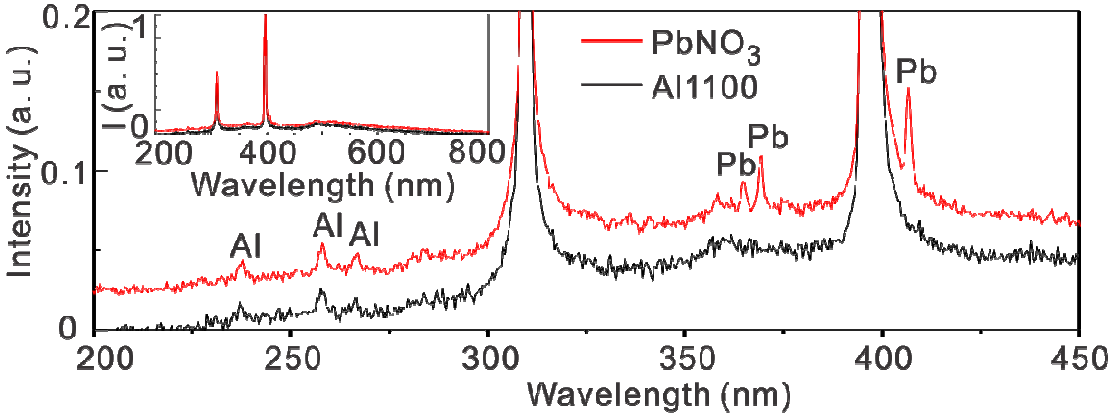

Figure 80: LIBS spectra of pure Al1100 alloy (black) and $PbNO_3$ contaminated Al1100 (red).

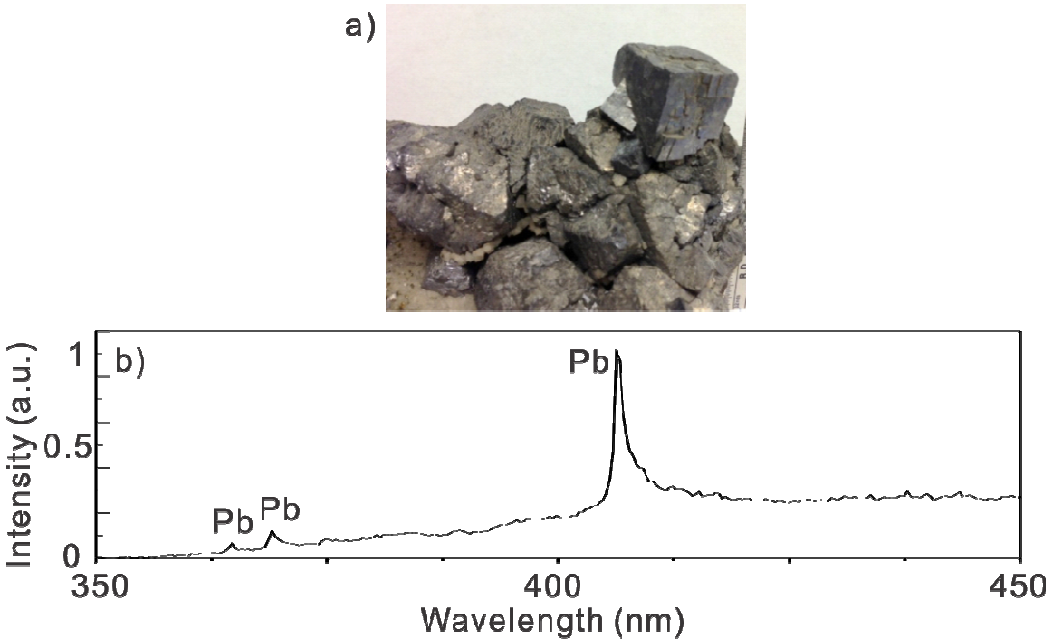

Figure 81: (a) Picture of Galena rock; (b) LIBS spectra of Galena rock.

In addition to these smooth metallic samples, a Galena (PbS) rock [Figure 81(a)] with a rough surface was also tested. Strong Pb emissions can be observed (e.g. 364.0, 368.3, and 405.8nm), as shown in Figure 81(b). This clear spectrum shows great potential for the system's

use in the mining industry, for example, for analyzing samples in the field without sample preparation.

4.4.3 Ablation threshold

The experimental threshold measurement is shown in Figure 82, which was carried out on Cu. Nonlinear fitting of the experimental data gives threshold fluence values around 0.25 J/cm^2. It was reported that when using a 5 ns Q-switched Nd:YAG laser the threshold fluence for Cu is 1.46 J/cm^2 [111], which is ~6 times larger than our result. The threshold is also smaller than 0.49 J/cm^2 obtained using a 150 fs Ti:Sapphire chirped-pulse amplifier [116] or 0.5 J/cm^2 obtained using a 35 fs Ti:sapphire amplifier in our lab [129].

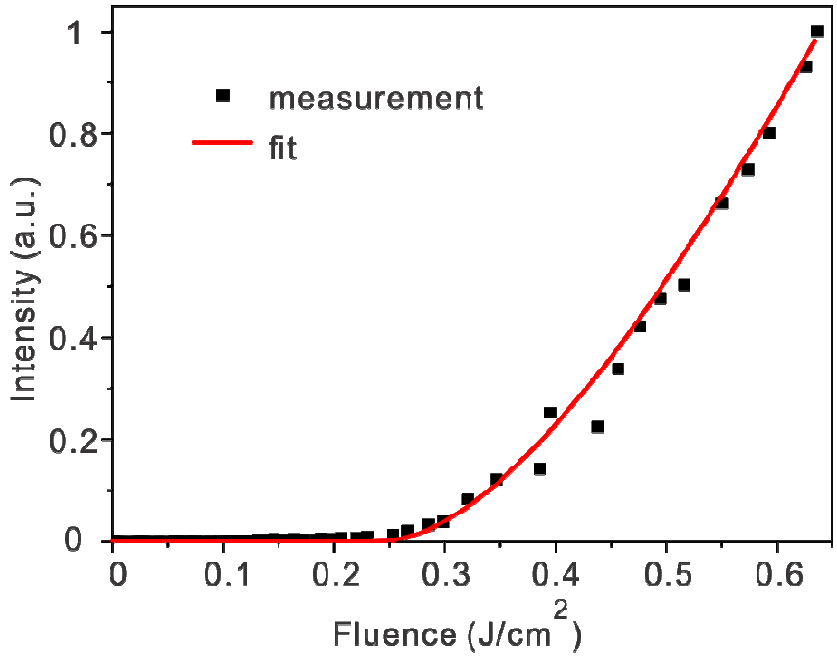

Figure 82: Threshold measurement. LIBS intensity for copper as a function of incident laser fluence.

Lower threshold implies less pulse energy required for LIBS, which results in a lower background plasma emission. Plasma emission can mask the LIBS signal and eliminating it

typically requires a time-gated spectrometer. As discussed above, the threshold measured from our laser is lower than the results of both nanosecond and femtosecond lasers. The observed lower ablation threshold, compared to that of single fs pulses, is probably due to the multiple femtosecond sub-pulses as indicated by reference [15]. The lower threshold and high repetition-rate of our laser source results in significant improvements in the efficiency and signal-to-noise ratio of LIBS spectra. Current portable LIBS systems typically use Q-switched nanosecond fiber lasers [113-115]. The laser presented here can be developed as an ideal source for a portable LIBS system.

4.5 Conclusion

We have built several noise-like fiber lasers by using more than 100 m of fiber inside a laser cavity. By varying intra-cavity spectral-filter bandwidth, laser performance is studied and the filter does not play as important a role as in similariton fiber lasers. By removing the spectral filter, broader output spectra are achieved and output pulses with 320 nJ pulse energy are delivered at 2 MHz repetition rate. These pulses are more than 100 ps long and contain irregular multiple femtosecond sub-pulses. It is found that these pulses meet the requirements of an ideal laser source for LIBS. A simple LIBS system has been built using this laser. Strong LIBS signals have been generated with low fluence threshold and insignificant continuum background. The system has also been tested to detect the change of atomic concentration in alloys and track trace contaminant. These results have shown that this laser will be an ideal source for a low-cost and portable LIBS system.

The pulse energy of this laser has been scaled up to 450 nJ at 1 MHz repetition rate by extending the cavity fiber length to about 200 m. A fiber amplifier has also been built to further increase the pulse energy to 3.87 μJ at 1 MHz repetition rate.

Chapter 5 Summary and Outlook

This chapter summarizes the work and results presented through this thesis. My work includes the development of similariton fiber lasers and noise-like fiber lasers and some applications using these developed lasers. Future directions of our work are discussed at the end.

5.1 Similariton fiber laser and applications

We have developed ultrafast fiber lasers based on all-normal dispersion cavity design. Pulses with up to 34 nJ pulse energy and 80 fs pulse duration are delivered from one of our regular all-normal dispersion fiber lasers. Fiber length and intra-cavity spectral-filter bandwidth are found to be the most important parameters affecting laser performance. A very narrow bandwidth intra-cavity spectral filter is used as an attractor for similariton pulse formation, which is a solution characterized by a wave-breaking-free form in normal dispersion fiber. With a 3 nm spectral filter, output pulses with about 20 nJ pulse energy are delivered and compressed to about 41 fs FWHM pulse duration using a MIIPS-enabled pulse shaper. Numerical simulations are conducted to verify the formation of similaritons and match the experimental results very well.

The similariton fiber laser has been successfully demonstrated for multiphoton microscopy. The ultrashort pulse durations greatly enhance two- and three-photon induced modalities in both stained and unstained living tissues such as Drosophila larvae and fruit fly wings. Results of SHG and THG from living tissue are compared under similar laser conditions and complementary results show the full information of living tissue structures. Due to the high pulse energy, depth-resolved imaging of Drosophila larva and fruit fly eyes is also achieved. Three-dimensional constructed imaging based on THG shows much better contrast in resolving the tissue structures than SHG. It shows that this high pulse energy ultrafast similariton fiber laser is a suitable source for deep tissue imaging.

5.2 Noise-like fiber laser and applications

Also based on all-normal fiber laser cavity design, another type of laser has been developed for laser-induced breakdown spectroscopy (LIBS). This laser is operated in an unusual mode-locking regime and produces noise-like pulses, which have mostly been ignored by many researchers. However, we have found that some characteristics of our noise-like laser, such as broad spectra and picosecond long pulse envelope containing multiple femtosecond sub-pulses, meet the requirements of an ideal laser source for LIBS. We have built a noise-like fiber laser using ~200 m long fiber and scaled the output pulse energy up to 450 nJ at 1 MHz repetition rate. The spectral filter does not affect the laser performance as much as in the similariton lasers and can be removed from the laser cavity. Due to its phase insensitivity, external pulse shaping is not necessary for this type of pulses in applications.

A simple LIBS setup using this noise-like laser has been demonstrated on several samples. Atomic emission spectra with very good signal-to-noise ratio have been obtained. Abilities, such as analyzing atomic composition, qualitatively detecting concentration changes and tracking trace compounds, have also been tested. The results show that our noise-like fiber laser is an ideal laser source for a low-cost and portable LIBS system.

5.3 Future work

To further improve the pulse energy of a similariton laser while still producing equally short pulse durations, one option is to use LMA fibers. In principle, with the same cavity design, the maximum output pulse energy delivered is proportional to the square of the fiber core diameter. Currently available single mode LMA fibers are mainly photonic crystal fibers and chirally coupled core fibers. Their core diameter is normally more than 30 μm, which can scale the pulse energy up to 100 nJ. However, these LMA fibers are not as flexible as standard single

mode fibers and may suffer large losses from bending. The other drawback is that special fiber splicing technology is required for them. The other option to scale up the pulse energy is to use multiple-stage amplification. This is the most commonly used method for higher-energy industrial fiber lasers. In terms of pulse duration, specially designed dispersion-decreasing fiber can be used to sustain the similariton evolution after the gain fiber and further broaden the output spectrum. Basically, new fiber technology is highly desirable for the development of fiber lasers.

For the noise-like fiber lasers, the limit of pulse energy should be further studied using even longer fiber. It is also important to experimentally measure the profile of single short pulses and understand the detailed structure of the sub-pulses. We have tried cross correlation using another highly chirped broadband laser source but could not get it to work. New measurement method is required.

To eliminate all the free-space components in our current fiber laser and modify them to an integrated all-fiber system will also be desirable for future applications.

APPENDICES

Appendix-I Matlab Code

1. Pulse propagation in fibers with second order and third order dispersion

```
%% define basic parameters
T = 1000; % time window, in femtosecond
nt = 2^12; % sampling points
dt = T/nt; % time resolution
t = (-nt/2:1:nt/2-1)'*dt; % time vector
v = (-nt/2:1:nt/2-1)'/(dt*nt); % frequency vector
w = 2*pi*(-nt/2:1:nt/2-1)'/(dt*nt); % angular frequency
dw = w(2)-w(1); % angular frequency resolution
lambda = 2*pi*3e2./(w+2*pi*3e2/1050); % wavelength, in nonometer
lambda(lambda<0)=nan;
c = 3*10^8; % speed of light, m/s
w0 = 2*pi*c/1050*10^9; % carrier frequency
beta2 = 23000; % GVD, fs^2/m
beta3 = 0.1e6; % Third order dispersion, fs^3/m
tau = 50; % FWHM pulse duration of input pulse, fs
tau0 = tau/2/log(2)^0.5; % 1/e^2 pulse duration
Ld = tau0^2/abs(beta2); % second order dispersion length
Ld3 = tau0^3/abs(beta3); % third order dispersion length
u0 = exp(-t.^2/2/tau0^2); % input intensity field
uw = fftshift(ifft(fftshift(u0)))*dt; % FFT of temporal field to frequency
filed
dispersion1 = exp(1i*beta2/2.*w.^2*3*Ld); % phase distortion
dispersion2 = exp(1i*beta3/6.*w.^3*3*Ld3); % phase distortion
uw1 = uw.*dispersion1;
uw2 = uw.*dispersion2;
uw3 = uw.*dispersion1.*dispersion2;
u1 = fftshift(fft(fftshift(uw1)))*1/dt;
u2 = fftshift(fft(fftshift(uw2)))*1/dt;
u3 = fftshift(fft(fftshift(uw3)))*1/dt;

%% make plots
ha=tight_subplot(2,4,[.1 .01]);
axes(ha(1));
plot(t,abs(u0).^2,'linewidth',2);
ylim([0 1]);
xlim([-500 500]);
set(gca,'xTick',-500:250:500,'xticklabel',[],'yticklabel',[]) ;
axes(ha(2));
plot(t,abs(u1).^2,'linewidth',2);
ylim([0 1]);
xlim([-500 500]);
set(gca,'xTick',-500:250:500,'xticklabel',[],'yticklabel',[]) ;

axes(ha(3));
plot(t,abs(u2).^2,'linewidth',2);
ylim([0 1]);
xlim([-500 500]);
set(gca,'xTick',-500:250:500,'xticklabel',[],'yticklabel',[]) ;
axes(ha(4));
plot(t,abs(u3).^2,'linewidth',2);
ylim([0 1]);
```

```
xlim([-500 500]);
set(gca,'xTick',-500:250:500,'xticklabel',[],'yticklabel',[]) ;
axes(ha(5));
plot(lambda,abs(uw).^2/max(abs(uw).^2),'linewidth',2);
ylim([0 1]);
xlim([950 1150]);
set(gca,'xTick',950:50:1150,'xticklabel',[],'yticklabel',[]) ;
axes(ha(6));
plot(lambda,abs(uw1).^2/max(abs(uw1).^2),'linewidth',2);
ylim([0 1]);
xlim([950 1150]);
set(gca,'xTick',950:50:1150,'xticklabel',[],'yticklabel',[]) ;
axes(ha(7));
plot(lambda,abs(uw2).^2/max(abs(uw2).^2),'linewidth',2);
ylim([0 1]);
xlim([950 1150]);
set(gca,'xTick',950:50:1150,'xticklabel',[],'yticklabel',[]) ;
axes(ha(8));
plot(lambda,abs(uw3).^2/max(abs(uw3).^2),'linewidth',2);
ylim([0 1]);
xlim([950 1150]);
set(gca,'xTick',950:50:1150,'xticklabel',[],'yticklabel',[]) ;
```

2. Pulse propagation in fibers with nonlinear coefficient

```
T=1000; %fs
nt=2^12;
dt=T/nt;                                % timestep (dt)
t=(-nt/2:1:nt/2-1)'*dt;                % time vector
v=(-nt/2:1:nt/2-1)'/(dt*nt);
w=2*pi*(-nt/2:1:nt/2-1)'/(dt*nt);
dw=w(2)-w(1);
lambda=2*pi*3e2./(w+2*pi*3e2/1050);
lambda(lambda<0)=nan;
lambda2w=2*pi*3e2./(w+2*pi*3e2/1050*2);
c=3*10^8;%m/s
w0=2*pi*c/1050*10^9;
beta2=23000;
tau=50;
tau0=tau/2/log(2)^0.5;
Ld=tau0^2/abs(beta2);
beta3=0.1e6;
Ld3=tau0^3/abs(beta3);
I0=1e11;
u0=exp(-t.^2/2/tau0^2);
uw=fftshift(ifft(fftshift(u0)))*dt;
n2=2.6*10^-16;%cm^2/W
%%%gamma=n2*w0/c/Aeff;
Lnl=1/(0.0044*I0);
L=Lnl;
nstep=100;
h=L/nstep;
u=u0;
for i=1:1:nstep
    u=u.*exp(1i*abs(u).^2*h/Lnl);
end
```

```
uw1=fftshift(ifft(fftshift(u)))*dt;

ha=tight_subplot(2,2,[.01 .02]);
axes(ha(1))
plot(lambda,abs(uw).^2/max(abs(uw).^2),'-k','linewidth',2);
xlim([950 1150]);
ylim([0 1]);
set(gca,'xTick',950:50:1150,'xticklabel',[],'yticklabel',[]) ;
axes(ha(2))
plot(t,abs(u0).^2/max(abs(u0).^2),'-k','linewidth',2);
xlim([-100 100]);
set(gca,'xTick',-100:50:100,'xticklabel',[],'yticklabel',[]) ;
ylim([0 1]);
hold on;
plot(t,[-diff(phase(u0))/dw;0],'-r','linewidth',2)
ylim([-1.1 1.1]);
hold on;
plot(t,0,'-k')
axes(ha(3))
plot(lambda,abs(uw1).^2/max(abs(uw).^2),'-k','linewidth',2);
xlim([950 1150]);
% ylim([0 1]);
set(gca,'xTick',950:50:1150,'xticklabel',[],'yticklabel',[]) ;
axes(ha(4))
% [haxes,hline1,hline2] =
plotyy(t,abs(u).^2/max(abs(u).^2),t,[diff(phase(u))/dw;0])
plot(t,abs(u).^2/max(abs(u).^2),'-k','linewidth',2);
xlim([-100 100]);
set(gca,'xTick',-100:50:100,'xticklabel',[],'yticklabel',[]) ;
ylim([-1.1 1.1]);
hold on;
plot(t,[-diff(phase(u))/dt*tau0;0],'-r','linewidth',2)
ylim([-1.1 1.1]);
hold on;
plot(t,0,'-k')
```

3. Pulse propagation in fibers with second order dispersion and nonlinear coefficient

```
T=1000; %fs
nt=2^12;
dt=T/nt;                                % timestep (dt)
t=(-nt/2:1:nt/2-1)'*dt;                % time vector
v=(-nt/2:1:nt/2-1)'/(dt*nt);
w=2*pi*(-nt/2:1:nt/2-1)'/(dt*nt);
dw=w(2)-w(1);
lambda=2*pi*3e2./(w+2*pi*3e2/1050);
lambda(lambda<0)=nan;
lambda2w=2*pi*3e2./(w+2*pi*3e2/1050*2);
c=3*10^8;%m/s
w0=2*pi*c/1050*10^9;
beta2=23000;
tau=50;
tau0=tau/2/log(2)^0.5;
Ld=tau0^2/abs(beta2);
beta3=0.1e6;
Ld3=tau0^3/abs(beta3);
```

```
I0=1e11;
u0=exp(-t.^2/2/tau0^2);
uw=fftshift(ifft(fftshift(u0)))*dt;
n2=2.6*10^-16;%cm^2/W
%%%gamma=n2*w0/c/Aeff;
Lnl=1/(0.0044*I0);
L=pi*Lnl;
nstep=100;
h=L/nstep;
u=u0;
for i=1:1:nstep
    u=u.*exp(1i*abs(u).^2*h/Lnl);
end
uw1=fftshift(ifft(fftshift(u)))*dt;
Lnl=1/(0.0044*I0);
L=3.5*pi*Lnl;
nstep=100;
h=L/nstep;
u=u0;
for i=1:1:nstep
    u=u.*exp(1i*abs(u).^2*h/Lnl);
end
uw2=fftshift(ifft(fftshift(u)))*dt;
ha=tight_subplot(1,3,0.02);
axes(ha(1))
plot(lambda,abs(uw).^2/max(abs(uw).^2),'-k','linewidth',2);
xlim([750 1550]);
ylim([0 1.1]);
set(gca,'xTick',750:200:1550,'xticklabel',[],'yticklabel',[]) ;
axes(ha(2))
plot(lambda,abs(uw1).^2/max(abs(uw).^2),'-k','linewidth',2);
xlim([750 1550]);
% ylim([0 1]);
set(gca,'xTick',750:200:1550,'xticklabel',[],'yticklabel',[]) ;
axes(ha(3))
plot(lambda,abs(uw2).^2/max(abs(uw).^2),'-k','linewidth',2);
xlim([750 1550]);
ylim([0 0.17]);
set(gca,'xTick',750:200:1550,'xticklabel',[],'yticklabel',[]) ;
```

4. Wave-breaking pulse simualtion

```
T=1000; %fs
nt=2^12;
dt=T/nt;                                % timestep (dt)
t=(-nt/2:1:nt/2-1)'*dt;                % time vector
v=(-nt/2:1:nt/2-1)'/(dt*nt);
w=2*pi*(-nt/2:1:nt/2-1)'/(dt*nt);
dw=w(2)-w(1);
lambda=2*pi*3e2./(w+2*pi*3e2/1050);
lambda(lambda<0)=nan;
lambda2w=2*pi*3e2./(w+2*pi*3e2/1050*2);
c=3*10^8;%m/s
w0=2*pi*c/1050*10^9;
beta2=23000;
```

```
tau=50;
tau0=tau/2/log(2)^0.5;
Ld=tau0^2/abs(beta2);
u0=exp(-1/2*(t/tau0).^2);
Lnl=Ld/30^2;
ha=tight_subplot(3,2,[.01 .02]);
L=0.01*Ld;
a=length(L);
nstep=100;
h=L/nstep;
halfstep=exp(1i*1/2*beta2*w.^2*h/2);
u=fftshift(ifft(fftshift(u0)))*dt;
spec0=abs(u).^2;
u=u*ones(1,a);
for i=1:1:nstep
    u=u.*halfstep;
    u=fftshift(fft(fftshift(u)))*1/dt;
    u=u.*exp(1i/Lnl*abs(u).^2*h);
    u=fftshift(ifft(fftshift(u)))*dt;
    u=u.*halfstep;
end
axes(ha(1))
spec=abs(u).^2/max(spec0);
plot(v*tau0,spec,'-k','linewidth',2);
xlim([-10 10]);
ylim([0 0.2]);
set(gca,'xticklabel',[],'yticklabel',[]) ;
axes(ha(2))
u=fftshift(fft(fftshift(u)))*1/dt;
int=abs(u).^2;
plot(t/tau0,int,'-k','linewidth',2);
xlim([-4.5 4.5]);
ylim([0 1]);
set(gca,'xticklabel',[],'yticklabel',[]) ;
hold on;
plot(t/tau0,[-diff(phase(u))/dt/0.6+0.5;0],'-r','linewidth',2)
ylim([0 1]);
xlim([-4.5 4.5]);
L=0.04*Ld;
a=length(L);
nstep=100;
h=L/nstep;
halfstep=exp(1i*1/2*beta2*w.^2*h/2);
u=fftshift(ifft(fftshift(u0)))*dt;
spec0=abs(u).^2;
u=u*ones(1,a);
for i=1:1:nstep
    u=u.*halfstep;
    u=fftshift(fft(fftshift(u)))*1/dt;
    u=u.*exp(1i/Lnl*abs(u).^2*h);
    u=fftshift(ifft(fftshift(u)))*dt;
    u=u.*halfstep;
end
```

```
axes(ha(3));
spec=abs(u).^2/max(spec0);
plot(v*tau0,spec,'-k','linewidth',2);
xlim([-10 10]);
ylim([0 0.07]);
set(gca,'xticklabel',[],'yticklabel',[]) ;
axes(ha(4))
u=fftshift(fft(fftshift(u)))*1/dt;
int=abs(u).^2;
plot(t/tau0,int,'-k','linewidth',2);
xlim([-4.5 4.5]);
ylim([0 0.6]);
set(gca,'xticklabel',[],'yticklabel',[]) ;
hold on;
plot(t/tau0,[-diff(phase(u))/dt/3+0.3;0],'-r','linewidth',2)
ylim([0 0.6]);
xlim([-4.5 4.5]);
L=0.08*Ld;
a=length(L);
nstep=100;
h=L/nstep;
halfstep=exp(1i*1/2*beta2*w.^2*h/2);
u=fftshift(ifft(fftshift(u0)))*dt;
spec0=abs(u).^2;
u=u*ones(1,a);
for i=1:1:nstep
    u=u.*halfstep;
    u=fftshift(fft(fftshift(u)))*1/dt;
    u=u.*exp(1i/Lnl*abs(u).^2*h);
    u=fftshift(ifft(fftshift(u)))*dt;
    u=u.*halfstep;
end
axes(ha(5));
spec=abs(u).^2/max(spec0);
plot(v*tau0,spec,'-k','linewidth',2);
xlim([-10 10]);
ylim([0 0.04]);
set(gca,'xticklabel',[],'yticklabel',[]) ;
axes(ha(6))
u=fftshift(fft(fftshift(u)))*1/dt;
int=abs(u).^2;
plot(t/tau0,int,'-k','linewidth',2);
xlim([-4.5 4.5]);
ylim([0 0.4]);
set(gca,'xticklabel',[],'yticklabel',[]) ;
hold on;
plot(t/tau0,[-diff(phase(u))/dt/15+0.15;0],'-r','linewidth',2)
ylim([0 0.35]);
xlim([-4.5 4.5]);
```

5. Fiber laser simulation

5.1 Pulse propagation function

```
function uout=prop(u0,g0,gamma,beta2,beta3,L,alpha,T,nt,Esat,lambda0)
if L<0.01
```

```
    h=0.001;
else
    h=0.02;
end
nz=L/h;
u=fftshift(fft(ifftshift(u0)));
% halfstep=exp((gain-alpha).*(h/2)-1i*beta2/2*w.^2*(h/2));
for n=1:1:nz
dt = T/nt;                                  % timestep (dt)
w = 2*pi*(-nt/2:1:nt/2-1)'./(dt*nt);
% w=fftshift(w);
% Esat=1500; %pJ
% Esat=2100;%38nJ saturation gain energy used in Simon's CCC fiber laser%
ue=fftshift(ifft(ifftshift(u)));
Ei=(abs(ue).^2)*dt*10^-3;
E0=sum(Ei);
% Tr=(4.3+0.5)/(3*10^8/1.458)*10^15;
% E0=E0*Tr/T;
bw=50;%nm
BW=(2*pi*3*10^8)/(lambda0-bw/2)/(lambda0+bw/2)*bw*10^-6;%gain bandwith
corresponding to the frequency
% if E0<Esat
gain=g0./(1+E0/Esat+((w+2*pi/2/T)./BW).^2);
% else gain=g0./(2+(w./BW).^2);
% end
% plot(w,gain)
halfstep=exp((gain-
alpha).*(h/2)+1i*beta2./2.*(w.^2)*(h/2))+1i*beta3/6*(w.^3)*(h/2);
u=halfstep.*u;
u=fftshift(ifft(ifftshift(u)));
u=u.*exp(1i*gamma*((abs(u)).^2)*(h));
u=fftshift(fft(ifftshift(u)));
u=halfstep.*u;
end
uout=fftshift(ifft(ifftshift(u)));
```

5.2 Laser cavity function

```
folder='';
mkdir(folder);
% prameters for fourier transforms
T=50000; %fs
nt=2^11;
dt = T/nt                                   % timestep (dt)
t = (-nt/2:1:nt/2-1)'*dt;                   % time vector
w = 2*pi*(-nt/2:1:nt/2-1)'/(dt*nt);
% vs=w./2/pi;
lambda0=1070;
w0=2*pi*3e2/lambda0;
w1=w+w0;
lambda=2*pi*3e2./w1;
lambda_min=max(lambda)
lambda_max=min(lambda)
DATA=rand(1,5);
g0=3.45;
beta3=0;
```

```
Esat=5000;%gain saturation energy, in pJ
L_gain=2.5;
gamma_10um=0.001584;
%setting the maximum value of
L_GVD_max=1.7;
bw_max=1.5;
Esat_max=200;

for nm=1:1:1000
    Esat=Esat+100
    bw=2.5;
for j=1:1:1000
    bw=bw+0.5
    L_GVD=1.2;
    count_L_GVD=0
    for m=1:1:1000
        L_GVD=L_GVD+0.5
%--%initial pulse%--%
% u0 = sqrt(p0)*exp(-((1+1i*C)/2)*((t-t0)/T0).^(2*m));%initial pulse
u0=wgn(nt,1,-40,'complex');
% u0=fftshift(fft(ifftshift(u0)));
% int_u0=abs(u0).^2;
% plot(t,int_u0);
% ylim([-0.1 1])
% spec_u0 = fftshift(abs(dt*fft(ifftshift(u0))/sqrt(2*pi)).^2);
% plot(lambda,spec_u0);
% xlim([960 1100]);
% ylim([-0.1 1]);

iteration=100;

for n=1:iteration
%--%the first segment of passive fiber%--%
%prameters for fiber
gamma1=gamma_10um;
beta2_1=23*10^3;
beta3;
% gamma1=0;
alpha1=0;
g1=0;
L1=L_GVD;
%pulse after propagating through the passive fiber
u1=prop(u0,g1,gamma1,beta2_1,beta3,L1,alpha1,T,nt,Esat,lambda0);
% spec1=fftshift(abs(dt*fft(ifftshift(u1)))/sqrt(2*pi).^2);
% spec1=spec1./max(spec1);%normalized spectrum
% int1=abs(u1).^2;

%--%segment of gain fiber%--%
% prameters for gain fiber
gamma=gamma_10um; %(W*m)^-1
% gamma=0;
% beta2=0;
beta2=23*10^3; %fs^2/m, 23 fs^2/mm
beta3;
alpha=0;
```

```
g0; %small signal gain corresponding to a ~30dB fiber amplifier,
30dB/10*ln10=6.9, then since the energy is square of power, so it is divided
by to get 3.45

% FWHM=rand(1,100);
% for i=1:1:100
%     L_gain=i*0.02;
L_g=L_gain;
%pulse after propagating through the gain fiber
u_gain=prop(u1,g0,gamma,beta2,beta3,L_g,alpha,T,nt,Esat,lambda0);
% spec_gain =
fftshift(abs(dt*fft(ifftshift(u_gain))/sqrt(2*pi)).^2);%spectrum
% spec_gain=spec_gain./max(spec_gain);%normalized spectrum
% int_gain=abs(u_gain).^2;


%--%the second segment of passive fiber%--%
%prameters for passive fiber
% gamma2=gamma_10um;
gamma2=gamma_10um;
beta2_2=23*10^3;
beta3;
alpha2=0;
g2=0;
L2=1;
%pulse after propagating through the passive fiber
u2=prop(u_gain,g2,gamma2,beta2_2,beta3,L2,alpha2,T,nt,Esat,lambda0);
% spec2=fftshift(abs(dt*fft(ifftshift(u2))/sqrt(2*pi)).^2);
% spec2=spec2./max(spec2);%normalized spectrum
int2=abs(u2).^2;

%%%saturable absorber%%%
SA=1-1./(1+int2./max(int2));
u_sa=u2.*(SA.^0.5);

%%%spectral filter%%%
bw;%nm
BW=(2*pi*3e2)/(lambda0-bw/2)/(lambda0+bw/2)*bw/2/((2*log(2))^0.5);%spectral
filter bandwidth
SF=exp(-1/2*(w/BW).^2);%setting up spectral filter
u_sa=fftshift(fft(ifftshift(u_sa)));
u_sf=u_sa.*(SF).^0.5;
u_sf=fftshift(ifft(ifftshift(u_sf)));
u_sf=(0.2^0.5)*u_sf;
% int_sf=abs(u_sf).^2;
% spec_sf = fftshift(abs(dt*fft(ifftshift(u_sf))/sqrt(2*pi)).^2);

% u0=(0.2^0.5)*u_sf;
u0=u_sf;
end

%%input for the last run of cavity%%
int0=abs(u0).^2;
spec0=fftshift(abs(dt*fft(ifftshift(u0))/sqrt(2*pi)).^2);
% spec0=spec0./max(spec0);
```

```
%%fwhm of pulse%%
fwhm_t=find(int0>(max(int0)/2));
fwhm_t=t(max(fwhm_t))-t(min(fwhm_t));
FWHM_t=fwhm_t;
% %%fwhm of spectrum%%
fwhm_f=find(spec0>(max(spec0)/2));
fwhm_f=lambda(min(fwhm_f))-lambda(max(fwhm_f));
FWHM_f=fwhm_f;
spec_2d=spec0;%initiate the 2D spec database

%%plot the evolution of pulse duration and sepctrum bandwidth%%
%--%the first segment of passive fiber%--%
%prameters for fiber
gamma1=gamma_10um;
beta2_1=23*10^3;
beta3;
alpha1=0;
g1=0;
% L1=1.5;
%pulse after propagating through the passive fiber
for L1=0.05:0.05:L_GVD
u1=prop(u0,g1,gamma1,beta2_1,beta3,L1,alpha1,T,nt,Esat,lambda0);
spec1=fftshift(abs(dt*fft(ifftshift(u1))/sqrt(2*pi)).^2);
int1=abs(u1).^2;
%%fwhm of pulse%%
fwhm_t=find(int1>(max(int1)/2));
fwhm_t=t(max(fwhm_t))-t(min(fwhm_t));
FWHM_t=horzcat(FWHM_t,fwhm_t);
% %%fwhm of spectrum%%
fwhm_f=find(spec1>(max(spec1)/2));
% fwhm_f=3e2*2*3.14./(w(min(fwhm_f))+2*3.14*3/1060*1e2)-
3e2*2*3.14./(w(max(fwhm_f))+2*3.14*3/1060*1e2);
fwhm_f=lambda(min(fwhm_f))-lambda(max(fwhm_f));
FWHM_f=horzcat(FWHM_f,fwhm_f);
spec_2d=horzcat(spec_2d,spec1);%save the spectrum for each position withou
normalization
spec1=spec1./max(spec1);%normalized spectrum
end

%--%segment of gain fiber%--%
% prameters for gain fiber
gamma=gamma_10um; %(W*m)^-1
% gamma=0;
% beta2=0;
beta2=23*10^3; %fs^2/m, 23 fs^2/mm
beta3;
alpha=0;
g0; %small signal gain corresponding to a ~30dB fiber amplifier

for L_g=0.05:0.05:L_gain;
%pulse after propagating through the gain fiber
u_gain=prop(u1,g0,gamma,beta2,beta3,L_g,alpha,T,nt,Esat,lambda0);
spec_gain = fftshift(abs(dt*fft(ifftshift(u_gain))/sqrt(2*pi)).^2);%spectrum
int_gain=abs(u_gain).^2;
%%fwhm of pulse%%
fwhm_t=find(int_gain>(max(int_gain)/2));
```

```
fwhm_t=t(max(fwhm_t))-t(min(fwhm_t));
FWHM_t=horzcat(FWHM_t,fwhm_t);
% %%fwhm of spectrum%%
fwhm_f=find(spec_gain>(max(spec_gain)/2));
% fwhm_f=3e2*2*3.14./(w(min(fwhm_f))+2*3.14*3/1060*1e2)-
3e2*2*3.14./(w(max(fwhm_f))+2*3.14*3/1060*1e2);
fwhm_f=lambda(min(fwhm_f))-lambda(max(fwhm_f));
FWHM_f=horzcat(FWHM_f,fwhm_f);
spec_2d=horzcat(spec_2d,spec_gain);%save spectrum to the 2d database
spec_gain=spec_gain./max(spec_gain);%normalized spectrum
end


%--%the second segment of passive fiber%--%
%prameters for passive fiber
% gamma2=gamma_10um;
gamma2=gamma_10um;
beta2_2=23*10^3;
beta3;
alpha2=0;
g2=0;
for L2=0.05:0.05:1;
%pulse after propagating through the passive fiber
u2=prop(u_gain,g2,gamma2,beta2_2,beta3,L2,alpha2,T,nt,Esat,lambda0);
spec2=fftshift(abs(dt*fft(ifftshift(u2))/sqrt(2*pi)).^2);
int2=abs(u2).^2;
%%fwhm of pulse%%
fwhm_t=find(int2>(max(int2)/2));
fwhm_t=t(max(fwhm_t))-t(min(fwhm_t));
FWHM_t=horzcat(FWHM_t,fwhm_t);
% %%fwhm of spectrum%%
fwhm_f=find(spec2>(max(spec2)/2));
% fwhm_f=3e2*2*3.14./(w(min(fwhm_f))+2*3.14*3/1060*1e2)-
3e2*2*3.14./(w(max(fwhm_f))+2*3.14*3/1060*1e2);
fwhm_f=lambda(min(fwhm_f))-lambda(max(fwhm_f));
FWHM_f=horzcat(FWHM_f,fwhm_f);
spec_2d=horzcat(spec_2d,spec2);
spec2=spec2./max(spec2);%normalized spectrum
end

u2_w=fftshift(fft(ifftshift(u2)));
phi=log(u2_w./abs(u2_w))*(-1i);
phi=real(phi);
phi=unwrap(phi);
plot(lambda,phi);
phase=[w,phi];
phase_filename=[folder,'phase.dat'];
saveascii(phase,phase_filename);

Etot=(abs(u2).^2)*dt*10^-3;
Etot=sum(Etot)

%%%saturable absorber%%%
SA=1-1./(1+int_gain./max(int_gain));
u_sa=u2.*(SA.^0.5);
int_sa=abs(u_sa).^2;
```

```
Ei=(abs(u_sa).^2)*dt*10^-3;
E0=sum(Ei)
Eout=Etot-E0
spec_sa=fftshift(abs(dt*fft(ifftshift(u_sa))/sqrt(2*pi)).^2);
%%fwhm of pulse%%
fwhm_t=find(int_sa>(max(int_sa)/2));
fwhm_t=t(max(fwhm_t))-t(min(fwhm_t));
FWHM_t=horzcat(FWHM_t,fwhm_t);
% %%fwhm of spectrum%%
fwhm_f=find(spec_sa>(max(spec_sa)/2));
% fwhm_f=3e2*2*3.14./(w(min(fwhm_f))+2*3.14*3/1060*1e2)-
3e2*2*3.14./(w(max(fwhm_f))+2*3.14*3/1060*1e2);
fwhm_f=lambda(min(fwhm_f))-lambda(max(fwhm_f));
FWHM_f=horzcat(FWHM_f,fwhm_f);
spec_2d=horzcat(spec_2d,spec_sa);
spec_sa=spec_sa./max(spec_sa);

%%%spectral filter%%%
bw;%nm
BW=(2*pi*3e2)/(lambda0-bw/2)/(lambda0+bw/2)*bw/2/((2*log(2))^0.5);%spectral
filter bandwidth
SF=exp(-1/2*(w/BW).^2);%setting up spectral filter

u_sa=fftshift(fft(ifftshift(u_sa)));
u_sf=u_sa.*(SF).^0.5;
u_sf=fftshift(ifft(ifftshift(u_sf)));
u_sf=(0.2^0.5)*u_sf;
int_sf=abs(u_sf).^2;
spec_sf = fftshift(abs(dt*fft(ifftshift(u_sf))/sqrt(2*pi)).^2);
%%fwhm of pulse%%
fwhm_t=find(int_sf>(max(int_sf)/2));
fwhm_t=t(max(fwhm_t))-t(min(fwhm_t));
FWHM_t=horzcat(FWHM_t,fwhm_t);
% %%fwhm of spectrum%%
fwhm_f=find(spec_sf>=(max(spec_sf)/2));
% fwhm_f=3e2*2*3.14./(w(min(fwhm_f))+2*3.14*3/1060*1e2)-
3e2*2*3.14./(w(max(fwhm_f))+2*3.14*3/1060*1e2);
fwhm_f=lambda(min(fwhm_f))-lambda(max(fwhm_f));
FWHM_f=horzcat(FWHM_f,fwhm_f);
spec_2d=horzcat(spec_2d,spec_sf);
spec_sf=spec_sf./max(spec_sf);%normalized spectrum

%%final fwhm bandwidth and pulse duration%%
% FWHM_t=FWHM_t(1:1,2:length(FWHM_t));
% FWHM_f=FWHM_f(1:1,2:length(FWHM_f));

u0=u_sf;

%configure filename for saving data%
% folder='E:\RESEARCH\Dantus Group\FiberLaser\simulation\051311\';
filename=strcat('Esat',num2str(Esat),'pJ_','bw',num2str(bw),'nm_Lgvd',num2str
(L_GVD),'m_Eout',num2str(Eout),'pJ_Lgain_',num2str(L_gain),'m_');
spec1_file=strcat(folder,filename,'Spec1.dat');
int1_file=strcat(folder,filename,'Int1.dat');
spec_gain_file=strcat(folder,filename,'SpecGain.dat');
int_gain_file=strcat(folder,filename,'IntGain.dat');
```

```
spec2_file=strcat(folder,filename,'Spec2.dat');
int2_file=strcat(folder,filename,'Int2.dat');
spec_sf_file=strcat(folder,filename,'SpecSF.dat');
int_sf_file=strcat(folder,filename,'IntSF.dat');
FWHM_f_file=strcat(folder,filename,'FWHMf.dat');
FWHM_t_file=strcat(folder,filename,'FWHMt.dat');
figure1=strcat(folder,filename,'PulseEvolution.png');
figure2=strcat(folder,filename,'FWHM.png');
spec_2d_file=strcat(folder,filename,'spec_2d.data');


%check whether it is multi-pulsing for the loop using variable GVD segment
%length
delta=max(int2);
delta=delta*0.1;
peaks=peakdet(int2,delta);
[pix val]=size(peaks);
if pix>1
% if max(FWHM_t)>12000
    count_L_GVD=count_L_GVD+1
    if count_L_GVD>10
        %to check whether this length of GVD segment is not quite possible
        %to get stable single pulsing, the tolerance is 10 cycles, if it is
        %over 10, then just continute to the next length of GVD segment
        L_GVD;
        strcat('first segment of ',num2str(L_GVD),'m is a not stable
solution')
        count_L_GVD=0;

        data=[Esat bw L_GVD Eout 0];
        DATA=vertcat(DATA,data);

        figure(1);
        subplot(421);
        plot(lambda,spec1);
        xlim([900 1200]);
        title('1st SMF-spectrum');
%         xlim([950 1160]);
        ylim([-0.05 1.05]);
        subplot(422);
        plot(t,int1);
        title('1st SMF-time');
        spec1=horzcat(lambda,spec1);
        int1=horzcat(t,int1);
        saveascii(spec1,spec1_file);
        saveascii(int1,int1_file);
        subplot(423);
        plot(lambda,spec_gain);
        xlim([900 1200]);
        title('gain-spectrum');
%         xlim([1000 1120]);
        ylim([-0.05 1.05]);
        subplot(424);
        plot(t,int_gain);
        title('gain-time');
        spec_gain=horzcat(lambda,spec_gain);
```

```
        int_gain=horzcat(t,int_gain);
        saveascii(spec_gain,spec_gain_file);
        saveascii(int_gain,int_gain_file);
        subplot(425);
        plot(lambda,spec2);
        xlim([900 1200]);
        title('2nd SMF-spectrum');
%         xlim([1000 1120]);
        ylim([-0.05 1.05]);
        subplot(426);
        plot(t,int2);
        title('2nd SMF-time');
        spec2=horzcat(lambda,spec2);
        int2=horzcat(t,int2);
        saveascii(spec2,spec2_file);
        saveascii(int2,int2_file);
        subplot(427);
        plot(lambda,spec_sf);
        xlim([900 1200]);
        title('Spectral Filter-spectrum');
%         xlim([1000 1120]);
        ylim([-0.05 1.05]);
        xlabel('wavelength(nm)');
        subplot(428);
        plot(t,int_sf);
        title('Spectral Filter-time');
        xlabel('time(fs)');
        spec_sf=horzcat(lambda,spec_sf);
        int_sf=horzcat(t,int_sf);
        saveascii(spec_sf,spec_sf_file);
        saveascii(int_sf,int_sf_file);
        print('-f1', '-dpng', figure1);
        figure(2);
        position=0:0.05:(L_GVD+L_gain+L2+0.1);
        length(position);
        subplot(121);
        plot(position,FWHM_t);
        ylabel('pulse duration (fs)');
        xlabel('position (m)');
        subplot(122);
        plot(position,FWHM_f);
        ylabel('bandwidth (nm)');
        xlabel('position (m)');
        FWHM_f=horzcat(position',FWHM_f');
        FWHM_t=horzcat(position',FWHM_t');
        saveascii(FWHM_f,FWHM_f_file);
        saveascii(FWHM_t,FWHM_t_file);
        print('-f2', '-dpng', figure2);
        saveascii(spec_2d,spec_2d_file);

    else
        L_GVD=L_GVD-0.5;

    end

else
```

```
L_GVD;
count_L_GVD=0;
bandwidth=max(FWHM_f);
data=[Esat bw L_GVD Eout bandwidth];
DATA=vertcat(DATA,data);

figure(1);

subplot(421);
plot(lambda,spec1);
title('1st SMF-spectrum');
xlim([1000 1130]);
ylim([-0.05 1.05]);
subplot(422);
plot(t,int1);
title('1st SMF-time');
spec1=horzcat(lambda,spec1);
int1=horzcat(t,int1);
saveascii(spec1,spec1_file);
saveascii(int1,int1_file);

subplot(423);
plot(lambda,spec_gain);
title('gain-spectrum');
xlim([1000 1130]);
ylim([-0.05 1.05]);
subplot(424);
plot(t,int_gain);
title('gain-time');
spec_gain=horzcat(lambda,spec_gain);
int_gain=horzcat(t,int_gain);
saveascii(spec_gain,spec_gain_file);
saveascii(int_gain,int_gain_file);

subplot(425);
plot(lambda,spec2);
title('2nd SMF-spectrum');
xlim([1000 1130]);
ylim([-0.05 1.05]);
subplot(426);
plot(t,int2);
title('2nd SMF-time');
spec2=horzcat(lambda,spec2);
int2=horzcat(t,int2);
saveascii(spec2,spec2_file);
saveascii(int2,int2_file);

subplot(427);
plot(lambda,spec_sf);
title('Spectral Filter-spectrum');
xlim([1000 1130]);
ylim([-0.05 1.05]);
xlabel('wavelength(nm)');
subplot(428);
plot(t,int_sf);
title('Spectral Filter-time');
```

```
    xlabel('time(fs)');
    spec_sf=horzcat(lambda,spec_sf);
    int_sf=horzcat(t,int_sf);
    saveascii(spec_sf,spec_sf_file);
    saveascii(int_sf,int_sf_file);

    print('-f1', '-dpng', figure1);

    figure(2);

    position=0:0.05:(L_GVD+L_gain+L2+0.1);%change step to 0.02, then the 0.04
is for two steps of saturable absorber and spectral filter
    length(position);
    subplot(121);
    plot(position,FWHM_t);
    ylabel('pulse duration (fs)');
    xlabel('position (m)');
    subplot(122);
    plot(position,FWHM_f);
    ylabel('bandwidth (nm)');
    xlabel('position (m)');
    FWHM_f=horzcat(position',FWHM_f');
    FWHM_t=horzcat(position',FWHM_t');
    saveascii(FWHM_f,FWHM_f_file);
    saveascii(FWHM_t,FWHM_t_file);

    print('-f2', '-dpng', figure2);

    saveascii(spec_2d,spec_2d_file);
%     size(spec_2d)
%     size(FWHM_t)
%     size(position)
%     size(lambda)
    figure(3);
%     spec_2d=log10(spec_2d);
    contour(position,lambda,spec_2d,500);
    colorbar;
end

%check whether the length of the first segment of passive fiber is over the
%desired value
if (L_GVD+0.5)>L_GVD_max
    break;
else
end
    end

%     %check whether it is multi-pulsing for the loop using varibale filter
%     %bandwidth
% if max(FWHM_t)>12000
%     count_bw=count_bw+1;
%     if count_bw>10
%         bw;
%         strcat('filter bandwidth of ',num2str(bw),'nm is a not stabel
solution')
```

```
%     else
%     bw=bw-1;
%     end
%     else
%     bw;
% end
%
% %check whether the filter bandwith is over the desired one%
if (bw+1)>bw_max
    break;
else
end
end

if (Esat+100)>Esat_max
    break;
else
end
end
    DATA_file=strcat(folder,'data_051311.dat');
    saveascii(DATA,DATA_file);
```

Appendix-II Fiber Laser Setup and Alignment

1. Overview of the whole setup of a similariton fiber laser

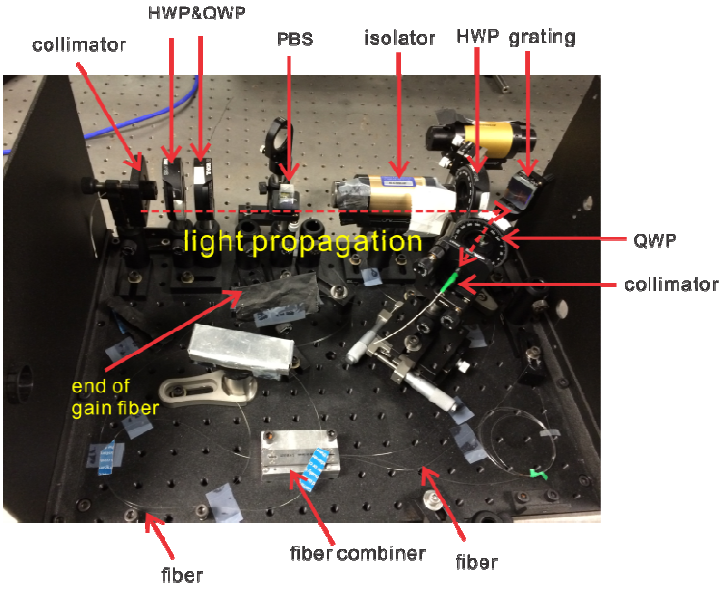

Figure 83: Layout of the similartion fiber laser.

2. Fiber laser alignment

Step #1, splice all fiber together and use fiber combiner to couple the pump laser to gain fiber

Step #2, put fiber collimators to their mount

Step #3, put in HWP, QWP and PBS

Step #4, turn on pump laser and operate it at low power

Step #5, adjust both collimators, make their output beam at the same height and propagate a long distance without changing height. Then, by putting a IR card or a piece of paper in front of one of the collimators, adjust the other collimator to overlap its output to the beam on the back of the card or paper from the other collimator, vice versa. Important: DO NOT COUPLE THEIR OUTPUT INTO EACH OTHER WITHOUT GOING THROUGH THE ISOLATOR.

Step #6, after the beams overlapped at the output of both collimators, put in isolator and adjust the isolator to pass the light. Up to this step, the rough alignment is done. Most likely the cavity is not lasing yet.

Step #7, adjust the wave plates to maximize the output power after the PBS

Step #8, adjust both collimators very carefully by monitoring the output power, once enough coupling efficiency reaches, the cavity starts lasing and the output power changes dramatically.

Step #9, once cavity start lasing, adjust wave plates again to maximize the output

Step #10, adjust collimators until the output power cannot be increased

Step #11, adjust the isolator to see if the output power can be improved

Step #12, adjust collimators again to maximize the output power

Step #13, cavity alignment is done.

3. Spectral filter

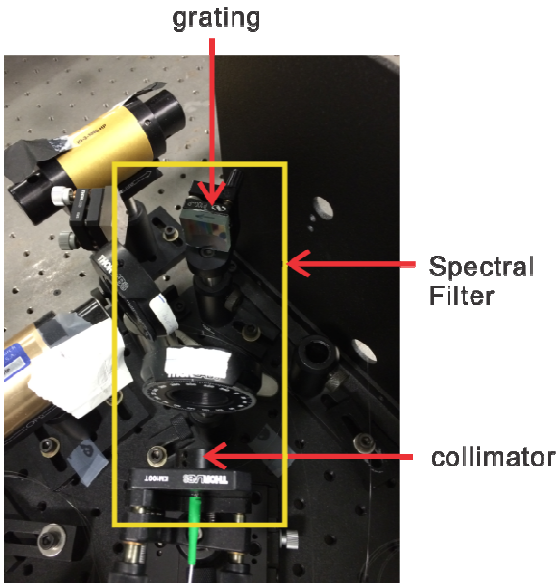

Figure 84: Layout of the spectral filter.

4. Splicing between gain fiber and SMF-II

Different than passive fiber-to-passive fiber splicing, splicing between gain fiber and SMF-II fiber needs special care. In order to remove the excess pump to avoid it mixed in the laser output, the pump light has to be removed at the end of gain fiber. Index matching gel is applied to the splicing joint between gain fiber and SMF-II. This index matching gel has refractive index larger than cladding, which will cause the leak of the gain fiber. After the index matching gel is applied, the splicing joint should be cover since there is strong scattering light coming out.

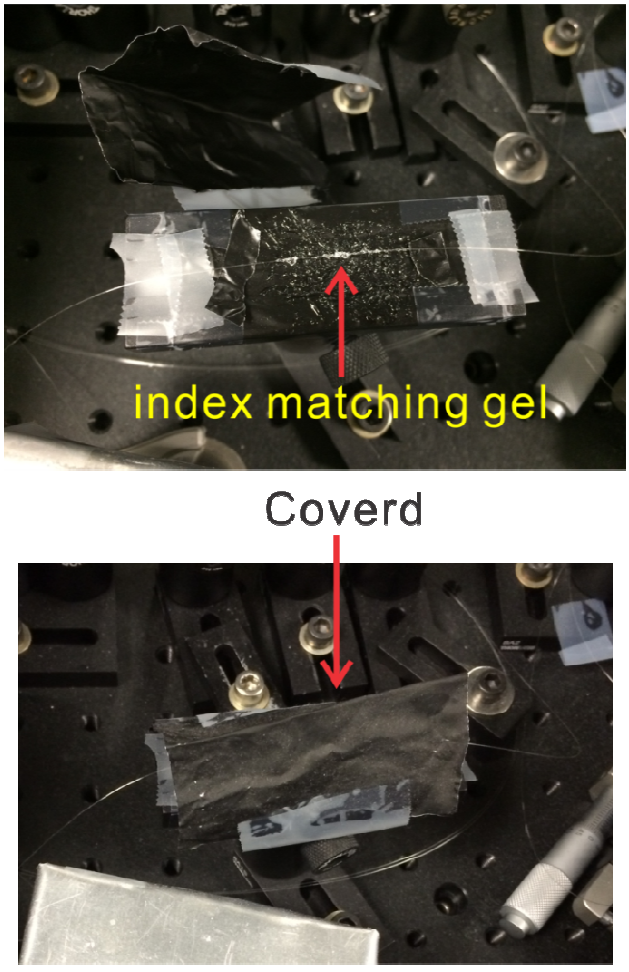

Figure 85: Splicing between gain fiber and SMF-II

Appendix-III Publication List

1. B. Nie, V. V. Lozovoy, M. Dantus, “Complete pulse characterization based on multiphoton intrapulse interference,” to be submitted.
2. B. Nie, I. Saytashev, and M. Dantus, “Towards a compact fiber laser for multimodal imaging,” Proc. SPIE 8948, 89480A (2014).
3. B. Nie, G. Parker, V. V. Lozovoy, M. Dantus, “Energy scaling and application of Yb fiber oscillators producing clusters of femtosecond pulses,” Optical Engineering 53, 051505 (2013).
4. A. Ryabtsev, B. Nie, M. Dantus, “45 fs optical pulses from phase corrected broadband cascaded four wave mixing products,” Laser Phys. Lett. 10, 125109 (2013).
5. G. Rasskazov, A. Ryabtsev, D. Pestov, B. Nie, V. V. Lozovoy, M. Dantus, “Anomalous laser-induced group velocity dispersion in fused silica,” Opt Express, 21 (15), 17695-17700 (2013).
6. B. Nie, I. Saytashev, A. Chong, H. Liu, S. N. Arkhipov, F. W. Wise, M. Dantus, “Multimodal microscopy with sub-30 fs Yb fiber laser oscillator,” Biomed Opt Express, 3 (7), 1750-1756 (2013).
7. A. Chong, H. Liu, B. Nie, B. Bale, S. Wabnitz, W. Renninger, M. Dantus, F. W. Wise, “Pulse generation without gain-bandwidth limitation in a laser with self-similar evolution,” Opt Express, 20 (13), 14213 (2012).
8. B. Nie, D. Pestov, F. W. Wise, M. Dantus, “An Ultrafast Fiber Laser with Self-Similar Evolution in the Gain Segment,” Optics and Photonics News, 22 (12), 47 (2011). ('Optics in 2011')
9. B. Nie, D. Pestov, F. W. Wise, M. Dantus, “Generation of 42-fs and 10-nJ pulses from a fiber laser with self-similar evolution in the gain segment,” Opt Express, 19 (13), 12074-12080 (2011). (Vol. 6, Iss. 7 *Virtual Journal for Biomedical Optics*)

BIBLIOGRAPHY

BIBLIOGRAPHY

1. R. G. Gould, "The LASER, light amplification by stimulated emission of radiation," in *The Ann Arbor conference on optical pumping, the University of Michigan*(1959), p. 128.

2. T. H. Maiman, "Stimulated optical radiation in ruby," (1960).

3. http://www.strategies-u.com/articles/2010/05/recovery-and-new-opportunities.html.

4. A. H. Zewail, "Femtochemistry: Recent progress in studies of dynamics and control of reactions and their transition states," Journal of Physical Chemistry 100, 12701-12724 (1996).

5. D. J. Jones, S. A. Diddams, J. K. Ranka, A. Stentz, R. S. Windeler, J. L. Hall, and S. T. Cundiff, "Carrier-envelope phase control of femtosecond mode-locked lasers and direct optical frequency synthesis," Science 288, 635-639 (2000).

6. W. Denk, J. H. Strickler, and W. W. Webb, "2-Photon Laser Scanning Fluorescence Microscopy," Science 248, 73-76 (1990).

7. B. N. Chichkov, C. Momma, S. Nolte, F. vonAlvensleben, and A. Tunnermann, "Femtosecond, picosecond and nanosecond laser ablation of solids," Applied Physics a-Materials Science & Processing 63, 109-115 (1996).

8. P. F. Moulton, "Spectroscopic and Laser Characteristics of Ti-Al2o3," Journal of the Optical Society of America B-Optical Physics 3, 125-133 (1986).

9. D. Strickland, and G. Mourou, "Compression of Amplified Chirped Optical Pulses," Optics Communications 56, 219-221 (1985).

10. "NIF Status Update – 2014," https://lasers.llnl.gov/news/status.

11. "Optical fiber," http://en.wikipedia.org/wiki/File:Optical-fibre.svg.

12. J. Limpert, T. Schreiber, and A. Tünnermann, "Fiber based high power laser systems," http://www. highpowerlasers. rp-photonics. com/fiber_systems. html 3 (2005).

13. P. Russell, "Photonic crystal fibers," Science 299, 358-362 (2003).

14. C.-H. Liu, G. Chang, N. Litchinitser, A. Galvanauskas, D. Guertin, N. Jabobson, and K. Tankala, "Effectively single-mode chirally-coupled core fiber," in *Advanced Solid-State Photonics*(Optical Society of America2007), p. ME2.

15. F. Parmigiani, C. Finot, K. Mukasa, M. Ibsen, M. A. Roelens, P. Petropoulos, and D. J. Richardson, "Ultra-flat SPM-broadened spectra in a highly nonlinear fiber using parabolic pulses formed in a fiber Bragg grating," Optics Express 14, 7617-7622 (2006).

16. A. Ghatak, and K. Thyagarajan, *An introduction to fiber optics* (Cambridge university press, 1998).

17. "Disperision in fiber," http://www.thorlabs.com/images/TabImages/1.31_Zero-Dispersion_780.jpg.

18. G. P. Agrawal, *Nonlinear Fiber Optics* (Academic Press, 1995).

19. R. W. Boyd, *Nonlinear optics* (Academic press, 2003).

20. A. Shabat, and V. Zakharov, "Exact theory of two-dimensional self-focusing and one-dimensional self-modulation of waves in nonlinear media," Soviet Physics JETP 34, 62-69 (1972).

21. A. Scott, *Encyclopedia of nonlinear science* (Routledge, 2005).

22. P. Kelley, "Self-focusing of optical beams," Physical Review Letters 15, 1005 (1965).

23. A. Hasegawa, and F. Tappert, "Transmission of stationary nonlinear optical pulses in dispersive dielectric fibers. I. Anomalous dispersion," Applied Physics Letters 23, 142-144 (1973).

24. R. A. Fisher, and W. Bischel, "Role of Linear Dispersion in Plane-Wave Self-Phase Modulation," Applied Physics Letters 23, 661-663 (1973).

25. R. A. Fisher, and W. K. Bischel, "Numerical Studies of Interplay between Self-Phase Modulation and Dispersion for Intense Plane-Wave Laser Pulses," Journal of Applied Physics 46, 4921-4934 (1975).

26. W. J. Tomlinson, R. H. Stolen, and A. M. Johnson, "Optical-Wave Breaking of Pulses in Nonlinear Optical Fibers," Optics Letters 10, 457-459 (1985).

27. Y. e. Jeong, J. Sahu, D. Payne, and J. Nilsson, "Ytterbium-doped large-core fiber laser with 1.36 kW continuous-wave output power," Optics Express 12, 6088-6092 (2004).

28. O. E. Martinez, R. L. Fork, and J. P. Gordon, "Theory of Passively Mode-Locked Lasers Including Self-Phase Modulation and Group-Velocity Dispersion," Optics Letters 9, 156-158 (1984).

29. I. N. Duling, "All-Fiber Ring Soliton Laser Mode-Locked with a Nonlinear Mirror," Optics Letters 16, 539-541 (1991).

30. J. Limpert, T. Schreiber, S. Nolte, H. Zellmer, T. Tunnermann, R. Iliew, F. Lederer, J. Broeng, G. Vienne, and A. Petersson, "High-power air-clad large-mode-area photonic crystal fiber laser," Optics Express 11, 818-823 (2003).

31. A. Chong, J. Buckley, W. Renninger, and F. Wise, "All-normal-dispersion femtosecond fiber laser," Optics Express 14, 10095-10100 (2006).

32. B. Oktem, C. Ulgudur, and F. O. Ilday, "Soliton-similariton fibre laser," Nature Photonics 4, 307-311 (2010).

33. A. J. Kenyon, "Recent developments in rare-earth doped materials for optoelectronics," Progress in Quantum Electronics 26, 225-284 (2002).

34. C. Brecher, and L. A. Riseberg, "Laser-induced fluorescence line narrowing in Eu glass: A spectroscopic analysis of coordination structure," Physical Review B 13, 81-93 (1976).

35. Y. D. Huang, M. Mortier, and F. Auzel, "Stark levels analysis for Er3+-doped oxide glasses: germanate and silicate," Optical Materials 15, 243-260 (2001).

36. Z. Wei, B. Zhou, Y. Zhang, Y. Zou, X. Zhong, C. Xu, and Z. Zhang, "All Solid-State Passively Mode-Locked Ultrafast Lasers Based on Nd, Yb, and Cr Doped Media," (2012).

37. M. E. Fermann, M. Hofer, F. Haberl, and S. P. Craigryan, "Femtosecond Fiber Laser," Electronics Letters 26, 1737-1738 (1990).

38. D. J. Richardson, J. Nilsson, and W. A. Clarkson, "High power fiber lasers: current status and future perspectives," Journal of the Optical Society of America B-Optical Physics 27, B63-B92 (2010).

39. "IPG Photonics 100kW fiber laser," http://www.laserfocusworld.com/articles/print/volume-49/issue-12/world-news/materials-processing-100-kw-fiber-laser-power-meter-serve-industry.html http://optics.org/news/3/10/44.

40. J. D. Kafka, T. Baer, and D. W. Hall, "Mode-Locked Erbium-Doped Fiber Laser with Soliton Pulse Shaping," Optics Letters 14, 1269-1271 (1989).

41. M. Hofer, M. H. Ober, F. Haberl, and M. E. Fermann, "Characterization of Ultrashort Pulse Formation in Passively Mode-Locked Fiber Lasers," Ieee Journal of Quantum Electronics 28, 720-728 (1992).

42. J. S. Russell, "Report on waves," in *14th meeting of the British Association for the Advancement of Science*(1844), p. 390.

43. L. F. Mollenauer, E. Lichtman, G. T. Harvey, M. J. Neubelt, and B. M. Nyman, "Demonstration of Error-Free Soliton Transmission over More Than 15000 Km at 5 Gbit/S, Single-Channel, and over More Than 11000 Km at 10 Gbit/S in 2-Channel Wdm," Electronics Letters 28, 792-794 (1992).

44. F. W. Wise, A. Chong, and W. H. Renninger, "High-energy femtosecond fiber lasers based on pulse propagation at normal dispersion," Laser & Photonics Reviews 2, 58-73 (2008).

45. M. E. Fermann, and I. Hartl, "Ultrafast Fiber Laser Technology," Ieee Journal of Selected Topics in Quantum Electronics 15, 191-206 (2009).

46. H. A. Haus, J. G. Fujimoto, and E. P. Ippen, "Structures for Additive Pulse Mode-Locking," Journal of the Optical Society of America B-Optical Physics 8, 2068-2076 (1991).

47. B. Proctor, E. Westwig, and F. Wise, "Characterization of a Kerr-Lens Mode-Locked Ti-Sapphire Laser with Positive Group-Velocity Dispersion," Optics Letters 18, 1654-1656 (1993).

48. A. Martinez, and Z. Sun, "Nanotube and graphene saturable absorbers for fibre lasers," Nature Photonics 7, 842-845 (2013).

49. N. Doran, and D. Wood, "Nonlinear-optical loop mirror," Optics Letters 13, 56-58 (1988).

50. M. Hofer, M. E. Fermann, F. Haberl, M. H. Ober, and A. J. Schmidt, "Mode-Locking with Cross-Phase and Self-Phase Modulation," Optics Letters 16, 502-504 (1991).

51. E. P. Ippen, H. A. Haus, and L. Y. Liu, "Additive Pulse Mode-Locking," Journal of the Optical Society of America B-Optical Physics 6, 1736-1745 (1989).

52. A. Weiner, "Femtosecond pulse shaping using spatial light modulators," Review of scientific instruments 71, 1929-1960 (2000).

53. V. V. Lozovoy, I. Pastirk, and M. Dantus, "Multiphoton intrapulse interference. IV. Ultrashort laser pulse spectral phase characterization and compensation," Optics Letters 29, 775-777 (2004).

54. B. Xu, J. M. Gunn, J. M. D. Cruz, V. V. Lozovoy, and M. Dantus, "Quantitative investigation of the multiphoton intrapulse interference phase scan method for simultaneous phase measurement and compensation of femtosecond laser pulses," JOSA B 23, 750-759 (2006).

55. Y. Coello, V. V. Lozovoy, T. C. Gunaratne, B. W. Xu, I. Borukhovich, C. H. Tseng, T. Weinacht, and M. Dantus, "Interference without an interferometer: a different approach to measuring, compressing, and shaping ultrashort laser pulses," Journal of the Optical Society of America B-Optical Physics 25, A140-A150 (2008).

56. W. R. Zipfel, R. M. Williams, and W. W. Webb, "Nonlinear magic: multiphoton microscopy in the biosciences," Nature biotechnology 21, 1369-1377 (2003).

57. B. Nie, I. Saytashev, A. D. Chong, H. Liu, S. N. Arkhipov, F. W. Wise, and M. Dantus, "Multimodal microscopy with sub-30 fs Yb fiber laser oscillator," Biomedical Optics Express 3, 1750-1756 (2012).

58. A. Chong, W. H. Renninger, and F. W. Wise, "All-normal-dispersion femtosecond fiber laser with pulse energy above 20 nJ," Optics Letters 32, 2408-2410 (2007).

59. K. Kieu, W. H. Renninger, A. Chong, and F. W. Wise, "Sub-100 fs pulses at watt-level powers from a dissipative-soliton fiber laser," Optics Letters 34, 593-595 (2009).

60. B. G. Bale, and S. Wabnitz, "Strong spectral filtering for a mode-locked similariton fiber laser," Optics Letters 35, 2466-2468 (2010).

61. W. H. Renninger, A. Chong, and F. W. Wise, "Self-similar pulse evolution in an all-normal-dispersion laser," Physical Review A 82, 021805(R) (2010).

62. D. Anderson, M. Desaix, M. Karlsson, M. Lisak, and M. L. Quirogateixeiro, "Wave-Breaking-Free Pulses in Nonlinear-Optical Fibers," Journal of the Optical Society of America B-Optical Physics 10, 1185-1190 (1993).

63. V. I. Kruglov, A. C. Peacock, J. D. Harvey, and J. M. Dudley, "Self-similar propagation of parabolic pulses in normal-dispersion fiber amplifiers," Journal of the Optical Society of America B-Optical Physics 19, 461-469 (2002).

64. M. E. Fermann, V. I. Kruglov, B. C. Thomsen, J. M. Dudley, and J. D. Harvey, "Self-similar propagation and amplification of parabolic pulses in optical fibers," Physical Review Letters 84, 6010-6013 (2000).

65. F. O. Ilday, J. R. Buckley, W. G. Clark, and F. W. Wise, "Self-similar evolution of parabolic pulses in a laser," Physical Review Letters 92, 213902 (2004).

66. C. Aguergaray, D. Mechin, V. Kruglov, and J. D. Harvey, "Experimental realization of a Mode-locked parabolic Raman fiber oscillator," Optics Express 18, 8680-8687 (2010).

67. L. R. Keefe, "Dynamics of Perturbed Wavetrain Solutions to the Ginzburg-Landau Equation," Studies in Applied Mathematics 73, 91-153 (1985).

68. M. J. Landman, "Solutions of the Ginzburg-Landau Equation of Interest in Shear-Flow Transition," Studies in Applied Mathematics 76, 187-237 (1987).

69. W. Vansaarloos, and P. C. Hohenberg, "Fronts, Pulses, Sources and Sinks in Generalized Complex Ginzburg-Landau Equations," Physica D 56, 303-367 (1992).

70. G. P. Agrawal, *Nonlinear Fiber Optics* (Academic Press, Inc., 2001).

71. Y. Coello, V. V. Lozovoy, T. C. Gunaratne, B. Xu, I. Borukhovich, C. Tseng, T. Weinacht, and M. Dantus, "Interference without an interferometer: a different approach to measuring, compressing, and shaping ultrashort laser pulses," JOSA B 25, A140-A150 (2008).

72. D. Pestov, V. V. Lozovoy, and M. Dantus, "Multiple Independent Comb Shaping (MICS): Phase-only generation of optical pulse sequences," Optics Express 17, 14351-14361 (2009).

73. T. Y. F. Tsang, "Optical third-harmonic generation at interfaces," Physical Review A 52, 4116-4125 (1995).

74. Y. Coello, V. V. Lozovoy, T. C. Gunaratne, B. Xu, I. Borukhovich, C.-h. Tseng, T. Weinacht, and M. Dantus, "Interference without an interferometer: a different approach to measuring, compressing, and shaping ultrashort laser pulses," Journal of the Optical Society of America B 25, A140-A150 (2008).

75. A. Chong, H. Liu, B. Nie, B. G. Bale, S. Wabnitz, W. H. Renninger, M. Dantus, and F. W. Wise, "Pulse generation without gain-bandwidth limitation in a laser with self-similar evolution," Optics Express 20, 14213-14220 (2012).

76. T. Hirooka, and M. Nakazawa, "Parabolic pulse generation by use of a dispersion-decreasing fiber with normal group-velocity dispersion," Optics Letters 29, 498-500 (2004).

77. R. W. Boyd, "Intuitive explanation of the phase anomaly of focused light beams," Journal of the Optical Society of America 70, 877-880 (1980).

78. Y. Barad, H. Eisenberg, M. Horowitz, and Y. Silberberg, "Nonlinear scanning laser microscopy by third harmonic generation," Applied Physics Letters 70, 922-924 (1997).

79. J. A. Squier, M. Muller, G. J. Brakenhoff, and K. R. Wilson, "Third harmonic generation microscopy," Optics Express 3, 315-324 (1998).

80. P. Xi, Y. Andegeko, D. Pestov, V. V. Lovozoy, and M. Dantus, "Two-photon imaging using adaptive phase compensated ultrashort laser pulses," Journal of Biomedical Optics 14 (2009).

81. P. Xi, Y. Andegeko, L. R. Weisel, V. V. Lozovoy, and M. Dantus, "Greater signal, increased depth, and less photobleaching in two-photon microscopy with 10 fs pulses," Optics Communications 281, 1841-1849 (2008).

82. D. Yelin, D. Oron, E. Korkotian, M. Segal, and Y. Silbergerg, "Third-harmonic microscopy with a titanium-sapphire laser," Applied Physics B-Lasers and Optics 74, S97-S101 (2002).

83. C. K. Sun, S. W. Chu, S. P. Tai, S. Keller, U. K. Mishra, and S. P. DenBaars, "Scanning second-harmonic/third-harmonic generation microscopy of gallium nitride," Applied Physics Letters 77, 2331-2333 (2000).

84. B. Nie, D. Pestov, F. W. Wise, and M. Dantus, "Generation of 42-fs and 10-nJ pulses from a fiber laser with self-similar evolution in the gain segment," Optics Express 19, 12074-12080 (2011).

85. D. Kobat, M. E. Durst, N. Nishimura, A. W. Wong, C. B. Schaffer, and C. Xu, "Deep tissue multiphoton microscopy using longer wavelength excitation," Optics Express 17, 13354-13364 (2009).

86. A. Chong, L. Hui, B. Nie, B. G. Bale, S. Wabnitz, W. H. Renninger, M. Dantus, and F. W. Wise, "Ultrabroadband mode-locked laser based on self-similar amplier pulse evolution," Optics Express 20, 14213-14220 (2012).

87. M. M. Wefers, and K. A. Nelson, "Space-time profiles of shaped ultrafast optical waveforms," Ieee Journal of Quantum Electronics 32, 161-172 (1996).

88. F. Frei, A. Galler, and T. Feurer, "Space-time coupling in femtosecond pulse shaping and its effects on coherent control," Journal of Chemical Physics 130, 034302 (2009).

89. D. Brinks, F. D. Stefani, and N. F. Hulst, "Nanoscale spatial effects of pulse shaping," Ultrafast Phenomena XVI 92, 890-892 (2009).

90. N. Krebs, R. A. Probst, and E. Riedle, "Sub-20 fs pulses shaped directly in the UV by an acousto-optic programmable dispersive filter," Optics Express 18, 6164-6171 (2010).

91. F. Frei, A. Galler, and T. Feurer, "Space-time coupling in femtosecond pulse shaping and its effects on coherent control," Journal of Chemical Physics 130 (2009).

92. D. A. Cremers, F. Y. Yueh, J. P. Singh, and H. Zhang, *Laser-Induced Breakdown Spectroscopy, Elemental Analysis* (Wiley Online Library, 2006).

93. J. P. Singh, and S. N. Thakur, *Laser-induced breakdown spectroscopy* (Elsevier, 2007).

94. R. Noll, H. Bette, A. Brysch, M. Kraushaar, I. Monch, L. Peter, and V. Sturm, "Laser-induced breakdown spectrometry - applications for production control and quality assurance in the steel industry," Spectrochimica Acta Part B-Atomic Spectroscopy 56, 637-649 (2001).

95. J. Gruber, J. Heitz, H. Strasser, D. Bauerle, and N. Ramaseder, "Rapid in-situ analysis of liquid steel by laser-induced breakdown spectroscopy," Spectrochimica Acta Part B-Atomic Spectroscopy 56, 685-693 (2001).

96. D. Anglos, "Laser-induced breakdown spectroscopy in art and archaeology," Applied Spectroscopy 55, 186a-205a (2001).

97. A. K. Knight, N. L. Scherbarth, D. A. Cremers, and M. J. Ferris, "Characterization of laser-induced breakdown spectroscopy (LIBS) for application to space exploration," Applied Spectroscopy 54, 331-340 (2000).

98. J. Cunat, S. Palanco, F. Carrasco, M. D. Simon, and J. J. Laserna, "Portable instrument and analytical method using laser-induced breakdown spectrometry for in situ characterization of speleothems in karstic caves," Journal of Analytical Atomic Spectrometry 20, 295-300 (2005).

99. F. Capitelli, F. Colao, M. R. Provenzano, R. Fantoni, G. Brunetti, and N. Senesi, "Determination of heavy metals in soils by laser induced breakdown spectroscopy," Geoderma 106, 45-62 (2002).

100. J. L. Gottfried, F. C. De Lucia, C. A. Munson, and A. W. Miziolek, "Laser-induced breakdown spectroscopy for detection of explosives residues: a review of recent advances, challenges, and future prospects," Analytical and Bioanalytical Chemistry 395, 283-300 (2009).

101. M. Baudelet, C. C. C. Willis, L. Shah, and M. Richardson, "Laser-induced breakdown spectroscopy of copper with a 2 mu m thulium fiber laser," Optics Express 18, 7905-7910 (2010).

102. H. Huang, L. M. Yang, and J. Liu, "Qualitative assessment of laser-induced breakdown spectra generated with a femtosecond fiber laser," Applied Optics 51, 8669-8676 (2012).

103. K. Y. Yamamoto, D. A. Cremers, M. J. Ferris, and L. E. Foster, "Detection of metals in the environment using a portable laser-induced breakdown spectroscopy instrument," Applied Spectroscopy 50, 222-233 (1996).

104. F. C. DeLucia, A. C. Samuels, R. S. Harmon, R. A. Walters, K. L. McNesby, A. LaPointe, R. J. Winkel, and A. W. Miziolek, "Laser-induced breakdown spectroscopy (LIBS): A promising versatile chemical sensor technology for hazardous material detection," Ieee Sensors Journal 5, 681-689 (2005).

105. A. Bertolini, G. Carelli, F. Francesconi, M. Francesconi, L. Marchesini, P. Marsili, F. Sorrentino, G. Cristoforetti, S. Legnaioli, V. Palleschi, L. Pardini, and A. Salvetti, "Modi: a new mobile instrument for in situ double-pulse LIBS analysis," Analytical and Bioanalytical Chemistry 385, 240-247 (2006).

106. M. Scharun, C. Fricke-Begemann, and R. Noll, "Laser-induced breakdown spectroscopy with multi-kHz fibre laser for mobile metal analysis tasks - A comparison of different analysis methods and with a mobile spark-discharge optical emission spectroscopy apparatus," Spectrochimica Acta Part B-Atomic Spectroscopy 87, 198-207 (2013).

107. M. V, A. Pakulev, A. Stockhaus, M. Bolshov, K. Niemax, and R. Hergenroder, "A comparison of nanosecond and femtosecond laser-induced plasma spectroscopy of brass samples," Spectrochimica Acta Part B-Atomic Spectroscopy 55, 1771-1785 (2000).

108. M. Baudelet, L. Guyon, J. Yu, J. P. Wolf, T. Amodeo, E. Frejafon, and P. Laloi, "Femtosecond time-resolved laser-induced breakdown spectroscopy for detection and identification of bacteria: A comparison to the nanosecond regime," Journal of Applied Physics 99 (2006).

109. L. Ponce, L. Moreira, E. de Posada, M. Arronte, T. Flores, and E. Rodriguez, "Burst Mode Q: switched Laser Pulses for Plasma Excitation in LIBS Analysis," in *Laser Pulse Phenomena and Applications*, F. J. Duarte, ed. (InTech, 2010).

110. R. Knappe, H. Haloui, A. Seifert, A. Weis, and A. Nebel, "Scaling ablation rates for picosecond lasers using burst micromachining," in *LASE*(International Society for Optics and Photonics2010), pp. 75850H-75850H-75856.

111. V. Pinon, C. Fotakis, G. Nicolas, and D. Angios, "Double pulse laser-induced breakdown spectroscopy with femtosecond laser pulses," Spectrochimica Acta Part B-Atomic Spectroscopy 63, 1006-1010 (2008).

112. V. Pinon, and D. Anglos, "Optical emission studies of plasma induced by single and double femtosecond laser pulses," Spectrochimica Acta Part B-Atomic Spectroscopy 64, 950-960 (2009).

113. D. Du, X. Liu, G. Korn, J. Squier, and G. Mourou, "Laser-Induced Breakdown by Impact Ionization in Sio2 with Pulse Widths from 7 Ns to 150 Fs," Applied Physics Letters 64, 3071-3073 (1994).

114. P. P. Pronko, S. K. Dutta, D. Du, and R. K. Singh, "Thermophysical Effects in Laser Processing of Materials with Picosecond and Femtosecond Pulses," Journal of Applied Physics 78, 6233-6240 (1995).

115. E. G. Gamaly, A. V. Rode, B. Luther-Davies, and V. T. Tikhonchuk, "Ablation of solids by femtosecond lasers: Ablation mechanism and ablation thresholds for metals and dielectrics," Physics of Plasmas 9, 949-957 (2002).

116. T. Gunaratne, M. Kangas, S. Singh, A. Gross, and M. Dantus, "Influence of bandwidth and phase shaping on laser induced breakdown spectroscopy with ultrashort laser pulses," Chemical Physics Letters 423, 197-201 (2006).

117. M. Horowitz, Y. Barad, and Y. Silberberg, "Noiselike pulses with a broadband spectrum generated from an erbium-doped fiber laser," Optics Letters 22, 799-801 (1997).

118. L. M. Zhao, D. Y. Tang, J. Wu, X. Q. Fu, and S. C. Wen, "Noise-like pulse in a gain-guided soliton fiber laser," Optics Express 15, 2145-2150 (2007).

119. S. Kobtsev, S. Kukarin, S. Smirnov, S. Turitsyn, and A. Latkin, "Generation of double-scale femto/pico-second optical lumps in mode-locked fiber lasers," Optics Express 17, 20707-20713 (2009).

120. S. M. Kobtsev, and S. V. Smirnov, "Fiber lasers mode-locked due to nonlinear polarization evolution: Golden mean of cavity length," Laser Physics 21, 272-276 (2011).

121. S. Smirnov, S. Kobtsev, S. Kukarin, and S. Turitsyn, "Mode-Locked Fibre Lasers with High-Energy Pulses," in *Laser Systems for Applications*, K. Jakubczak, ed. (InTech, 2011).

122. A. I. Chernykh, and S. K. Turitsyn, "Soliton and Collapse Regimes of Pulse Generation in Passively Mode-Locking Laser Systems," Optics Letters 20, 398-400 (1995).

123. M. Horowitz, and Y. Silberberg, "Control of noiselike pulse generation in erbium-doped fiber lasers," Ieee Photonics Technology Letters 10, 1389-1391 (1998).

124. L. M. Zhao, D. Y. Tang, and A. Q. Liu, "Chaotic dynamics of a passively mode-locked soliton fiber ring laser," Chaos 16 (2006).

125. S. Chouli, and P. Grelu, "Rains of solitons in a fiber laser," Optics Express 17, 11776-11781 (2009).

126. D. Y. Tang, L. M. Zhao, and B. Zhao, "Soliton collapse and bunched noise-like pulse generation in a passively mode-locked fiber ring laser," Optics Express 13, 2289-2294 (2005).

127. D. Y. Tang, L. M. Zhao, B. Zhao, and A. Q. Liu, "Mechanism of multisoliton formation and soliton energy quantization in passively mode-locked fiber lasers," Physical Review A 72 (2005).

128. L. M. Zhao, and D. Y. Tang, "Generation of 15-nJ bunched noise-like pulses with 93-nm bandwidth in an erbium-doped fiber ring laser," Applied Physics B-Lasers and Optics 83, 553-557 (2006).

129. L. M. Cabalin, and J. J. Laserna, "Experimental determination of laser induced breakdown thresholds of metals under nanosecond Q-switched laser operation," Spectrochimica Acta Part B-Atomic Spectroscopy 53, 723-730 (1998).